POLITECNICO
MILANO 1863

SCUOLA DI INGEGNERIA INDUSTRIALE
E DELL'INFORMAZIONE

Ejecta plume observability from an asteroid small impactor mission

Tesi di Laurea Magistrale in
Space Engineering - Ingegneria Spaziale

Author: **Pierpaolo Merola**

Student ID: 970436
Advisor: Prof. Camilla Colombo
Co-advisors: Mirko Trisolini
Academic Year: 2021-2022

Abstract

The asteroids that intersect Earth's orbit were probably once part of the main belt, but due to gravitational influences with the gas giant Jupiter, they now orbit just a step away from our planet. The study of so called Near-Earth Objects (NEOs) is easier due to their proximity to our planet and is fundamental to understanding the formation and evolution of our solar system. In addition to aiding in the development of a dynamic model for a low gravity environment, observing the ejecta dust following an impact from an asteroid's surface enables the examination of the body's physical characteristics. In this work, an image simulator model is created to investigate the observability of such events. In particular, a small impactor, similar to the one used in JAXA's Hayabusa2 mission, is implemented for use on astrodie 162173 Ryugu. In addition, the possibility of observing the impact from a lander at a safe distance on the surface is being investigated to understand its utility and efficiency. The propagation of the dust dynamics is based on the photo-gravitational Circular Restricted Three-Body Problem (CR3BP) with perturbations due to the Ryugu gravitational irregularity, for which the coefficients J_2 and J_4 are implemented, while the image acquisition model is fully developed from scratch for this research. The images obtained focus on the dust, while the asteroid is represented as a sphere with a radius equal to the mean radius of the asteroid. Furthermore, a photometry model is developed in this thesis merging 2 existing models, giving a very good compromise needed for each phase angle. The model's potential is demonstrated by a comparison with actual photographs of the Hayabusa2 impact, which coincide with the images simulated at the observed instants time, and investigations on the apparent magnitude are carried out between the various observation sites. This thesis is part of the Collecting Asteroid Orbiting Samples (CRADLE) project.

Keywords: observability, impact, Ryugu, ejecta dust, simulated images, asteroids

Sommario

Lo studio degli asteroidi che affollano lo spazio a noi più vicino, i cosidetti NEOs (Near-Earth Objects), probabilmete migrati dalla fascia principale per via di influenze gravitazionali con il gigante gassoso Giove, è primario per comprendere la nasciata e l'evoluzione del nostro sistema solare, oltre che comodo per via della loro vicinanza al nostro pianeta. L'osservazione delle polveri scagliate dopo un impatto sulla superficie dell'asteroide, oltre che utile a creare un modello dinamico per ambienti a bassa gravità, permette di studiare le caratteristiche fisiche dell'asteroide stesso. In questa tesi un simulatore di immagini è modellato al fine di studiare l'osservabilita di tale eventi. In particolare, un piccolo impattatore, simile a quello utilizzato nella missione Hayabusa2 della JAXA, è implementato per essere utilizzato sull'asterodie 162173 Ryugu. Inoltre, la possibilità di avere un lander che osservi l'impatto dalla superficie ad una distanza di sicurezza è studiata per capirne l'utilità e l'efficienza. La propagazione della dinamica delle polveri si basa sul problema dei tre corpi circolare ristretto (CR3BP) perturbato dalla radiazione solare e alla irregolarità gravitazionale di Ryugu, per il quale i coefficienti J_2 e J_4 sono implementati, mentre il modello di acquisizione immagine è sviluppato appositamente per questa tesi. Le immagini ottenute si concentrano sulle polveri, mentre l'asteroide è visualizzato come una sfera di riaggio uguale al raggio medio dell'asteroide stesso. Inoltre, in questa tesi viene sviluppato un modello di fotometria unendo due modelli esistenti, fornendo un ottimo compromesso necessario per ogni angolo di fase. La comparazione tra le imamgini reali dell'impatto di Hayabusa2 dimostra il potenziale del modello, le quali combaciano molto bene con le immagini simulate, metre studi sulla magnitudine apparente che l'osservatore percepisce sono affrontati per valutare le differenze tra le varie posizioni di osservazione. Questa tesi fa parte del progetto CRADLE (Collecting Asteroid Orbiting Samples).

Parole chiave: osservabilità, impatto, Ryugu, polveri, immagini simulate, asteroidi

Contents

List of Figures

List of Tables

List of Acronyms

Acronym	Description
ADC	Analog to Digital converter.
ADCS	Attitude determination and control system.
AIDA	Asteroid Impact Deflection Assessment.
CR3BP	Circular restricted three-body problem.
CRADLE	Collecting Asteroid Orbiting Samples.
ESA	European Space Agency.
FoV	Field of view.
HST	Hubble Space Telescope.
IFoV	Istantaneus Field of view.
JAXA	Japan Aerospace Exploration Agency.
LINEAR	Lincoln Near-Earth Asteroid Research.
MAM	Autonomy manager.
MARA	Thermal IR radiometer.
MASCOT	Mobile Asteroid Surface Scout.
MATLAB	Matrix Laboratory.
MMEGA	Hyper-spectral infrared microscope MicrOmega.
MOID	Minimum Orbit Intersection.
NASA	National Aeronautics and Space Administration..
NEA	Near-Earth asteroid.
NEOs	Near-Earth objects.
PSF	Point spread function.
R3BP	Restricted three-body problem.
RAAN	Right Ascension of the Ascending Node.

Acronym	Description
SCI	Small carry-on impactor.
SFA	Sand and Fly Ashes.
SMP	Sapling device.
SRF	Synodic reference frame.
SRP	Solar radiation pressure.
WCB	Weakly Cemented Basalt.

List of Symbols

Variable	Description	SI unit
AU	Astronomic unit. 10, 16, 18, 42.	km
p	Ryugu geometric albedo. 10, 42.	
g	Ryugu surface gravity. 10, 31, 32.	cm/s^2
R	Ryugu mean radius. 10, 24-27, 34	km
ρ	Ryugu mean density. 10, 31, 32.	kg/cm^3
m_a	Ryugu mass. 10, 18, 27.	kg
m_s	Solar mass. 18, 27.	kg
β	lightness parameter. 16, 17, 19-21, 23, 24, 28.	
P_0	Solar flux at 1 AU. 16, 42.	W/m^2
c	Speed of Light. 16.	km/s
μ_{sun}	Solar gravity constant. 16.	km^3/s^2
c_R	reflectivity coefficient. 16.	
d	particle size (diameter). 16, 34, 42.	mm
μ	Sun - asteroid adimensional mass parameter. 18-28.	
r_{es}	Sun - asteroid main distance. 16.	
G	Gravitational costant. 17, 27.	$km^3/kg\ s^2$
ω	Sun - asteroid angular velocity. 17.	km/s^2
$\omega_{asteroid}$	Asteroid angular velocity. 34.	km/s^2
l	Length unit. 18.	
M	Mass unit. 18.	
v	Velocity unit. 18.	
τ	Time unit. 18.	
$\boldsymbol{R}$	particle position in SRF. 18.	

Variable	Description	SI unit
$\boldsymbol{r}$	ad. particle position in SRF. 18, 24-28, 40.	
r_{sp}	ad. Sun - particle distance in SRF. 19-21, 25, 28.	
r_{ap}	ad. asteroid - particle distance in SRF. 19-21, 25, 28.	
V	ad. CR3BP potential. 19-28.	
L	Lagrangian points	
C	Jacobi constant.21, 22.	
P_l	Conventional Legendre polynomials. 24, 26.	
$P_{l,m}$	Associated Legendre polynomials. 24	
$C_{l,m}$	Gravity field coefficients. 24.	
$S_{l,m}$	Gravity field coefficients. 24.	
J_l	Jacobi constant. 24-26.	
η	Asteroid latitude. 25-26, 34.	
α	Asteroid longitude. 24, 34.	
U	Impactor velocity. 30-31.	km/s
a	Impactor radius. 30-32.	cm
δ	Impactor density. 30-32.	kg/cm^3
m	Impactor mass. 30-32.	kg
R_c	Crater radius. 31-33.	m
u_p	Ejecta velocity. 31, 34.	cm/s
T	Crater formation time. 32.	
V_c	Crater volume. 32.	
γ	Ejecta inclination. 33.	
$\boldsymbol{v_{rot}}(\phi)$	surface velocity. 34.	
G_d	Size cumulative distribution function. 34.	
N_r	Multiplicative factor. 34.	
$\bar{\alpha}$	Power law exponent. 34, 35, 59.	
M_{tot}	Total ejecta mass. 34.	kg
u	Focal distance. 38-40.	mm
L	Detector size. 38-40.	mm
θ_{FoV}	FoV. 38, 44, 57.	mm

Variable	Description	SI unit
d_{px}	Pixel size. 38, 44, 57.	mm
n_{px}	Pixel number. 38, 44, 57.	
f	Focal length. 44, 57.	mm
H_m	Particle absolute magnitude. 42	
m_p	Particle apparent magnitude. 42.	
F_{diff}	Particle reflected solar radiation (Lambertian model). 42.	W/m^2
ϕ	Phase angle. 42, 69.	
H_{px}	Image resolution. 47.	m/px

1 | Introduction

From the first observation of what would later be called an Asteroid, up to a redirection test mission of one of them, 221 years have passed. In 1802, the astronomer Giuseppe Piazzi observed an area of the sky in search of a missing planet, between the orbits of Mars and Jupiter. Indeed, a numerical sequence had been found, which distributed the planets at a certain distance around the Sun, the Titus - Bode law. The number sequence seemed confirmed when he found what he was looking for, naming the missing planet Ceres. After that, other astronomers and scientists observed that portion of the sky, to confirm the presence of the new planet. However, the German astronomer Heinrich Wilhelm Olbers, in 1807, found another celestial body, Vesta. Since then, many other smaller bodies have been discovered, identifying this asteroid-rich area as the Asteroid Belt. Due to gravitational influences, some of them have migrated to the inner solar system, in some cases settling in trajectories that intercept the Earth's orbit, the so-called Near-Earth Objects (NEOs). Precisely on one of them, the DART mission was able for the first time in the history of space exploration to modify the orbit of Dimorphos, the smallest asteroid of the Didymos binary system.

Asteroids have always been a subject of study for understanding the formation of the solar system, as well as the appearance of life on our planet. Besides, the exploitation of their resources is also a topic of debate among space agencies and private companies. For both purposes, NEOs are the most attractive targets for robotic probes, guaranteeing a lower cost and the possibility of maintaining mission control from ground stations. Indeed, several missions have had the objective of exploring some of these bodies, such as the Hayabusa and Hayabusa2 missions (JAXA), respectively on the asteroids 25143 Itokawa and 162173 Ryugu, the OSIRIS-REx mission on the asteroid 101955 Bennu and the DART mission on the minor asteroid of the system 65803 Didymos (NASA). Some missions, on the other hand, have exploited the passage of Jupiter-family comets in the inner solar system, as in the case of the Rosetta mission (ESA), on comet 67P/Churyumov–Gerasimenko, and the Deep Impact mission (NASA), on comet 9P/Tempel.

A particular and alternative study method for asteroids is the observation of the crater

and the ejecta dust deriving from the impact on its surface. This event also leads to a significant increase in brightness (they are called "active" asteroid), so much that some of them have been discovered thanks to this phenomenon. However, natural collisions on the surface of asteroids are very rare, therefore, some of the missions mentioned above have implemented an impact on the target, using projectiles specially designed for the mission, or the probe itself, as in the case of the DART mission. Furthermore, in the Hayabusa2 mission, the crater formed provided a site for collecting material from the surface, while the possibility for future missions of collecting dust directly in orbit after an impact on the asteroid has been studied. This method is complementary to simple asteroid observation and allows for creating more sophisticated dynamics models in a low-gravity environment.

This thesis is part of the Collecting Asteroid Orbiting Samples (CRADLE) project, aimed at the development of methodologies and tools for collecting material without necessarily having to reach the surface of the body. The host institutions of the CRADLE Project are the Politecnico di Milano, which is the main institutions, and the Japan Aerospace Exploration Agency (JAXA), which is the “Third Country” institution.

1.1. Thesis aim

The aim of this research is the ejecta plume observability characterization of small impact on the asteroid’s surface, using a simulated image generator developed specifically for this study. The asteroid 162173 Ryugu will be the main subject of the research, and the impact on its surface will have the characteristics of the one already occurred in the Hayabusa2 mission to have a direct comparison with the real images. For this purpose, the implementation of the photo-gravitational Circular Restricted Three-Body Problem (CR3BP) and gravitational perturbations is necessary for dust dynamics propagation. With the dust position data over time, an image acquisition model is developed, taking as reference cameras already successfully tested in space for the same purpose. The choice of the camera used to obtain the images is mainly based on the distance from the event: the wider the distance, the smaller the Field of View (FoV).

1.2. Thesis contributions

The developed image simulator generates dust images for each instant of time to be studied, from any position around the asteroid itself. These images are used for a preliminary study of the observability of the event. Regarding the dynamic model used, this study reports the derivation and use of the equations for the gravitational field coefficient J_4,

an upgrade of the asteroid model compared to the reference taken for the construction of the dynamics model. In this research, a camera is also implemented on several landers positioned on the surface of the asteroid during the impact, in order to document the event from a very close distance and from a different angle. Having a lander on the surface during the impact allows for obtaining seismic surveys for the study of the internal structure of the asteroid, alternating with the use of radar. Small landers of this type (for nomenclature and size reasons, they are called nanolanders) have already been used on the asteroid, but with different purposes. The innovation of this thesis is the utility and ejecta plume visibility studies of a lander during an impact on the asteroid.

Thesis outline

The thesis is organized as follows:

- **Chapter 2**: previous research and studies relevant to the thesis are summarized to define the starting point and to have the tools to carry on the work;
- **Chapter 3**: the dynamical model of the three-body problem is reported, with the use of the gravitational field coefficients J_2 and J_4, the latter of which was used in the equations of motion specially obtained for this study;
- **Chapter 4**: the initial conditions of the ejecta dust are studied in relation to the type of impact and the type of asteroid surface;
- **Chapter 5**: the model of the optical system and image acquisition is developed, with the use of cameras already tested in space. Furthermore, the position of the observer is evaluated in relation to safety and visibility;
- **Chapter 6**: the use of the nanolander for images directly from the surface is evaluated, with the study of the ejecta particles landing time and the lander position on the surface;
- **Chapter 7**: simulated images of the model are displayed and visibility and brightness studies of the images are performed. Furthermore, the images obtained by the landers on the surface are evaluated for their possible usefulness;
- **Chapter 8**: the conclusions regarding the development of the model and its results are listed, with possible future developments.

2 | State of the art

This chapter discusses previous research on asteroid observation, laboratory tests, and asteroid rendezvous missions with impact on them. In terms of observability, the spacecraft payloads that have reached asteroids are studied to create realistic simulated image models. Additionally, there have been numerous studies on the dynamics of asteroid impacts, which have been integrated with laboratory tests and real-life impacts.

Various laboratory studies have enabled the development of an impact model with parameters that vary according to the type of asteroid. The strength and porosity of an asteroid are particularly important, as they define whether the impact falls under the strength regime or the gravity regime. To link laboratory experiments on Earth (in vacuum) with real impacts in low gravity environments, scaling laws based on the experimentally verified concept of the point source projectile are necessary.

The construction of the dynamic model is based on the Circular Restricted Three-Body Problem (CR3BP), already extensively studied in the literature, which however implements gravitational perturbations due to the irregular shapes of the attracting object, which are therefore specific to the asteroid studied.

2.1. Missions to asteroids and comets

Numerous missions to explore, collect, observe dust particles, and redirect the orbit of asteroids have been conducted by the various space agencies. Near Earth Objects (NEOs) are the best targets to be reached by space missions, due to their low costs, and to be observed from a telescope, due to their close range. Observations of impacts such as the Deep Impact [25], Hayabusa2, and Dart [2] missions provide important data and images to better define the model of dust ejections and to study the physical properties of asteroids. By combining the images with experimental data, crater images (and samples of the collected material as in the case of Hayabusa2), it is possible to obtain a relatively accurate range of values for the physical asteroid parameters. Furthermore, having images of an impact on an asteroid can provide data on the momentum transferred to the body,

as described in the work of Holsapple and Housen [8].

2.1.1. Deep Impact mission

The Deep Impact mission was a NASA space probe launched in January 2005 [24], with the primary objective of studying the composition and structure of a comet by intentionally impacting it with a projectile. The target comet was 9P/Tempel1, a short-period comet that orbits the Sun once every 5.5 years.

On July 4, 2005, the Deep Impact spacecraft successfully released a 372-kg impactor that collided with Tempel 1's nucleus at a speed of 10.2 km/s, creating a crater and ejecting material from the comet's interior. The collision was observed by the spacecraft's instruments with a minimum flyby distance of 575 km, and also by ground-based telescopes and Hubble Space Telescope. in Figure 2.1 the moments before and after the impact on the comet are shown.

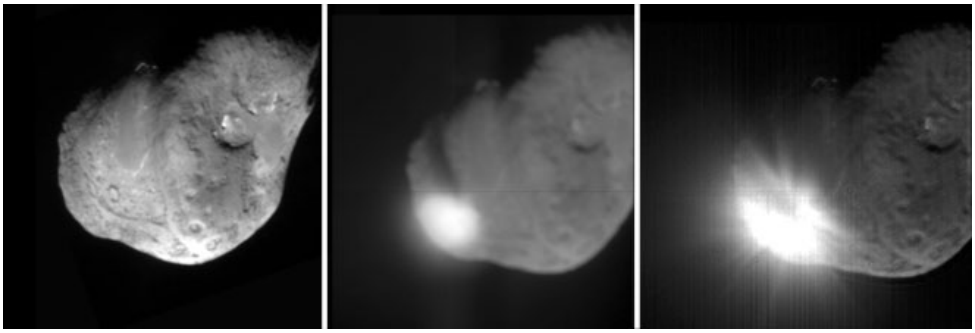

Figure 2.1: Deep Impact images [24].

The mission provided valuable data and insights into the composition and structure of comets. Scientists were able to analyze the ejected material and determine the comet's chemical makeup, which included organic compounds and minerals that could be related to the early solar system's formation. The Deep Impact mission was an important step in our understanding of comets and their role in the formation of the solar system. It paved the way for future missions that aimed to explore and study other comets.

2.1.2. Dart and LiciaCube missions

Double Asteroid Redirection Test (DART) mission is a NASA space probe designed to demonstrate asteroid deflection by intentionally impacting an asteroid with a spacecraft. The target of the DART mission is the moonlet of the asteroid system 65803 Didymos, named Dimorphos. Didymos is a binary asteroid system, which means it consists of two

asteroids orbiting each other. The larger asteroid, Didymos A, is about 780 meters in diameter, while the smaller moonlet, Dimorphos, is about 160 meters in diameter. The DART spacecraft will be targeting Dimorphos specifically.

The DART spacecraft is equipped with a high-speed impactor that collided with Dimorphos at a speed of around 6 km/s in October 2022. The impact has changed Dimorphos' orbit around Didymos, allowing scientists to study the effect of the impact on the asteroid's trajectory. The Italian LiciaCube probe, released before the impact, filmed the event on 26 September 2022 from a minimum flyby distance of 55 kilometers (Figure 2.2). The study on the cameras and on the Attitude Determination and Control System (ADCS) of the probes has proved to be of great importance, to guarantee the camera is always pointed precisely at the target during the high-speed passage of the asteroid.

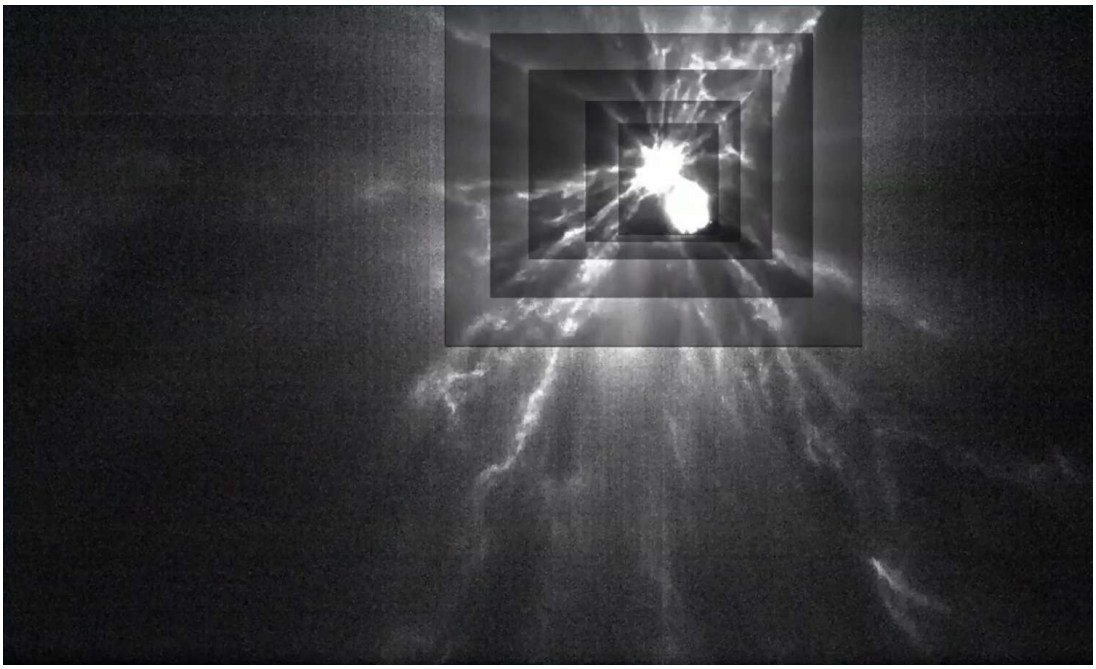

Figure 2.2: LiciaCube image of impact [28].

The event was also taken up by the Hubble Space Telescope (HST), of which the very recent studies of the images show the very long tails of dust days after the impact [22]. From the images in Figure 2.3 it is possible to see the evolution of the event filmed as never before. The study of these images gives the possibility to improve our knowledge on particle dynamics days after the impact. It is also the first time that an asteroid's environment has been voluntarily activated by humans, which has made it much more visible from ground-based and orbiting telescopes. Activating an asteroid is also one way they are observed for the first time, due to the higher luminosity level.

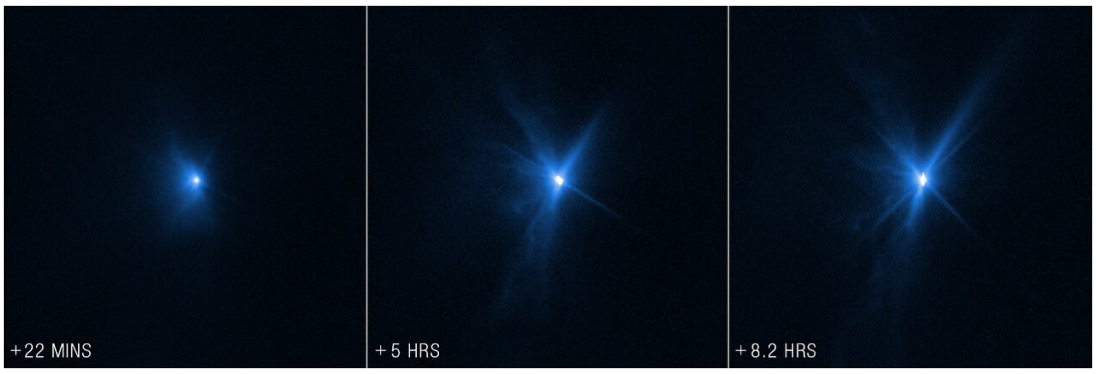

Figure 2.3: HST images of Dart impact [11].

2.1.3. Hayabusa2 mission

The Hayabusa2 mission is a Japanese space probe mission designed to study the asteroid Ryugu and collect samples of its surface materials for return to Earth. The mission was launched by the Japan Aerospace Exploration Agency (JAXA) in December 2014 and arrived at Ryugu in June 2018. 162173 Ryugu is a near-Earth asteroid with a diameter of approximately one kilometer. The Hayabusa2 spacecraft was equipped with a suite of instruments to study the asteroid's surface and interior, including a set of remote sensing instruments, the sapling device (SMP), small carry-on impactor (SCI), a small lander named MASCOT, and two small rovers named MINERVA-II [20].

During the course of the mission, the Hayabusa2 spacecraft performed multiple close flybys of Ryugu to gather data and images of its surface. It also successfully deployed the MINERVA-II rovers and the MASCOT lander to study different locations on the asteroid's surface. The highlight of the mission was the collection of surface samples from Ryugu using the spacecraft's sampling horn. In February 2019, the spacecraft descended to the asteroid's surface and fired a projectile at the asteroid to create a small crater. The spacecraft then collected the surface materials from the crater using its sampling horn and returned to Earth with the samples in December 2020. The samples collected by the Hayabusa2 mission will provide scientists with valuable insights into the formation and evolution of the solar system. They will also help in understanding the composition and physical properties of asteroids and their potential as resources for future exploration and mining.

Impact experiment

The Hayabusa2 mission also included an impact experiment on the asteroid Ryugu. In April 2019, the spacecraft deployed a small impactor called the Small Carry-on Impactor

(SCI) [29] towards the asteroid's surface. The SCI was designed to create an artificial impact crater on the asteroid's surface, which would allow scientists to study the interior of the asteroid. The SCI was a copper cylinder with a mass of about 2.5 kilograms and a diameter of 18 centimeters. It was equipped with an explosive charge that was designed to create a high-speed impact on the asteroid's surface. The SCI was launched from the Hayabusa2 spacecraft and was guided to the target site on Ryugu using optical and laser range finders.

In particular, the dust cloud shown in Figures 2.4, observed by the Deployable CAMera 3 (DCAM3), never detached from the surface, confirming the state of poor cohesion of the surface material. The crater was formed under gravity regime, with a final diameter greater than 10 meters and just over 2 meters deep [1]. The explosive charge of the SCI was supposed to accelerate the impactor up to 2 km/s shortly before reaching the surface. To protect the satellite from impact debris and explosive fragments, mission analysis was conducted in order to position the spacecraft safely. The study of the dust and the crater, combined with laboratory studies, was able to estimate the effective strength of the target surface, below 1.3 Pa.

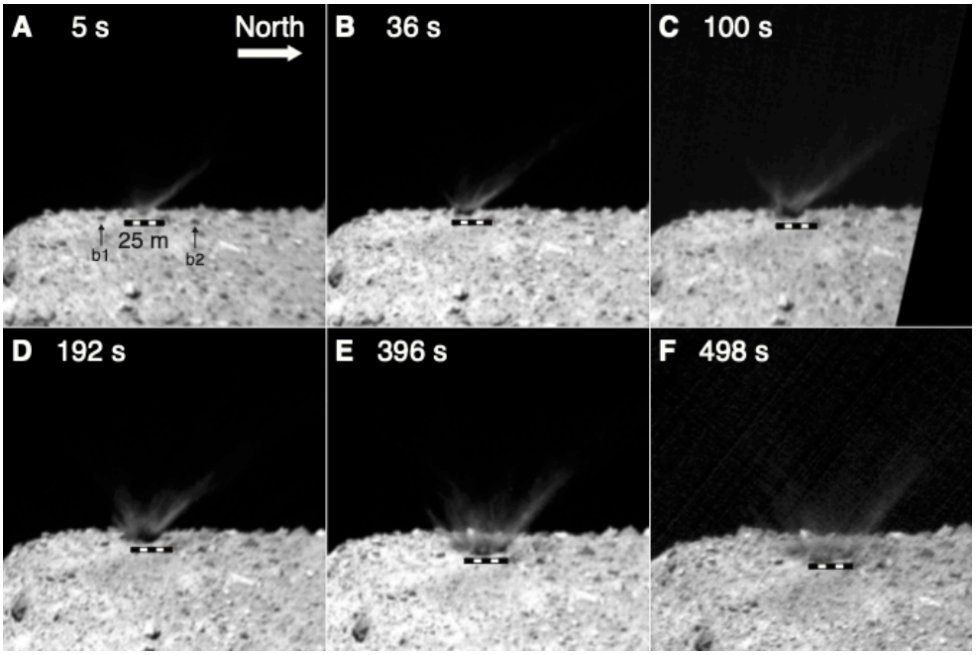

Figure 2.4: Impact of SCI in different time instants [1].

2.2. 162173 Ryugu

Ryugu is a near-Earth asteroid (NEA) that was studied by the Hayabusa2 mission launched by the Japan Aerospace Exploration Agency (JAXA) in 2014. It was discovered in 1999 by

astronomers at the Lincoln Near-Earth Asteroid Research (LINEAR) project and named after a dragon's palace in Japanese mythology. Ryugu [33] has a diameter of about 1 kilometer and is classified as a C-type asteroid, which means it is rich in carbon and other organic compounds. It has a low albedo, one of the lowest among the bodies of the solar system, which means it reflects only a small fraction of the sunlight that hits its surface. One of the most notable features of Ryugu is its shape, which resembles an oblate spinning top or a diamond. It has a rough, rocky surface with boulders and craters, and from visible spectrum observations, scientists believe it may have formed from the collision of two or more smaller asteroids. In fact, the asteroid families Eulalia and Polana report many parent bodies in the main asteroid belt. Based on the craters and their depth, the age of the surface of the body has been estimated to be between 10^8 and 10^7 years. Such high uncertainty derives from poor cohesion. The main characteristics of Ryugu are shown in Table 2.1. Mass and density indicate a high internal porosity, greater than 50%.

Orbital characteristics		**Physical characteristics**	
Aphelion	1.4159 AU	**Dimensions**	1004 m × 876 m
Perihelion	0.9633 AU	**Mean radius** R	448 ±2 m
RAAN	251.62 deg	**Mean density** ρ	1.19 g/cm^3
Orbital period	1.3 ys (474 d)	**Mass** m_a	(4.5 ±0.06) ×10^{11} kg
Rotation period	7,63262 h	**Surface gravity** g	0.011 cm/s^2
Eccentricity	0.1902	**Geometric albedo** p	0.045 ±0.002
Inclination	5.8837 deg	**Spectral type**	Cb-type
Earth MOID	0.0006 AU	**Abs magnitude**	19.3

Table 2.1: Orbital and physical characteristics of Ryugu [33] [41] [18].

2.2.1. Asteroid surface

Three types of surfaces are frequently discussed in studies regarding asteroids, as they are key in determining the degree of resistance and aggregation of the surface material. These surfaces are sand, Weakly Cemented Basalt (WCB), and Sand and Fly Ashes (SFA), as noted by Trisolini et al. [36]. In the case of sand, where the material has zero cohesion, impacts occur in the gravity regime, with the gravity of the asteroid being the only force governing the impact's evolution. For WCB, the impact occurs in the strength regime, where the resistance of the impacted material plays the most significant role in the impact's evolution. The third type of surface is a hybrid between the first two, with

several material typologies reported in various studies, including the Housen & Holsapple studies [10], where the model for crater formation is developed, and which will be used in this study.

Regarding Ryugu, observations have allowed for the cataloging of the asteroid's surface based on a certain range of cohesion and material resistance values [33]. The structures of the SCI crater and the observed ejecta dust by the Hayabusa2 spacecraft suggest that the impact occurred in the gravity-dominated regime, classifying the asteroid's soil as a sand-like material. Looking at the images of the impact in Figure 2.4, it can be seen that the dust cone never detaches from the surface, and the formation time of the crater is in the order of minutes.

2.3. Simulated images

The use of simulated images is an important tool to predict and compare the evolution of the dust around the asteroid. In order to obtain useful images, it is necessary to carefully analyze the positioning of the observer. Planned observations can involve simulating the impact by considering single particles or packets of particles [5], or by using a three-dimensional polygon-plume [25] to study the shape and opacity of the debris cone.

Once the dynamic model is used, the position and velocity of the ejecta particles are known. This allows for the acquisition of simulated images depending on the position of the spacecraft at a given moment after the impact. Various factors such as impact inclination, porosity, granulation type, and material type, change the shape and distribution of the raised dust. The image simulations of impact events compared to the real debris cloud images can provide valuable insights into the physical characteristics of the asteroid, such as its density, porosity, and strength. These simulations can also be used to determine the regime in which the impact occurred, whether it was gravity-dominated or strength-dominated. In addition, the visualization of the debris cloud can help to calculate the momentum transfer of the impact, which is important for understanding the impact process and its effects on the asteroid.

The cameras used to capture images of the debris cloud are critical to obtaining accurate data. Different missions use cameras with different field of view (FoV) depending on their distance from the asteroid. For example, spacecraft in flyby maneuvers around the asteroid need cameras with a small FoV to accurately pinpoint the asteroid even from a distance of more than 50 km (as in the case LEILA and LUKE onboard LiciaCube probe in DART mission [4]), while spacecraft in close proximity to the asteroid, like Hayabusa2 spacecraft, use DCAM3 cameras with a larger FoV to capture the entire debris cloud [13].

Table 2.2 shows the two types of cameras just mentioned. It is to be noted that, in the end, in the literature there is still nothing regarding image simulations of asteroid impacts from landers positioned on the surface of the asteroid itself during the impact.

LEIA (LiciaCube)		**DCAM3 (Hayabusa2)**	
Detector	CMOS	**Detector**	CMOS
Number of pixel	2048 x 2048	**Number of pixel**	2000 x 2000
Pixel size	5.5 x 5.5 µm	**Pixel size**	3.5 x 3.5 µm
FoV	2.06 deg	**FoV**	37 deg
IFoV	25 µrad/px	**IFoV**	0.65 mrad/px
Focal Length	220 mm	**Focal Length**	5.76 mm

Table 2.2: Camera characteristics of LiciaCube and Hayabusa2 [4] [13].

2.3.1. Comparison between simulated and real images

The images captured during the aforementioned missions generally do not exhibit the symmetry depicted in simulations. The dust cone resulting from the impact is subject to irregularities caused by the impact dynamics and the characteristics of the impacted surface, as demonstrated in Figure 2.4. The angle of inclination of the impact surface, which was studied in Richardson et al. [25]), can modify the orientation of the dust cone, while the presence of boulders can create privileged directions for the dust lifted by the impact.

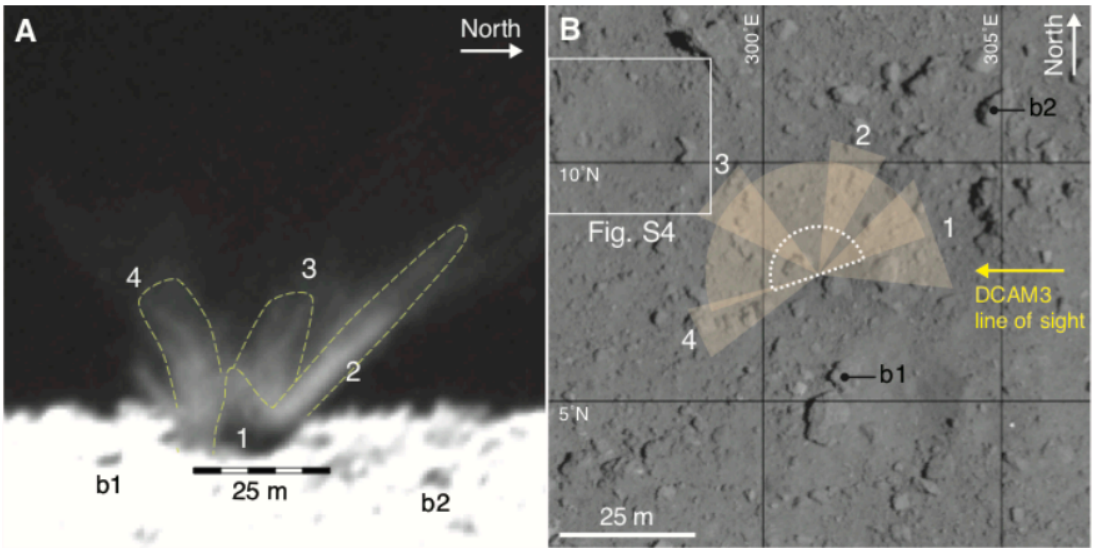

Figure 2.5: Impact ejecta and irregular impact topography [1].

In Figure 2.5 A, a snapshot of the Hayabusa2 impact dust cloud is shown, featuring denser arms. Figure 2.5 B displays a view from above of the impact site, revealing the presence of boulders within the affected area, likely responsible for the irregularities observed in the dust cone. Boulders and compacted material are part of the asteroids' topography, and considering them in analyses is challenging. In any case, variables such as the size of the crater, the duration of the cratering event, and the shape of the dust cone can provide us with clear insights into the characteristics of the asteroid.

2.4. Dust particle dynamics

Numerous studies have been conducted to comprehend the behavior of dust in low-gravity conditions, exposed to solar wind and the strong gravitational irregularities caused by the non-spherical shape of asteroids. In Scheeres et al. [31] the fate of the dust around an asteroid is well summarized, identifying different classes of ejecta fate. Identifying stable, periodic orbits that can retain particles for extended periods, even up to several months, is critical for the safety of rendezvous operations and the potential collection of particles in orbit [35]. The Libration points, also known as Lagrange points, emerge from the three-body dynamics (CR3BP), especially for particle trajectories with an initial velocity near the escape velocity of the asteroid. As highlighted in Latino et al. [21], solar radiation influences the position of the Lagrangian points, particularly the L_2 point, which lies behind the asteroid concerning the Sun and varies depending on the dust size. The L_2 point for fine dust is positioned very close to the asteroid, while that for coarser particles is further away. A different model that exploits the change in mean orbital angular momentum and eccentricity over time is defined by Richter and Keller [27], and used in the study by Scheeres and Marzari [30] to evaluate the ejecta dynamics in the Deep Impact mission.

In the research work on the asteroid Ryugu, non-uniform gravitational fields, eclipses, and solar radiation are utilized to compute particle trajectories and examine the collisions between particles, particularly in the high-density dust areas immediately following the impact. Two additional phenomena are examined: the possible rebound of dust falling on the asteroid [21], which contributes to maintaining a high number of particles in orbit, and the uplift of particles around the asteroid caused by shock waves from the impact [25]. Different families of periodic orbits are identified in the works of Pinto et al. [40] and Kikuchi et al. [16]. The first reports Lyapunov planar orbits around the L_2 point, Distant Prograde Orbits (DPOs), and terminator orbits, while the second identifies planar elliptical orbits, elliptical orbits with high inclination, and terminator orbits. Dust

observations over time have focused on these types of orbits, which are more stable despite gravitational perturbations and solar radiation. The study was conducted for different particle sizes, which correspond to different levels of solar radiation pressure effect. Both studies indicate stable particle permanence for over 150 days.

In order to obtain a dynamic propagation of particles, it is necessary to have initial conditions of both position and velocity. To achieve this, a model of crater formation resulting from an impact were developed, as the parameters vary depending on the type of impact and the surface on which it occurs. Several laboratory tests have been reported in the literature, such as the work of Housen and Holsapple [10], which has produced one of the most commonly used models in this field. Another model, developed by Richardson at al. [25], has also been proposed as an alternative, and a study conducted by Trisolini at al. [38] has evaluated the differences between these models.

3 | Dynamics Model for Dust Particles in Low Gravity Environment

The environment around asteroids is complex, subject to solar radiation, solar tide and gravitational perturbations due to the non-uniform shape of the asteroid. Other nongravitational perturbations such as temperature ambalance, Yarkovsky effect, and gas pressure (important for the comets) are neglected in this work, due to their very low influence on dust dynamics. Particle collision, especially in the first minutes after impact, could have a greater influence on the dust trajectory than the other perturbations. Nevertheless, in the literature, this effect is used only for more sophisticated models, therefore it is also neglected in this study. Afterwards a generic impact on the asteroid's surface, the dust particles ejected from the surface would follow a purely ballistic path until they fall back on the asteroid itself or escape (if the speed of the particle exceeds the escape velocity). Nevertheless, the different perturbations make the particle trajectories chaotic, especially those with a velocity close to the escape velocity. As mentioned in Chapter 2, the results of some research conducted on the asteroid Ryugu have shown that for some initial conditions, there is the possibility that dust will remain in orbit around the body for over 5 months.

The Three-body problem is the most used to analyze this type of dynamics, which includes dust as the third body, the asteroid as the second body, and the Sun as the major attractor. The problem follows Newton's equations of gravity, but it does not have closed-form solution as in the case of the two-body problem. When the mass of the third body has a negligible gravitational attraction with respect to the first two bodies, Restricted Three-Body Problem (R3BP) is introduced, in which the main bodies (called primaries) orbit around the common center of mass, while the third body is affected by the gravity of the system without affecting it. A simplified model also includes circular orbits of the primaries around their common center of mass. If these assumptions are satisfied, the Three Body Problem becomes Circular Restricted Three Body Problem (CR3BP), from

which it is possible to obtain closed-form solutions, first given by Euler in 1767.

As seen in Yu et al. [43], the gravitational attraction of the planets can be considered as perturbations of dust dynamics. For NEOs, the planets with high degree of planetary tidal effect are Earth (due to its proximity) and Jupiter (due to its mass). Since the solar tide effect is about two orders of magnitude larger than other bodies, planetary tides can be neglected.

The model used is synthesized to have the equations useful for the propagation of dust particles. The synthesis comes from the work of Latino et al. [21]. The use of the gravitational field coefficient J_4 is a development implemented in this research compared to the one just mentioned. This addition was being used because as reported in Kikuchi et al. [16], Ryugu exhibits a strong zonal gravitational force associated with the J_4 term due to its spinning-top shape.

3.1. Solar radiation pressure

One of the most important sources of disturbance of particle motion is solar radiation. It is usually considered as a non-conservative force caused by the irradiation of photons emitted directly from the Sun. In the context of solar radiation, studies of heat dissipation and operating temperature ranges are also conducted, but this study focuses only on the effects of dynamics. The cannonball model is used, where a spherical object with the same optical properties is affected by the SRP. The albedo of Ryugu and the infrared radiation (IR) are not included in the model, both because of the low albedo value and for the low effect level on the particle dynamics, especially over short timescales.

Solar radiation contributes as acceleration, which must be included in the equations of motion. However, it is more convenient to insert it into the equations as the ratio between the SRP acceleration and the gravitational acceleration of the Sun. In this way, the lightness parameter β is obtained [21]:

$$\beta = \frac{P_0}{c}\frac{r_{es}^2}{\mu_{sun}}\frac{3}{2\rho_p d}c_R \tag{3.1}$$

where the solar flux $P_0 = 1367$ W/m^2 is taken at 1 AU away from the Sun, c is the speed of light and r_{es} is the Sun-Asteroid distance. In this study, the reference distance of the asteroid is set at 1 astronomical unit away from the Sun. The reflectivity coefficient is set to $c_R = 2$, corresponding to an ideal specular reflection, and the density $\rho_p = 1.19$ g/cm^3 is set equal to the mean density of Ryugu [41]. The presence of the particle diameter d

in the denominator indicates that the effect of solar radiation changes depending on the size of the hit particle. This will affect the position of Libration points as reported in Section 3.2.2. Furthermore, the eclipse effect is taken into account, when the parameter β is set equal to 0. This effect has important implications near the asteroid, during the first phase of dust cloud evolution. Important results are shown in Watanabe et al. [40], where periodic orbits change their shapes, especially near the L_2 point.

3.2. Circular Restricted Three Body Problem

As stated before, Circular Restricted Three Body Problem (CR3BP) is the simplified the dynamics of the case study with a low computational cost, and guarantees closed-form solutions (the model is extensively studied in Szebehely [34]). CR3BP can be simplified even better by setting a rotating reference frame (synodic reference frame), in which the primaries have fixed position in space, as in Figure 3.1. In this way the time invariant equations of motion are obtained.

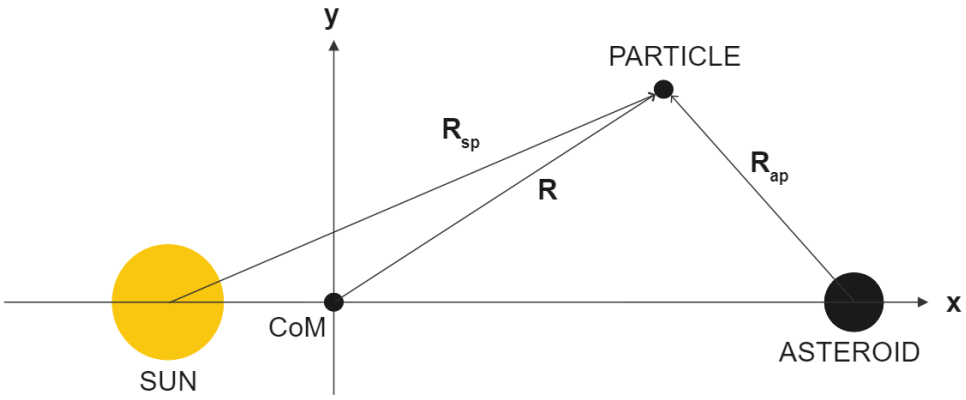

Figure 3.1: Sun-Asteroid system in synodic reference frame.

The angular velocity of the reference system will be equal to the primaries orbital velocity around the center of mass, with which the centripetal force balances the gravitational force:

$$\omega = \sqrt{\frac{G(m_s m_a)}{r_{es}^3}} \tag{3.2}$$

The angular velocity ω is essential to pass from a sidereal to a synodic reference system, nevertheless, in this study the equations in the sidereal reference frame are not reported, since they are not necessary for the development of the model. In the following sections,

the synodic dimensionless equations of motion are obtained by reporting the main steps studied in Latino et al. [21].

3.2.1. Dimensionless synodic equation of motion

The already amply investigated nondimensional photo-gravitational CR3BP is used for the formulation of the equations of motion. For clarity of wording and nomenclature, the dimensionless values are reported in lowercase letters and obtained with the parameters in Table 3.1. The first step is to calculate adimensional mass parameter μ to model the system where the investigated ejecta dust is generated:

$$\mu = \frac{m_a}{m_s + m_a} \tag{3.3}$$

where m_a and m_s are the asteroid mass and the solar mass respectively. Due to the following dimensionless ness, the angular velocity is equal to unity: $\bar{n} = 1$ rad$/\tau$.

Normalisation parameters	
Length unit (l)	1.19 AU
Mass unit (M)	1.989 $\times 10^{30}$ kg
Time unit (τ)	6.516592779 $\times 10^{6}$ s
Velocity unit (v)	27.32 km/s

Table 3.1: Normalisation parameters for the Sun-Ryugu system [21]. Length unit l is simply taken from the average distance between Sun and Ryugu. Mass unit M is the sum of the two primaries masses. Time unit τ corresponds to one revolution of Ryugu. Velocity unit v is the mean velocity of Ryugu around the Sun.

Therefore, to obtain dimensionless position and velocity, it is enough to divide the vectors by the normalisation parameters of Table 3.1 (reported in Figure 3.2):

$$\boldsymbol{r} = \frac{\boldsymbol{R}}{l}, \qquad \dot{\boldsymbol{r}} = \frac{\dot{\boldsymbol{R}}}{v} \tag{3.4}$$

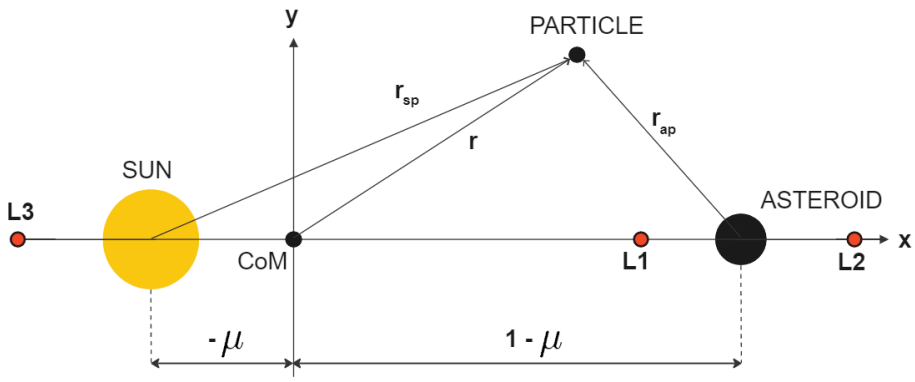

Figure 3.2: Adimensional Sun-Asteroid system.

The potential V is used to write the equations of motion in compact form. It is the sum of the gravitational contribution of the two primaries, the rotating system contribution, and the solar radiation contribution [32]:

$$V = \frac{1}{2}(x^2 + y^2) + \frac{(1-\beta)(1-\mu)}{r_{sp}} + \frac{\mu}{r_{ap}} \tag{3.5}$$

where r_{sp} is the adimensional Sun-particle distance and r_{ap} is the adimensional asteroid-particle distance, expressed in synodic frame:

$$\begin{aligned} r_{sp} &= \sqrt{(x+\mu)^2 + y^2 + z^2} \\ r_{ap} &= \sqrt{(x+\mu-1)^2 + y^2 + z^2} \end{aligned} \tag{3.6}$$

Then the compact equations of motion are written for the non-dimensional photo-gravitational CR3BP:

$$\begin{cases} \ddot{x} - 2\dot{y} = V_{/x} \\ \ddot{y} + 2\dot{x} = V_{/y} \\ \ddot{z} = V_{/z} \end{cases} \tag{3.7}$$

Where the derivatives of the potential for each direction are thus computed:

$$
\begin{aligned}
V_{/x} &= x - \frac{(1-\beta)(1-\mu)}{r_{sp}^3}(x+\mu) - \frac{\mu}{r_{ap}^3}(x+\mu-1) \\
V_{/y} &= y - \frac{(1-\beta)(1-\mu)}{r_{sp}^3}y - \frac{\mu}{r_{ap}^3}y \\
V_{/z} &= -\frac{(1-\beta)(1-\mu)}{r_{sp}^3}z - \frac{\mu}{r_{ap}^3}z
\end{aligned}
\tag{3.8}
$$

3.2.2. Libration points

Since the problem is expressed in a rotating frame (synodic reference frame), it has no explicit time dependence, which therefore implies the possibility of time-invariant equilibrium points solution. Such solutions are characterized by a stationary position and velocity in the synodic frame, proved by Lagrange (1772). There are three collinear points along the primaries line (L_1 between the asteroid and the Sun, L_2 behind the asteroid and L_3 behind the Sun) and two equilateral points, symmetric with respect to the x-axis (Figure 3.3). Zero velocity and zero acceleration with respect to the rotating frame are the necessary conditions to have the equilibrium points. To obtain them, it is enough to equate the left-hand side of the Eqs. (3.7) to zero.

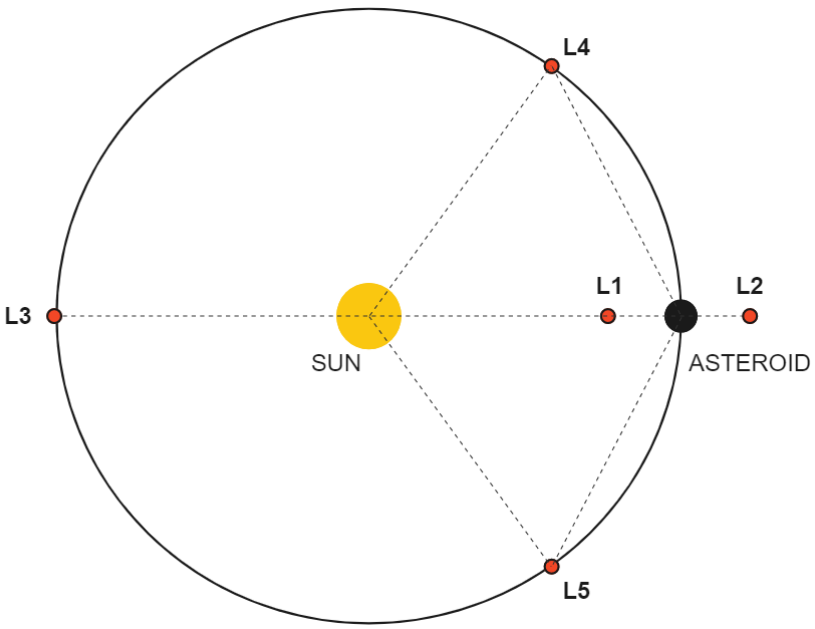

Figure 3.3: Lagrangian points Sun-Ryugu system.

As seen in Section 3.1, particle size affects the β parameter, which in turn modifies the equilibrium condition in the equations of motion. Thus, the Lagrangian points are

expected to change position. Figure 3.4 shows how the effect of solar radiation moves the three collinear points L_1, L_2, and L_3 towards the center of mass. The effect is more pronounced for finer particles (with a larger beta parameter). As seen in Latino et al. [21], for particles with diameters equal to 19 µm, the Lagrangian point L_2 touches the surface of the asteroid, referred to the Sun - Ryugu system.

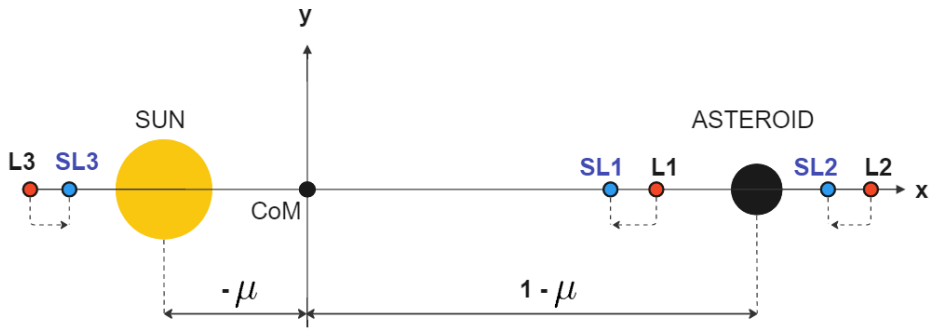

Figure 3.4: Lagrangian points with β effect.

3.2.3. Jacobi integral and Hill's regions

The CR3BP has the so call Jacobi integral of motion (1836). Its very simple derivation cames form the work of Latino et al. [21] is reported in this study. Starting from a scalar combination of the dynamic variables and considering only the solar radiation pressure:

$$\dot{x}\ddot{x} + \dot{y}\ddot{y} + \dot{z}\ddot{z} = \dot{x}(2\dot{y} + V_{/x}) + \dot{y}(-2\dot{x} + V_{/y}) + \dot{z}V_{/z} \quad = \frac{dV}{dt} \tag{3.9}$$

Observing that

$$\dot{x}\ddot{x} + \dot{y}\ddot{y} + \dot{z}\ddot{z} = \frac{d}{dt}\frac{1}{2}(\dot{x}^2 + \dot{y}^2 + \dot{z}^2) \quad = \frac{dV}{dt} \tag{3.10}$$

Integrating the second and the third term of the previous equation:

$$\frac{1}{2}(\dot{x}^2 + \dot{y}^2 + \dot{z}^2) = V(x, y, z) - \frac{C}{2} \tag{3.11}$$

Where C is the so call Jacobi constant. For its complete expression it is sufficient to substitute the potential V of the equation 3.5 in the previous equation:

$$C = x^2 + y^2 + \frac{2(1-\beta)(1-\mu)}{r_{sp}} + \frac{2\mu}{r_{ap}} - (\dot{x}^2 + \dot{y}^2 + \dot{z}^2) \tag{3.12}$$

The constant C represents the energy level of a given particle in orbit in the system, and remains constant during the motion. Consequently, it is possible to calculate the particle velocity at any position, that is the last term of the Eqs. 3.12. By setting the speed equal to 0, it is possible to obtain the boundary beyond which the given particle cannot cross, since in this boundary the particle arrives with a speed equal to 0 ($v^2 < 0$ has no physical meaning), for each value of C. In the case of a too high C value, the particle never comes to rest, running away from the system. This concept was used by Hill to introduce the concept of zero velocity curves.

Figure 3.5a shows qualitatively the value of the potential in the Sun-Ryugu system ($\mu = 2.25 \times 10^{-19}$). Since the mass of the asteroid is too small compared to the Sun, the Lagrangian points L_1 and L_2 appear to overlap. To show in more detail the arrangement of the Lagrangian points and the potential, in Figure 3.5b the Earth-Moon system is shown ($\mu = 0.0122$).

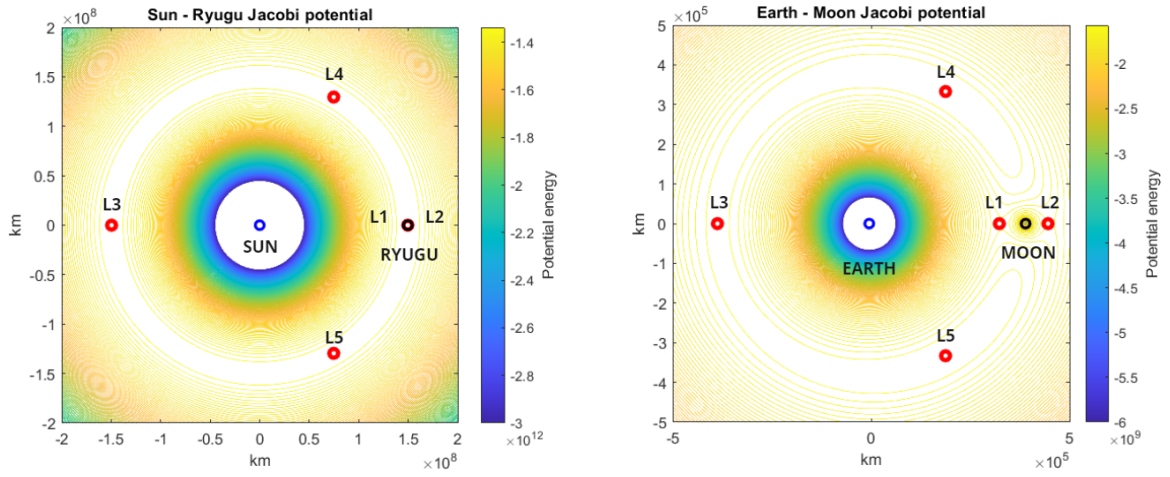

(a) Potential of the Sun-Ryugu system ($\mu = 2.25 \times 10^{-19}$).

(b) Potential of the Earth-Moon system ($\mu = 0.0122$).

Figure 3.5: Gravitational potential contour line.

The zero velocity curve gives us useful information on the positions that can be reached at a certain energy level C. The figure 3.3 shows different energy levels the object possesses in orbit in the Earth - Moon system. The C_1 value refers to the minimum energy required to arrive at the Lagrangian point L_1 with a velocity equal to 0. As well as C_2, C_3, C_4 and C_5. Depending on the initial conditions, the energy level C can provide information on the fate of the object in orbit, such as its permanence or escape from the system. In the case of $C = C_1$, a small increase in energy level allows the object to switch between

domains around the primaries. If the energy level is big enough, the object is allowed to go virtually anywhere, as can be seen in the last plot of Figure 3.3.

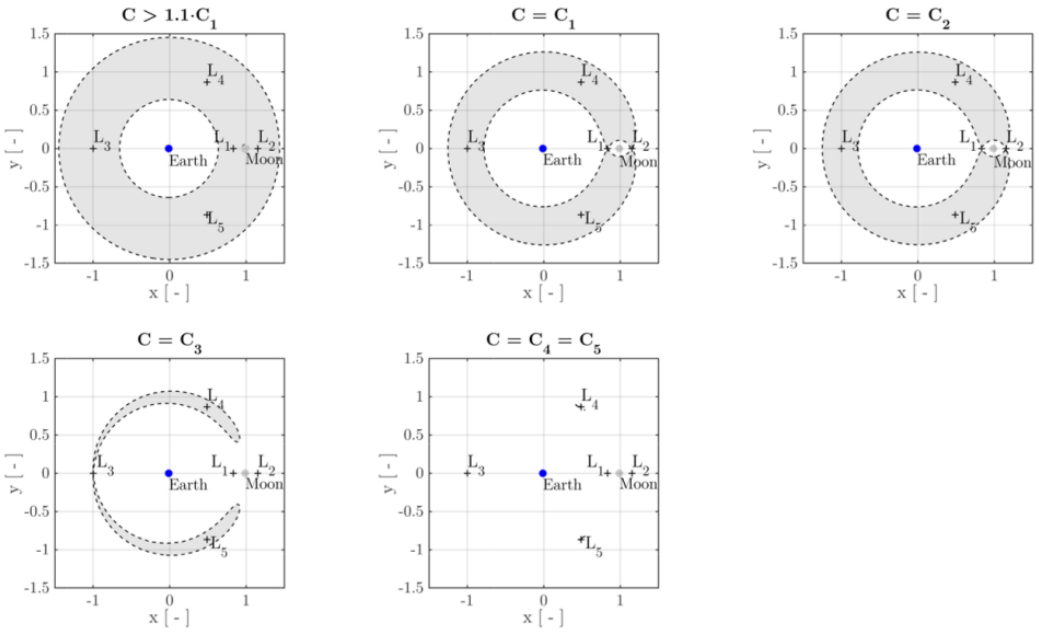

Figure 3.6: Zero velocity curve Earth - Moon system ($\beta = 0.02$) [21].

3.3. Gravity perturbations

The irregular shape and distribution of mass and density of the asteroids should be considered to better model the particle dynamics. Obviously, the resulting gravitational field becomes more complicated to model. Furthermore, most of the data available on asteroids comes from Hayabusa2 missions, which approached the asteroid until it touched its surface. In order to consider the irregular shape of a body, different types of solutions have been developed over time, including the spherical harmonics (aspherical potential), triaxial ellipsoid, polyhedral and Mascon (point mass) models. In the study of an asteroid about a kilometer in size, as in the case of Ryugu, the resulting gravitational attraction is very small, and the gravitational perturbations are relevant only a few radii away from the asteroid itself. It is important to remember that the influence of solar radiation is very large, especially for very small particles (most of the particles produced by an impact).

Following again the equations derivation of Latino et al. [21], spherical harmonics tool is used to model the irregular shape of Ruygu. General formulation came from Kaplan (1976), Lambeck (1988) and others. If the $J_{l,m}$ gravity filed coefficient is used, it is possible to write the gravitational potential energy with the 0^{th} order term separated

from the zonal and the tesseral harmonics:

$$V = \frac{\mu}{r}\left(1 - \sum_{l=2}^{\infty} J_l \left(\frac{R}{r}\right)^l P_l + \right. \\ \left. + \sum_{l=2}^{\infty}\sum_{m=1}^{\infty} \left(\frac{R}{r}\right)^l P_{l,m}\Big(C_{l,m}cos(m\alpha) + S_{l,m}sin(m\alpha)\Big)\right) \tag{3.13}$$

Where $r = \sqrt{x^2 + y^2 + z^2}$ is the distance form the attractive body, R is the reference radius of attractor, α is the particle longitude, $P_{l,m} = P_{l,m}(cos(\eta))$ are the associated Legendre polynomials (whit $m = 0$, $P_{l,m}$ become the conventional Legendre polynomials) and $C_{l,m}$ and $S_{l,m}$ are the gravity field coefficients ($J_l = -C_l$). Terms with $m = 0$ are called zonal coefficients, since they do not depend on the longitude. Terms with $m < l$ are called tesseral coefficients, while the sectorial coefficients have $m = l$. In the case with the attractive body's center of mass is the centre of the coordinate system, $C_{1,0} = S_{1,0} = C_{1,1} = 0$. The expression of the harmonic coefficients up to $C_{4,4}$ are computed as follows [21]:

$$\begin{aligned} C_{2,0} &= \frac{1}{5R^2}\left(c^2 - \frac{a^2+b^2}{2}\right) = -0.008347066115702 \\ C_{2,2} &= \frac{1}{20R^2}(a^2 - b^2) = 0.001556342975207 \\ C_{4,0} &= \frac{15}{7}(C_{2,0}^2 + 2C_{2,2}^2) = 0.000159681256398 \\ C_{4,2} &= \frac{5}{7}C_{2,0}C_{2,2}^2 = -0.000009279212651 \\ C_{4,4} &= \frac{5}{28}C_{2,2}^2 = 0.00000043253633 \end{aligned} \tag{3.14}$$

Where dimensions $a \geq b \geq c$ are referred to the triaxial ellipsoid. The conventional Legendre polynomial are well expressed with the Rodrigues' formula (1816):

$$P_l(\nu) = \frac{1}{2^l l!}\frac{d^l}{d\nu^l}(\nu^2 - 1)^l \tag{3.15}$$

The associated Legendre polynomials $P_{l,m}$ (equal to zero if $m > l$) instead, follow the next expression:

$$P_{l,m} = (1 - \nu^2)^{\frac{m}{2}}\frac{d^m}{d\nu^m}P_l(\nu) \tag{3.16}$$

3.3.1. Effect of J2 and J4 on the equations of motion

In this study, the use of J_4 gravity field coefficients is chosen with a trade-off between computational cost and model sophistication. As already stated, the procedure for obtaining the equations is taken from Latino et al. [21], in which however only J_2 is implemented. The first step is to compute the conventional Legendre polynomial P_2 and P_4 from Eq. (3.15):

$$\begin{aligned} P_{2,0} = P_2 &= \frac{1}{2}(3\nu^2 - 1) \\ P_{4,0} = P_4 &= \frac{1}{8}(35\nu^4 - 30\nu^2 + 3) \end{aligned} \tag{3.17}$$

Here ν is substituted for geocentric latitude as follows:

$$\nu = \sin(\eta) = \frac{z}{r} \tag{3.18}$$

Where η is the particle latitude. Using the reference system reported in section 3.2.1, thus using the adimensional Sun-particle distance r_{sp} and asteroid-particle distance r_{ap}, the complete expression of the potential is obtained:

$$\begin{aligned} V = &\frac{1}{2}(x^2 + y^2) + \frac{(1-\beta)(1-\mu)}{r_{sp}} + \frac{\mu}{r_{ap}} - \frac{\mu}{r_{ap}} J_2 \left(\frac{R}{r_{ap}}\right)^2 \frac{1}{2}\left(3\left(\frac{z}{r_{ap}}\right)^2 - 1\right) + \\ &- \frac{\mu}{r_{ap}} J_4 \left(\frac{R}{r_{ap}}\right)^4 \frac{1}{8}\left(35\left(\frac{z}{r_{ap}}\right)^4 - 30\left(\frac{z}{r_{ap}}\right)^2 + 3\right) \end{aligned} \tag{3.19}$$

Now the derivative of the potential in all three directions must be calculated. Since $V = V(r, \eta)$, the rule of the chain of derivatives of several variables is required:

$$\begin{cases} \dfrac{\partial V}{\partial x} = \dfrac{\partial V}{\partial r}\dfrac{\partial r}{\partial x} + \dfrac{\partial V}{\partial \eta}\dfrac{\partial \eta}{\partial x} \\ \dfrac{\partial V}{\partial y} = \dfrac{\partial V}{\partial r}\dfrac{\partial r}{\partial y} + \dfrac{\partial V}{\partial \eta}\dfrac{\partial \eta}{\partial y} \\ \dfrac{\partial V}{\partial z} = \dfrac{\partial V}{\partial r}\dfrac{\partial r}{\partial z} + \dfrac{\partial V}{\partial \eta}\dfrac{\partial \eta}{\partial z} \end{cases} \tag{3.20}$$

Where the position and latitude derivatives over the three direction are equal to:

$$\begin{aligned}
\frac{\partial r}{\partial x} &= \frac{x}{r} & \frac{\partial \eta}{\partial x} &= -\frac{xz}{r^2\sqrt{x^2+y^2}} \\
\frac{\partial r}{\partial y} &= \frac{y}{r} & \frac{\partial \eta}{\partial y} &= -\frac{yz}{r^2\sqrt{x^2+y^2}} \\
\frac{\partial r}{\partial z} &= \frac{z}{r} & \frac{\partial \eta}{\partial z} &= \frac{\sqrt{x^2+y^2}}{r^2}
\end{aligned} \tag{3.21}$$

As shown in Latino et al. [21], the derivatives of the potential along the three spatial directions can be generalized for zonal harmonics (m = 0) as follows:

$$\begin{aligned}
\frac{\partial V}{\partial r} &= -\frac{\mu}{r^2}\left(1 - \sum_{l=2}^{\infty} J_l \left(\frac{R}{r}\right)^l (l+1) P_l\right) \\
\frac{\partial V}{\partial \phi} &= -\frac{\mu}{r} \sum_{l=2}^{\infty} J_l \left(\frac{R}{r}\right)^l P_{l,1}
\end{aligned} \tag{3.22}$$

It can be seen in Eqs. (3.23) how the derivative of the potential over the latitude also depends on the Legendre polynomials with parameter $m = 1$. To obtain the derivatives, $P_{2,1}$ and $P_{4,1}$ are computed next:

$$\begin{aligned}
P_{2,1} &= 3\cos(\eta)\sin(\eta) \\
P_{4,1} &= \frac{5}{2}\cos(\eta)(7\sin(\eta)^4 - 3\sin(\eta))
\end{aligned} \tag{3.23}$$

Substituting Eqs. (3.23) in Eqs. (3.22) the following expressions are obtained:

$$\begin{aligned}
\frac{\partial V}{\partial r} &= -\left(1 - \frac{3}{2} J_2 \left(\frac{R}{r}\right)^2 (3\sin(\eta)^2 - 1) + \right. \\
&\quad \left. - \frac{5}{8} J_4 \left(\frac{R}{r}\right)^4 (35\sin(\eta)^4 - 30\sin(\eta)^2 + 3)\right)\frac{\mu}{r^2} \\
\frac{\partial V}{\partial \eta} &= -\left(J_2 \left(\frac{R}{r}\right)^2 3\sin(\eta)\cos(\eta) + \right. \\
&\quad \left. - \frac{5}{2} J_4 \left(\frac{R}{r}\right)^4 (\cos(\eta)(7\sin(\eta)^3 - 3\sin(\eta))\right)\frac{\mu}{r}
\end{aligned} \tag{3.24}$$

The derivatives just found are for the gravitational contributions of the potential, without SRP contribution. From Eqs. (3.19) V_J, the gravitational contributions of the potential, is taken:

$$
\begin{aligned}
V_J = &-\frac{\mu}{r} J_2 \left(\frac{R}{r}\right)^2 \frac{1}{2}\left(3\left(\frac{z}{r}\right)^2 - 1\right) + \\
&- \frac{\mu}{r} J_4 \left(\frac{R}{r}\right)^4 \frac{1}{8}\left(35\left(\frac{z}{r}\right)^4 - 30\left(\frac{z}{r}\right)^2 + 3\right)
\end{aligned}
\tag{3.25}
$$

Then the spatial derivatives of the potential are obtained:

$$
\begin{aligned}
\frac{\partial V_J}{\partial x} &= \left(\frac{3}{2} J_2 \left(\frac{R}{r}\right)^2 \left(5\left(\frac{z}{r}\right)^2 - 1\right) + \right. \\
&\left. + \frac{5}{8} J_4 \left(\frac{R}{r}\right)^4 \left(7\left(\frac{z}{r}\right)^4 - 18\left(\frac{z}{r}\right)^2 + 3\right)\right) \frac{\mu}{r^3}(x + \mu - 1) \\
\frac{\partial V_J}{\partial y} &= \left(\frac{3}{2} J_2 \left(\frac{R}{r}\right)^2 \left(5\left(\frac{z}{r}\right)^2 - 1\right) + \right. \\
&\left. + \frac{5}{8} J_4 \left(\frac{R}{r}\right)^4 \left(7\left(\frac{z}{r}\right)^4 - 18\left(\frac{z}{r}\right)^2 + 3\right)\right) \frac{\mu}{r^3} y \\
\frac{\partial V_J}{\partial z} &= \left(\frac{3}{2} J_2 \left(\frac{R}{r}\right)^2 \left(5\left(\frac{z}{r}\right)^2 - 3\right) + \right. \\
&\left. + \frac{5}{8} J_4 \left(\frac{R}{r}\right)^4 \left(31\left(\frac{z}{r}\right)^4 + 10\left(\frac{z}{r}\right)^2 - 13\right)\right) \frac{\mu}{r^3} z
\end{aligned}
\tag{3.26}
$$

In the case of non-uniform attractive mass, the adimensional mean motion is not equal to the unity like before. The expression is obtained by dividing for the unit of mass $(m_s + m_a)$, the unit of length (the mean Sun - Ryugu distance R_0) and taking the universal gravitational constant $G = 1$ (due to the adimensionalization), as reported in Latino et al. [21].

$$
\bar{n} = 1 + \frac{3}{2} J_2 \left(\frac{R}{R_0}\right)^2 - \frac{15}{8} J_4 \left(\frac{R}{R_0}\right)^4 \tag{3.27}
$$

The equations of motion used in this study are finally obtained, written in compact form:

$$
\begin{cases}
\ddot{x} - 2\bar{n}\dot{y} = V_{/x} \\
\ddot{y} + 2\bar{n}\dot{x} = V_{/y} \\
\ddot{z} = V_{/z}
\end{cases}
\tag{3.28}
$$

Where the right-hand terms are the potential derivatives, where the distance from the attractor r is replaced with the dimensionless asteroid - particle distance r_{ap}:

$$
\begin{aligned}
V_{/x} &= x - \frac{(1-\beta)(1-\mu)}{r_{sp}^3}(x+\mu) - \frac{\mu}{r_{ap}^3}(x+\mu-1) + \frac{\partial V_J}{\partial x} \\
V_{/y} &= y - \frac{(1-\beta)(1-\mu)}{r_{sp}^3}y - \frac{\mu}{r_{ap}^3}y + \frac{\partial V_J}{\partial y} \\
V_{/z} &= -\frac{(1-\beta)(1-\mu)}{r_{sp}^3}z - \frac{\mu}{r_{ap}^3}z + \frac{\partial V_J}{\partial z}
\end{aligned}
\tag{3.29}
$$

4 | Initial condition and crater formation

In Chapter 3, the dynamic model of particles in a low gravity environment has been implemented. This chapter deals with the initial conditions of the dust following the impact, with the relative crater formation. The various laboratory studies combined with real impact observations have contributed to the creation of various models, the first of which is the Housen and Holsapple model [10], used in this work. Their research lists many laboratory studies conducted in vacuum under Earth's gravity. In order to use the data obtained from the laboratory tests it was necessary to implement an ejecta scaling law, with the point source approximation of the projectile impacting, which is a good approximation for hypervelocity impacts. In this study, the Richardson model [25] is also used, for which the crater formation and particle departure time depending on the distance from the impact are obtained. This second model results differ in some aspects compared to the first mentioned, as studied in Trisolini et al. [38].

Spectral observations, gravitational field studies, and observations of dust from an asteroid impact, as seen in Section 2.1, are helpful in identifying the type of surface. This chapter will also deal with the surface typology of the asteroid Ryugu and the physical characteristics of the impactor, to obtain a complete event characterization and for obtaining the initial conditions of the ejecta dust.

4.1. Impact on Ryugu surface

The crater formation model needs information about the asteroid surface where the crater forms and the characteristics of the impactor. Information about Ryugu comes from the Hayabusa2 mission, which performed close-up observations and a small impact experiment on the asteroid's surface.

4.1.1. Impactor

As seen in section 2.1, the different asteroid and comet impact missions have implemented different solutions, using either the spacecraft itself as an impactor (this is the case of the Dart mission), or using parts of it as a projectile (as in the case of Hayabusa2). In this study, the goal is to explore the various aspects and constraints on the ejecta dust observability from a probe stationed around the asteroid, as in the case of Hayabusa2. For this reason, the impactor was chosen with the same characteristics, especially the impact velocity, as the one already tested in the Hayabusa2 mission [29]. The main characteristics of the impactor used in this study are shown in Table 4.1.

Impactor	
Impactor velocity U	2 km/s
Impactor radius a	7.5 cm
Impactor density δ	2.7 g/cm^3
Impactor mass m	4.7713 kg

Table 4.1: Impactor main characteristics [29].

The implementation of an impactor with different characteristics, especially the impact mass and velocity, affect the dynamics of the event which could be too risky for a probe orbiting the asteroid itself. The use of a small impactor is therefore forced by the research aim.

4.1.2. Asteroid surface

As seen in the Section 2.2, the studies on the asteroid and the images of the impact conducted by the Hayabusa2 mission have cataloged the type of surface as sand soil, with non-cohesive or very low cohesion material. For this reason, the impacts on its surface occur under gravity regime, as shown in the pictures in Figure 2.4. The impact categorization is important to define all parameters used in the crater formation model, and to obtain the particle ejecta initial conditions. Table 4.2 shows the constants relating to the ejecta model with gravity-dominated impacts.

Crater formation parameters		
H_1	0.59	Housen & Holsapple model
C_1	0.55	Housen & Holsapple model
μ	0.41	Housen & Holsapple model
ν	0.4	Housen & Holsapple model
n_1	1.2	Housen & Holsapple model
n_2	1.3	Housen & Holsapple model
k	0.3	Housen & Holsapple model
K_1	0.24	Richardson model
K_{tg}	0.8	Richardson model

Table 4.2: Gravity domain ejecta model constants of sand-like asteroid surface of different models [10] [25].

4.2. Ejecta model

This section shows the useful parameter formulations for ejecta initial condition modeling and the crater formation. The model widely used in the field of crater formation is the one developed by Housen and Holsapple [10]. Richardson model [25], whose results have been compared to the first one in Trisolini et al. [38], is used in this work for crater formation times computation. Both models have a formulation for the gravity regime and strength regime impact. The following expressions are all associated with a gravity regime impact.

The objective is to obtain the ejecta velocity depending on the distance from the impact site x. First of all, the final crater radius is obtained as follows [10]:

$$R_c = H_1 \left(\frac{\rho}{\delta}\right)^{\frac{2+\mu-6\nu}{6+3\mu}} \left(\frac{ga}{U^2}\right)^{-\frac{\mu}{2+\mu}} \left(\frac{\rho}{m}\right)^{-\frac{1}{3}} \tag{4.1}$$

Where H_1, C_1, ν and μ are ejecta model constants listed in Table 4.2, g is the surface gravity, ρ is the asteroid density and U, δ, m and a are impactor parameters listed in Table 4.1. It is therefore possible to obtain the speed as a function of the distance from the point of impact x up to R_c [10]:

$$u_p = C_1 U \left(\frac{x}{a}\left(\frac{\rho}{\delta}\right)^{\nu}\right)^{-\frac{1}{\mu}} \tag{4.2}$$

In this way, the ejecta velocity is applied to the particle with a given orientation (always taken radial with respect to the center of impact) and an inclination that will be studied later. Now the Richardson model is applied to study the crater formation time [25]:

$$T = K_{Tg}\sqrt{\frac{V_c^{\frac{1}{3}}}{g}} \tag{4.3}$$

Where K_{tg} and K_1 are ejecta model constants listed in Table 4.2. V_c is the total crater volume computed as [25]:

$$V_c = K_1\left(\frac{m}{\rho}\right)\left(\frac{ga}{U^2}\right)^{-\frac{3\mu}{2+\mu}}\left(\frac{\rho}{\delta}\right)^{\frac{\mu}{2+\mu}} \tag{4.4}$$

It must be kept in mind that the formulation of the Richardson model derives in part from Housen and Holsapple model. Hence the reason for the similarity of the expressions. The model allows to calculate the starting position of the particles as a function of the time elapsed since the impact t [25]:

$$x = K_{Tg}^{-\frac{\mu}{\mu+1}} R_c\left(t\sqrt{\frac{g}{R_c}}\right)^{\frac{\mu}{\mu+1}} \tag{4.5}$$

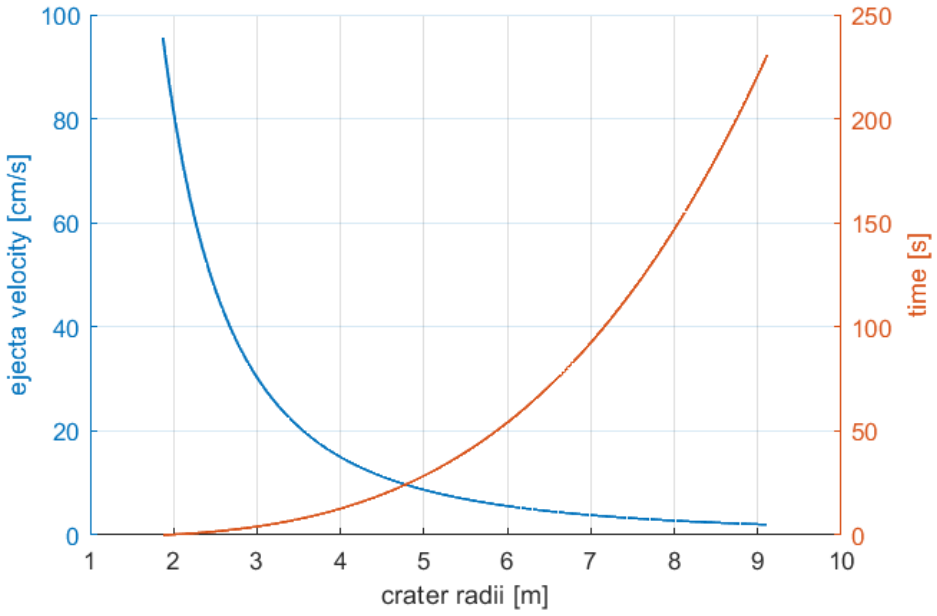

Figure 4.1: Crater formation with impactor of Table 4.1.

Taking as reference the impactor selected in Section 4.1.1 and the Ryugu surface features listed in Section 4.1.2, a crater of 9.1 meters in radius is obtained from the model. The value agrees with the real SCI crater (8.8 ± 0.7 meters [1]). The crater formation time, on the other hand, stands at 235 seconds, a very long time as expected, due to the impact in the gravity regime. The velocity of ejecta versus location and the advancement of the crater versus time are shown in Figure 4.1. From the figure, it can be seen how close to the impact point no data is reported. due to the high speed (> 90 cm/s) of the ejecta particles close to the impact, In addition, it should be noted that according to the model, the first meter of the crater forms at the same time as the impact, partly due to the impactor which blocks the dust up to a distance of $n_1 = 1.2$ times the radius of the impactor from the impact point [10].

4.2.1. Ejecta inclination and orientation

The initial inclination of the particles is still a debated topic. In the literature, it is possible to find assumptions of a constant inclination for all particles [9], the Maxwell Z-model implementation, which links the inclination to a parameter Z [23], or ejection angle distribution functions [38]. The only widely agreed condition is the inclination decrease at greater distances from the impact point, but the decrease trend is still an area of study. As reported in Richardson et al. [25], a monotonic function is assumed to model the inclination of the particles as a function of the distance from the impact location:

$$\gamma(x) = \gamma_0 - \gamma_d\left(\frac{x}{R_c}\right) \tag{4.6}$$

Where γ_0 is the starting angle, and γ_d is the total drop angle, which is corrected after a series of iterations. With the same approximation used in Richardson et al. [25], the initial iteration values from laboratory studies are used (as reported in Cintala et al. [3]):

$$\begin{aligned} \gamma_0 &= 52,4^\circ \pm 6,1^\circ \\ \gamma_d &= 18,4^\circ \pm 8,2^\circ \end{aligned} \tag{4.7}$$

To give more randomness to the ejecta dust, a randomization of the orientation angle with respect to the ground is implemented, with a more or less dense discretization, depending on the number of particles to be used for image generation.

4.2.2. Asteroid rotation

Also the rotation of the asteroid is considered to set the initial conditions of each individual particle. The starting speed is set as the speed obtained in Eq. (4.2) (decomposed in the direction obtained by inclination in Eq. (4.6)) added to the speed of the asteroid surface at the particle starting point:

$$\boldsymbol{u_{ej}} = \boldsymbol{u_p} + \boldsymbol{v_{rot}} \tag{4.8}$$

Where the surface velocity at each point is found as follow:

$$\boldsymbol{v_{rot}} = \frac{\omega_{asteroid}}{R} cos(\eta_p)[cos(\alpha_p + \pi/2); sin(\alpha_p + pi/2); 0] \tag{4.9}$$

The asteroid rotation period $\omega_{asteroid}$ is equal to 7.63262 hours [18], while α_p and η_p are respectively the longitude and latitude of the particle's starting point.

4.2.3. Particle size

Particle size is the only parameter in literature that is not linked to any other impact-related variable. Consequently, it is legitimate to use a cumulative distribution function which decreases the number of particles as the size increases. However, the starting speed of individual particles can be related to their size. In Trisolini et al. [38] the number of representative fragments in the size-speed distribution is evaluated, where small-sized and low-velocity particles are the most frequent, while large-sized and high-velocity ones are the rarest. This study is limited to the sizing of powders with a cumulative distribution function [17]:

$$G_d = N_r d^{-\bar{\alpha}} \tag{4.10}$$

Where N_r is a multiplicative factor, $d_{min} \leq d \leq d_{max}$ is the particle size and $\bar{\alpha}$ is the slope exponent of the power law. The minimum and maximum width of the particles is arbitrary. In literature, the most common values range from $10 - 100$ µm to $1 - 10$ cm. N_r is obtained by the conservation of mass [38]:

$$N_r = \frac{3(3 - \bar{\alpha})M_{tot}}{4\bar{\alpha}(d_{max}^{3-\bar{\alpha}} - d_{min}^{3-\bar{\alpha}})\pi\rho} \tag{4.11}$$

When the total mass ejected M_{tot} derives from Housen and Holsapple model [10]:

$$M_{tot} = k\rho[(n_2 R_c)^3 - (n_1 a)^3] \tag{4.12}$$

Where k, n_1 and n_2 are ejecta model constants reported in Table 4.2. The selection of the $\bar{\alpha}$ parameter is mainly based on observations of impacts in similar environments (same gravitational attraction and/or same distance from the Sun). As reported in Krivov et al. [17], the value of alpha for basalt and granite targets varies between 2.4 and 2.7. Preliminary studies on the images relating to the Dart mission show how the coefficient settles on the value of 2.7 for particles of 1 µm - a few mm radius and reaches up to 3.7 for larger particles up to a few cm. In this research, the $\bar{\alpha}$ parameter is set to 2.7 (the most common data in the literature for this impact types).

5 | Image simulation and spacecraft positioning for robust image acquisition

The aim of this study is to develop a simulated image model for the ejecta dust generated by an impact on an asteroid's surface. For this purpose, it is necessary to implement an image acquisition model consistent with the specifics required by the event and with the technical characteristics of the selected cameras. In this chapter, the model implementation is presented, with particular attention on the camera pointing, the solar radiation reflected by the plume, and the diffraction of the light into the optical instrument. Since the chosen cameras have already been tested in space missions, the need to develop a complex optical system aimed at mitigating the various aberrations was not of great importance. For this reason, the developed optical system is a simple pinhole model.

Furthermore, the spacecraft location at the moment of impact and in the following instants is essential for its safety, due to the high-speed impact of ejecta particles, and for obtaining images useful for the purpose. Studies of this kind have been addressed, especially for the safety and for the collectability of dust directly in orbit around the asteroid, as in the work of Trisolini [37].

The possibility of having one or more landers on the surface of the asteroid, as in the case of MASCOT in the Hayabusa2 mission [20], could lead to useful data for observing the dust cone from the surface itself. In this study, therefore, the possibility of having landers on the asteroid and the obtainable images from surface are studied in the next chapters.

5.1. Image acquisition model

In this section, the optical system and the methods for obtaining the simulated image are developed. The optical system implemented is the Pin-hol model, which consists of a simple infinitesimal aperture and a detector placed at a distance u, called focal distance,

as shown in Figure 5.1. Detectors have a certain number of pixels, but usually, only the inner ones are used to obtain the image. In this case, working with the ideal pinhole model, the detector is modeled on the actual number of pixels that are used. The length of the detector L will therefore be equal to the number of pixels per side n_{px} multiplied by their size d_{px}. Furthermore, in literature, it is usual to find the Field of View (FOV) angle of the camera, while the focal length refers to the system of lenses that the camera carries with it. Consequently, the focal distance u is calculated as follows:

$$u = \frac{L}{2}\frac{1}{\tan(\theta_{FOV})} \tag{5.1}$$

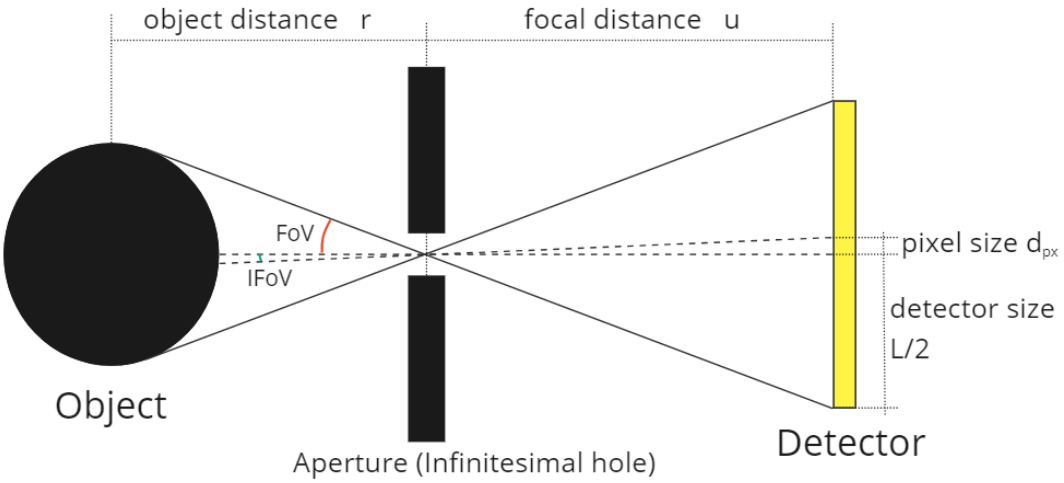

Figure 5.1: Pin-hole model.

Now, it is useful to develop a new reference system, called camera reference frame, different from the synonic reference frame seen in Chapter 3: the pointing direction of the camera is equivalent to the x-axis of the new reference system, as shown in Figure 5.2a. While in Figure 5.2b the reference system of the detector is obtained with a simple rigid translation on the negative x_o-axis. The latter reference system is useful for positioning the pixels in 2D detector space, which ranges from $-L/2$ to $L/2$ on the y_d and z_d axes of the detector frame.

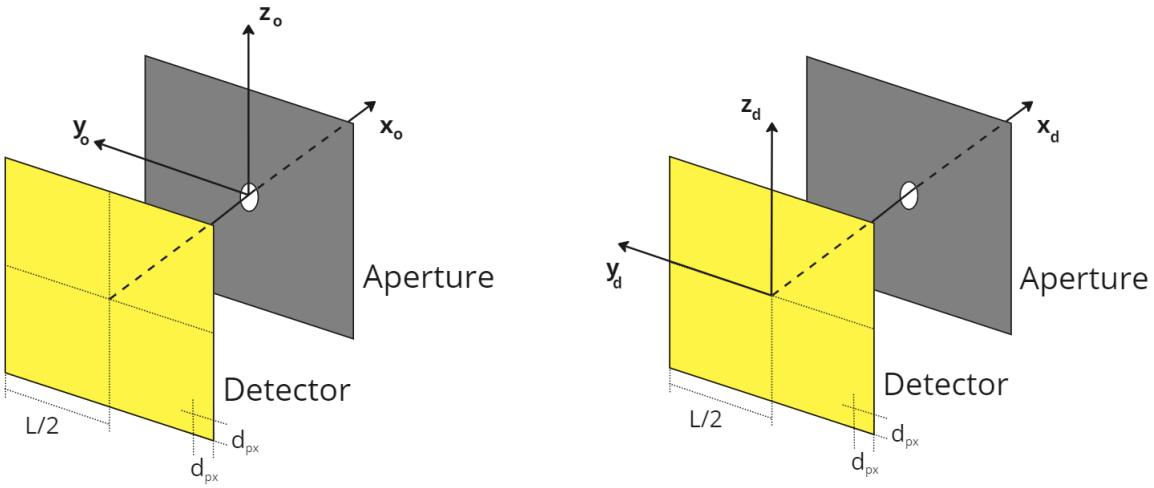

(a) Camera axis. (b) Detector axis.

Figure 5.2: Reference frames for image acquisition.

To obtain the ejecta dust image, it is necessary to have the position of the particles, propagated with the dynamic model implemented in Chapter 3, in the new camera reference frame. Thanks to them, it is possible to evaluate the visibility, as shown in Figure 5.3, respecting these three conditions:

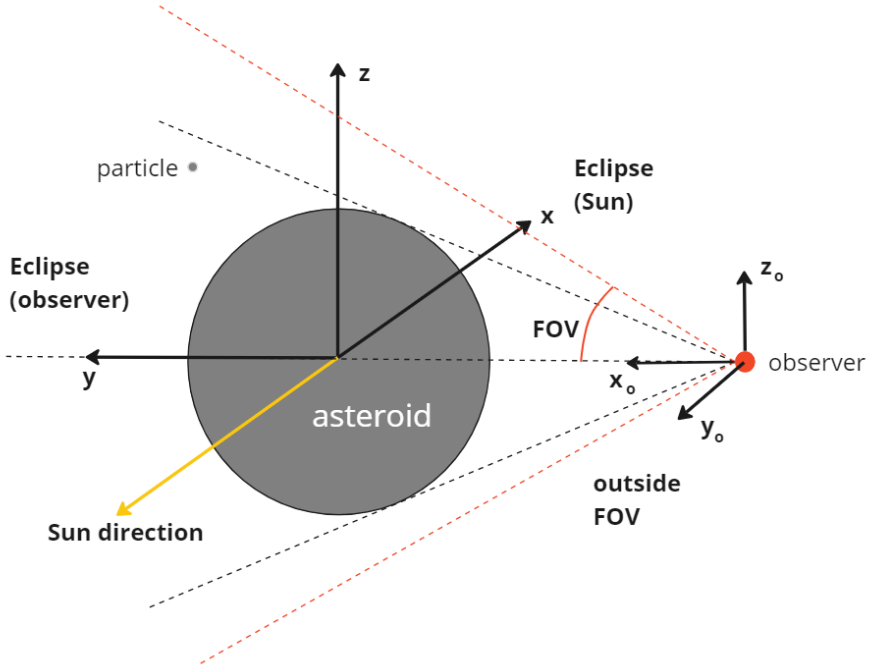

Figure 5.3: Visibility conditions.

1. the particle must be within the camera's field of view (FOV);
2. the particle must not be in eclipse with respect to the Sun;
3. the particle must not be in eclipse with respect to the camera.

To get the simulated asteroid image, the asteroid is displayed as a spherical shape to lighten the computational cost of the model. Obtaining the observer - dust particle distance as the difference of their positions $\boldsymbol{v} = \boldsymbol{P_p} - \boldsymbol{P_0}$, where $\boldsymbol{P_0}$ is the position of the observer, and $\boldsymbol{P_p}$ is the particle position, the particle image on the y-z detector plane can be obtained as follows:

$$\begin{aligned} y_{dp} &= (u - P_{0,x})\frac{v_y}{v_x} + P_{0,y} \\ z_{dp} &= (y_{dp} - P_{0,y})\frac{v_z}{v_y} + P_{0,z} \end{aligned} \tag{5.2}$$

To meet the first visibility condition, the detector plane particle position must fall on the detector plane itself, therefore:

$$\begin{cases} y_{dp} \leq \dfrac{L}{2} \\ z_{dp} \leq \dfrac{L}{2} \end{cases} \tag{5.3}$$

The second condition can be evaluated by referring to the synodic reference frame. The particle will be in eclipse with respect the Sun if:

$$\begin{cases} r_{ap,x} > 0 \\ r_{ap,y}^2 + r_{ap,z}^2 < R^2 \end{cases} \tag{5.4}$$

where the R is the asteroid mean radius showed in Table 2.1. In the model, the distance from the Sun to the asteroid is approximated to infinity, forming a shadow cylinder behind the asteroid's surface. This approximation cannot be made with the spacecraft, which could also be located a few tens of meters from the asteroid. To comply with the third and final visibility condition, the particle will be in eclipse with respect to the observer if:

$$\begin{cases} r_{po,x} > R_v \\ r_{po,y}^2 + r_{po,z}^2 < R_{new}^2 \end{cases} \tag{5.5}$$

Where R_{new} is the virtual radius representing the disc obscured by the asteroid at distance

$r_{po,x}$, and R_v is the distance between the observer and the visibility limit of the asteroid, as shown in Figure 5.4, calculated as:

$$\begin{aligned} R_v &= r_{sp}\cos(\xi)^2 \\ R_{new} &= r_{po,x}\tan(\xi) \end{aligned} \tag{5.6}$$

Where ξ is obtaind as:

$$\xi = \arcsin\left(\frac{R_{ast}}{||\boldsymbol{r_{sp}}||}\right) \tag{5.7}$$

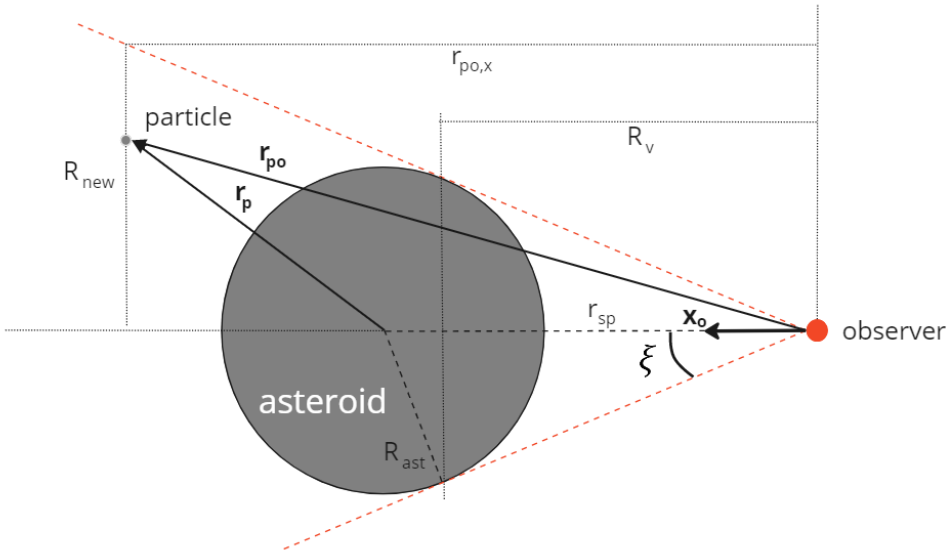

Figure 5.4: Spacecraft eclipse condition.

5.1.1. Phase angle and magnitude

To obtain the solar radiation reflected towards the observer by the particles, the phase angle and scattering computations are necessary. The phase angle ϕ is the angle between the Sun-particle and particle-observer distances, which therefore varies from 0 to 180 degrees. However, to obtain useful images, in this research, the pointing of the camera ensures the Sun out from the field of view. Consequently, the 180-degree phase angle will never be reached.

Two different models for the solar flux radiated by the particles and the subsequent calculation of the apparent magnitude have been implemented. The first one, developed

by Hergenrother et al. [7] for the study of the ejecta dust of the asteroid (101955) Bennu, has been applied to obtain Dart impact simulated images, as seen in Fahnestock et al. [5]. The apparent magnitude is evaluated as follows:

$$m_p = H + \frac{\partial V_m}{\partial \phi}\phi + 5\log_{10}(r_{sp}r_{ap}) \tag{5.8}$$

Where the absolute magnitude H is computed as:

$$H = 5\log_{10}\left(\frac{P_0}{d\sqrt{p}}\right) \tag{5.9}$$

Where P_0 is the solar flux at 1 AU, and p is the particle albedo, equal to the Ryugu surface in Table 2.1. The phase slope $\partial V_m/\partial\phi = 0.013$ mag/deg from Hergenrother et al. [7], which describes the variation of the apparent magnitude depending on phase angle. In case of multiple particles for each sample, the mean size of the sample is computed as [5]:

$$d = 2^{\frac{1}{3}}\left(\frac{1}{d_u^3} + \frac{1}{d_l^3}\right)^{-\frac{1}{3}} \tag{5.10}$$

Where d_u and d_l are the maximum and minimum extremes of the particle size range. This model is valid only for a phase angle value between 70 and 120 degrees. In the case study, the spacecraft could be positioned at any position with respect to the ejecta dust. Consequently, a second model is considered: the Lambertian (diffusely-reflecting) sphere model is used to compute the reflected solar radiation with the expression derived by Vallerie [39]:

$$F_{\text{diff}} = \frac{2}{3}p\frac{(d/2)^2}{\pi r_{ap}^2}(\sin(\phi) + (\pi - \phi)\cos(\phi))P_0 \tag{5.11}$$

and then the apparent magnitude is calculated:

$$m_p = -26.74 - 2.5\log_{10}(F_{\text{diff}/\text{P}_0}) \tag{5.12}$$

In Figure 5.5 the two models are compared for the same particle at the same distance from the observer. It can be observed with the Lambertian model how the magnitude increases steeply near the maximum phase angle, which is more realistic than the Hergenrother model, even if the latter has greater validity in its range of competence.

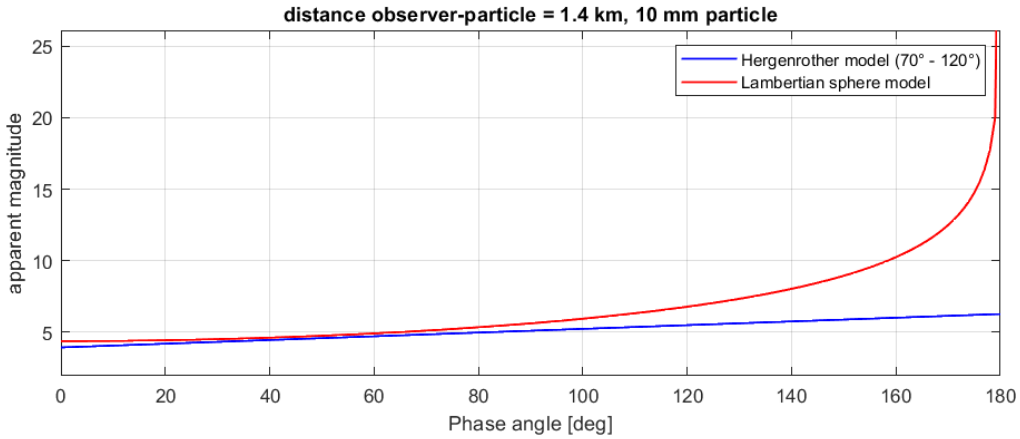

Figure 5.5: Magnitude value for each phase angle for 1.4 km distant 10 mm particle.

A possible third model is obtained by combining the two models and creating a continuous function, as shown in Figure 5.6, in which the Hergenrother model is assumed only in its range of validity. In order to avoid value jumps, the differences in magnitude (or flux) are calculated at a phase angle of 70 and 120 degrees, and then they are subtracted from the value of the Lambertian model.

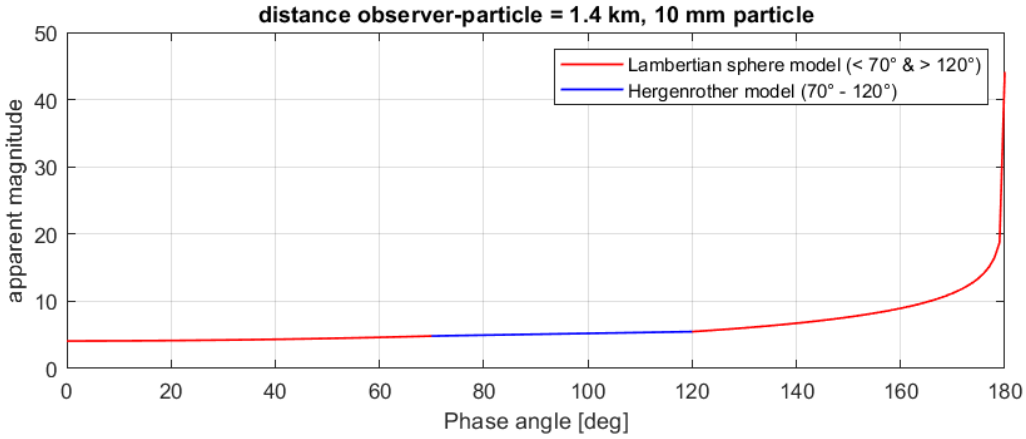

Figure 5.6: New model of magnitude value for each phase angle for 1.4km distant 10mm particle.

In the Chapter 7, both models will be used to observe the differences in magnitude and the third model for the observation of the displacement and accretion of the ejecta cone.

5.1.2. Image acquisition and Point Spread Function (PSF)

Once evaluated detector plane position of a given particle (and therefore the pixel), the acquisition of the image is obtained by flux computation on each pixel. After that, the

value is converted into magnitude as in the Eq. 5.12. Taking as reference the camera tested in a space environment and used for the same purpose, the DCAM3-D camera of Hayabusa2 [13], whose specifications are shown in Table 5.1, the saturation value of the pixel is calculated (from 1 to 255, for the 8-bit ADC converter). In this model, the minimum value has been set to the maximum magnitude visible from an optical instrument, equal to 34, while the maximum value (255) is set simply as the maximum value obtained from the image itself.

The image exposure time has been studied for the specific camera chosen in Ishibashi et al. [13], where two image acquisition modes are defined which have respectively 0.5 and 2.5 ms of exposure time. Furthermore, the level of the dark current noise is evaluated (the readout noise is not dependent on the exposure time). The results show how readout noise is dominant at the chosen exposure times. But, due to their low relevance to the useful signal, noises are not modeled in this study.

DCAM3-D camera	
Detector type	CMOS
Number of pixels	2210 x 3002
Used number of pixels n_{px}	2000 x 2000
Pixel size d_{px}	3.5 µm x 3.5 µm
ADC bits	10 bits
Significant ADC bits	8 bits
FOV θ_{FOV}	37 deg
Focal length f	5.76 mm
Pixel scale	0.65 ± 0.05 mrad/px

Table 5.1: DCAM3-D camera parameters.

One disturbance that needs to be considered is the diffraction of light through the optical aperture: the smaller the aperture, the more pronounced the effect. The studies conducted on the DCAM3-D reference camera and also on the ONC-T camera [15] (on board Hayabusa2, with a much narrower angle of view for images at a great distance) help to understand the entity of the phenomenon.

In Figure 5.7 the same light source is represented with different diffraction parameters, in particular, a gaussian distribution of the irradiation that hits the single pixels is implemented. With the change of the standard deviation σ, the irradiation is more or less

distributed on the adjacent pixels, and its value depends on the technical characteristics of the camera, especially on the diameter of the aperture (and the wavelength). The model used differs from the real system developed for the DCAM3-D camera, but an indicative value taken from the study of the real images and calibration can be used.

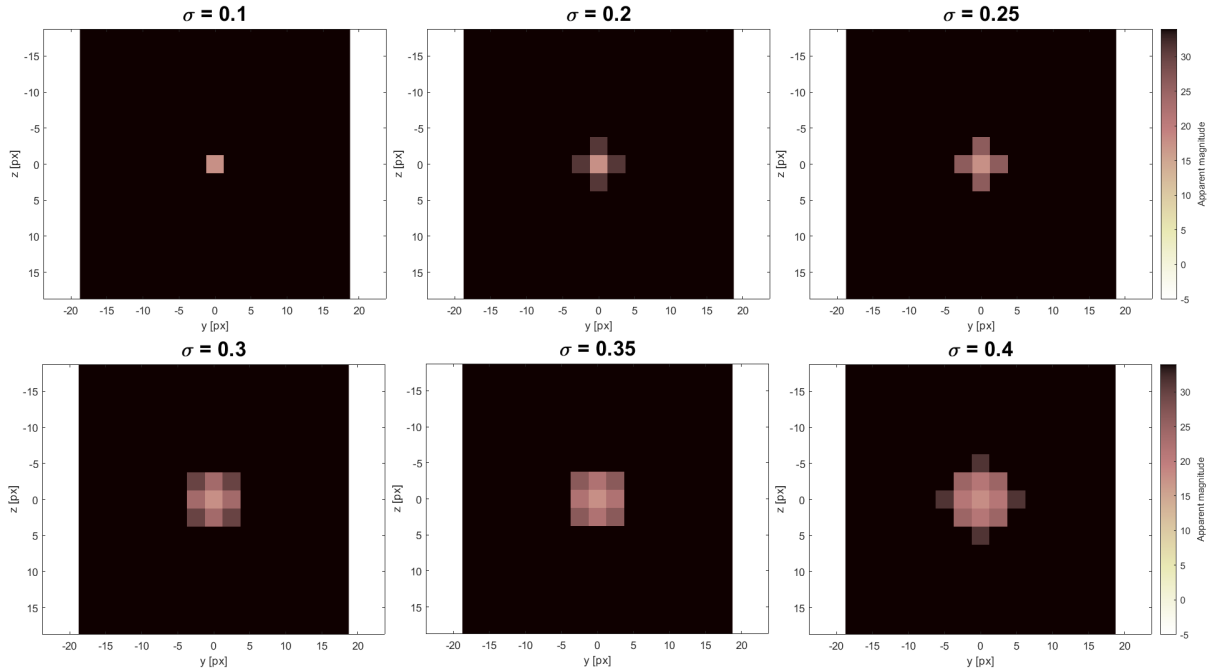

Figure 5.7: Application of PSF with different standard deviation values.

For the images of the light source, a dust particle placed 1 km away from the observer with a phase angle of 90 degrees was used, in the absence of noise. From the camera images used by the Hayabusa2 probe, a value of σ equal to 0.2 is selected.

The asteroid visualization is modeled as a spherical body with a homogeneous constant reflection of sunlight which depends exclusively on the albedo. This simple approximation of the asteroid visualization is intended to lighten the computational load, without heavy impacts on the study, due to the interest only for the ejecta dust visualization. Figure 5.8 shows a simulated image of the asteroid obtained from a certain position around it. The asteroid radius considered for visualization, as for evaluating the impact of dust on the ground, is the average radius in Table 2.1.

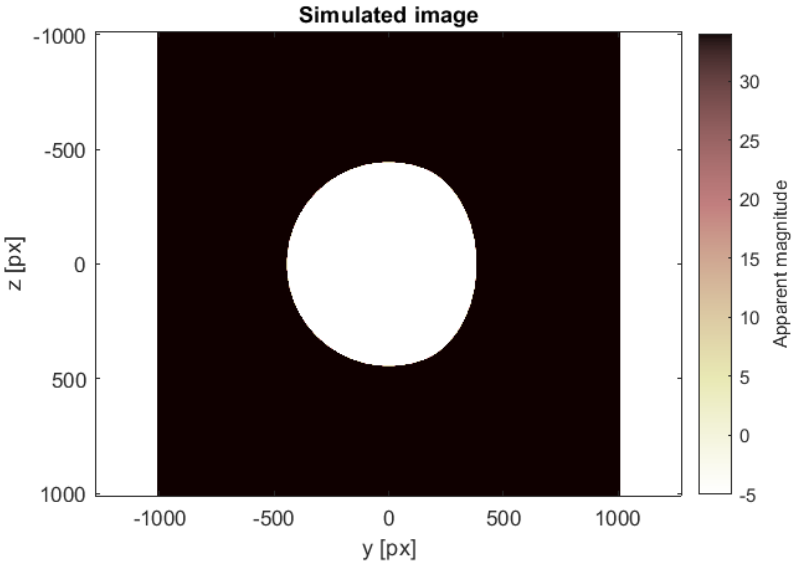

Figure 5.8: Asteroid view form camera at [-1,-1,0] km asteroid centre synodic reference frame, nadir pointing.

Only the sunlit part of the asteroid is displayed in the image. For displaying the dust - surface overlapping, particles take precedence, which obscure the pixel from surface radiation. Subsequently, the PSF redistributes the surface light in that pixel, except for a thick dust cover. An example can be seen in Figure 5.9, with a random impact on the sunlit surface of the asteroid. The image is simulated 20 minutes after the impact at 45 degrees latitude, on the sunlit side of the asteroid.

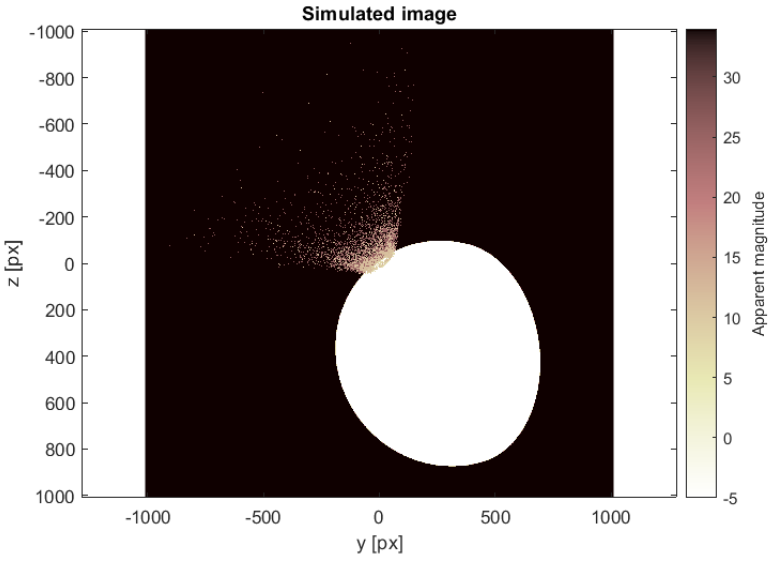

Figure 5.9: Impact view form camera at [-1,-1,0] km asteroid centre synodic reference frame, impact pointing.

5.2. Spacecraft position

Also the spacecraft position evaluation during the impact is of great relevance for image acquisition and also for safety, considering that the probe could be affected by ejecta dust. First, the space around the asteroid must be defined, which reflects the synodic reference frame seen in Chapter 3, but with the asteroid as the origin of the axes. As can be seen in Figure 5.10, the mean meridian has longitude 0° in the night side, and 180° in the side exposed to sunlight.

Once a observation location in space has been selected, the resolution of the image can be calculated (in metres per pixel):

$$H_{px} = ||\boldsymbol{r}|| \tan(IFOV) \tag{5.13}$$

Where $\boldsymbol{r}$ is the generic target distance vector from observer, and IFOV is the instant field of view.

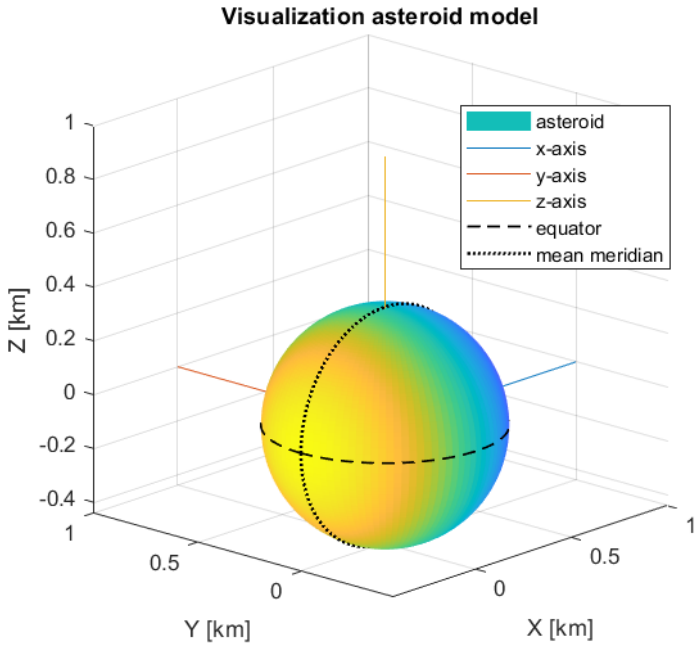

Figure 5.10: asteroid visualization, steroid centered synodic reference frame. 0 degree longitude on night side

Location selection is crucial for obtaining useful images for ejecta particles study. As shown in Figure 5.11, it is necessary to evaluate whether the impact site is visible to the observer and how likely ejecta dust impact may occur. In work of Trisolini [37], the

possibility of ejecta dust impact is studied as an opportunity to collect it directly in orbit, and the number of particles that can be collected is sensitive to the chosen location of the spacecraft, with respect to the impact site. In this study, several positions are studied for the ejecta cone observation, always keeping in mind the safety of the spacecraft.

Concerning the Hayabusa2 mission, the spacecraft was positioned just over the horizon to shelter from the fragments of the impactor explosion [42] (which accelerated the projectile up to 2 km/s). The images taken in the following instants instead guaranteed the view of the impact place, as shown in Figure 2.4.

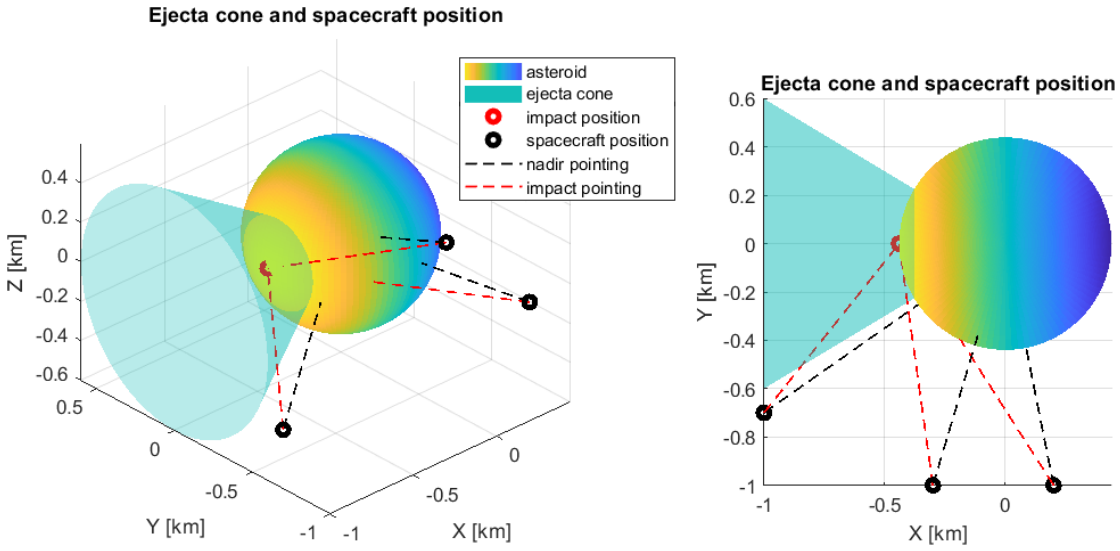

Figure 5.11: asteroid visualization, steroid centered synodic reference frame. Ejecta cone and spacecraft positions

A preliminary position analysis can be carried out with Figure 5.11, where three possible locations are shown, two of which have a direct view of the impact point, but one of the two is too close to the ejecta cone axis, exposing the spacecraft to the impact of high-speed particles. Therefore an initial trade-off leads the spacecraft where the impact point is visible on the asteroid horizon. The strategy implemented in the Hayabusa2 mission is a deployable camera (DCAM) [29] from the main probe. which remains in place in order to observe the impact. Separation occurred after bullet release and before impact. A separable camera made it possible to place the spacecraft beyond the horizon line with respect not only to the impact, but also to the fragments resulting from the explosion of the SCI.

Thus the model for the image acquisition is developed, and with the various observer locations, the images of the impact at the desired instant of time are simulated and studied in Chapter 7.

6 | Nanolander for images comparison

The use of a lander on the asteroid's surface at the impact moment has been previously explored as part of the AIDA program, with the MASCOT2 nanolander intended for deployment during the Dart impact on the Dimorphos asteroid [19]. Unfortunately, the nanolander was ultimately not utilized, there is the possibility for its implementation in future missions such as Hera. The novelty of this research lies in the images that could be captured by a lander during the impact, which could be used to supplement seismic studies if a seismograph was included on board.

In the Hayabusa2 mission, the MASCOT nanolander was successfully deployed on the surface of asteroid Ryugu with the aim of conducting on-site surface studies [20]. MASCOT and MASCOT2 nanolanders are used as references for this study, however, it's important to note that only the first has been tested in a scientific space mission.

Indeed, the study of seismic waves generated by the impact could provide valuable information about the interior structure of the asteroid, such as its density distribution and the presence of internal voids. This information could be used to refine our understanding of asteroid formation and evolution processes. However, it should be noted that the implementation of a seismograph or accelerometer on a nanolander (as the DACC designed for MASCOT2) would likely require additional engineering and design considerations, such as the need for a stable and level platform for the instrument, as well as measures to mitigate the effects of vibration and mechanical disturbances caused by the impact event. Overall, the integration of seismic and geophysical measurements with image acquisition could provide a more comprehensive and multi-disciplinary approach to the study of asteroid impact events and their effects on the asteroid's structure and evolution. Morphological modification processes have been studied with seismic and geomorphological models as in the work of Richardson et al. [26], investigating the distribution of the regolith and the density of craters on the asteroid's surface. This aspect will not be explored in this study, focusing more on image acquisition.

6.1. Tested features and implementations

During the Hayabusa2 mission, the nanolander free-fell from a height of 100 meters after uncoupling from the main probe [19]. It stopped after a few bounces on the surface, with the main constraint being an impact velocity less than half the asteroid escape velocity to avoid an overly energetic rebound that would cause the lander to run away. The scientific instrumentation on board the nanolander included a hyper-spectral infrared microscope MicrOmega (MMEGA), a thermal IR radiometer (MARA), a camera, and a magnetometer [20]. It also had a battery, a mobility mechanism for reorientation and movement on the surface, and an antenna to communicate with the main probe. During the fall on the surface, which lasted between 20 and 30 minutes (taking into account the rebounds), the magnetometer was primarily used, while the other instruments were used on the surface to study it with a resolution in the order of millimeters.

As shown in Figure 6.1, the new task to be performed compared to the reference nanolander is the observation of the ejecta cone. For this purpose, a study on the camera already implemented and on wide-angle cameras was carried out, to take advantage of the advantageous observation position.

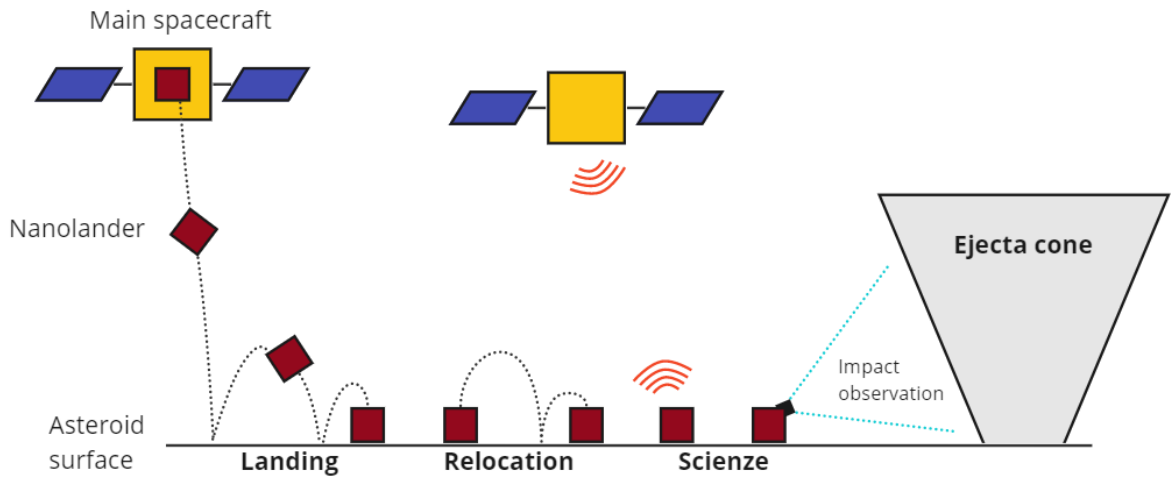

Figure 6.1: Nanolander operations on asteroid surface

The MASCOT lander had an autonomous operations scheduling system managed by the autonomy manager (MAM) software. This was necessary due to the lander's short lifetime,which therefore led to the choice of automating the various tasks to be performed. The implementation of solar panels allowed for a longer operational lifetime, which is essential for accurate positioning on the asteroid's surface relative to the impact point.

For example, the MASCOT2 lander was estimated to have a lifetime of over three months, compared to its predecessor MASCOT, which had only 16 hours of operational time. However, to avoid damage from ejecta dust, the solar panels will need to be closed for a certain amount of time, which will be discussed in Section 6.2.

6.1.1. Nanolander mission constraints and requirements

This section contains a list of constraints and requirements, in order to get a more complete picture of lander mission aspects. The MASCOT nanolander from the Hayabusa2 mission is the primary reference, already tested in a successful space mission. As for the solar panels, a preliminary configuration study comes from MASCOT2. In Table 6.1 there are the most important requirements and sizing of the MASCOT lander, which are also useful in the development of the new lander for the study purpose.

MASCOT principal requirements & constraints	
Mass constraint	11 kg
Size constraint	0.3 x 0.3 x 0.2 m
Altitude release	100 m
Relative separation velocity	5 cm/s
Landing velocity	$<$ 0.5 Ryugu escape velocity
Landing time	20-30 minutes (fall + rebounds)
Lander temperature range	[-60°C , +77°C]
Surface average temperature range	[-50°C , +25°C]
MASCAM operational temperature	$<$ 30°C
Operational life	2 asteroid rotations
Link time with main probe	40% asteroid rotational period

Table 6.1: MASCOT lander requirements for the Hayabusa2 mission on the asteroid Ryugu [20].

When the lander is on the surface at the same time as the impact, new requirements are added regarding positioning (study in section 6.2), orientation and visibility. Furthermore, taking MASCOT2 as a reference, with the addition of solar panels, the operational life of the lander is extended. The new requirements are as follows:

- The lander's solar arrays and secondary battery are expected to provide an operational lifetime of more than 3 months.

- The extension of the solar panels shall take place for each stationing on the surface and be retracted for a programmed displacement or for the imminent approach of the dust particles generated by the impact (to avoid damage to the panels and the withdrawal mechanism).
- The lander shall be positioned at a sufficient distance to guarantee its safety, both due to the uncertainty of the impact location and due to the fallout of the dust. Furthermore, the location shall take into account the phase angle at the moment of impact, to avoid the sun in the view of the camera.
- The lander shall have implemented a seismograph capable of detecting the seismic waves due to the impact for the study of the interior of the asteroid.

As always happens in space mission analysis, the implementation of new tools requires a multi-iteration study for sizing and for the cost-benefit ratio evaluation. In this work, only the possibility of having a directional or fixed camera for the ejecta cone observation directly from the asteroid surface is studied.

6.2. Nanolander position on surface

For the safety and integrity of the lander, it is important to assess its position on the surface during impact, due to the inevitable collision with dust. It is important to ensure that the ejecta dust falling on the lander does not cause any damage to its structure, as its speed is below the asteroid's escape speed (approximately 38 cm/s), although some particles may have higher speeds in reality. Another important factor to consider is the uncertainty of the impact location. According to the SCI simulations of the Hayabusa2 mission, the uncertainty of the projectile (launched from an altitude of 500 meters above the surface) was 200 meters in radius [20].

In the Deep Impact mission [25],the observations established that most of the ejecta dust blanket covered up to 4 crater radii away from the impact location, and after about 45 minutes, particles were deposited up to 20 crater radii away. In the Hayabusa2 mission, from the images [1], it was observed that the dust reached almost 3 crater radii 500 seconds after the impact. The distances, as compared to the actual asteroid, are shown qualitatively in Figure 6.2. The asteroid's non-spherical shape creates flat surfaces, making it possible to observe the impact point even at great distances, which would be impossible with a completely spherical surface.

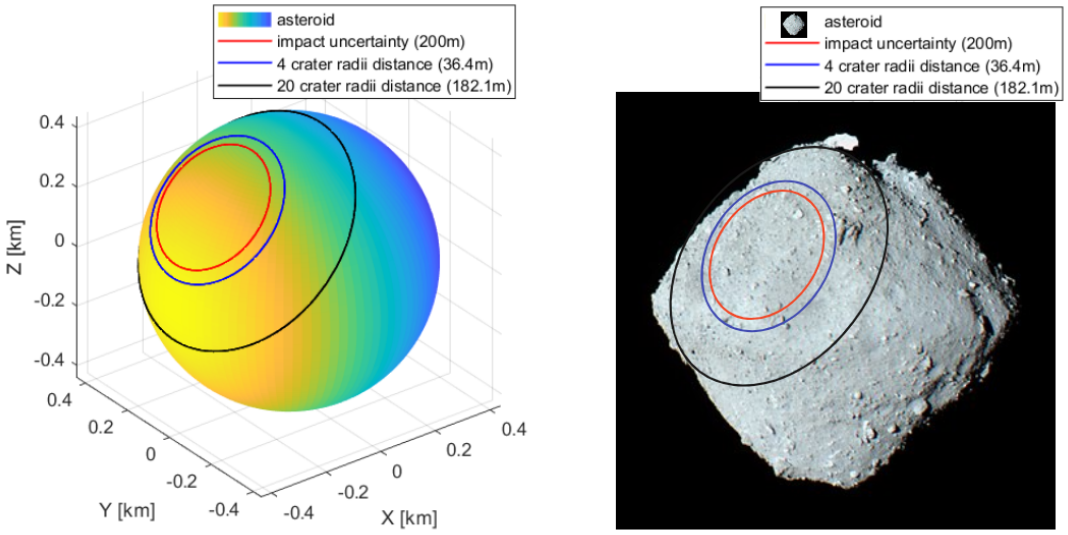

Figure 6.2: Crater size on surface and qualitative representation on the real asteroid.

With the model developed in Section 4.2, it is possible to evaluate the time and distance of dust landing, the minimum safety distance for observing the impact, and the percentage of landed particles.

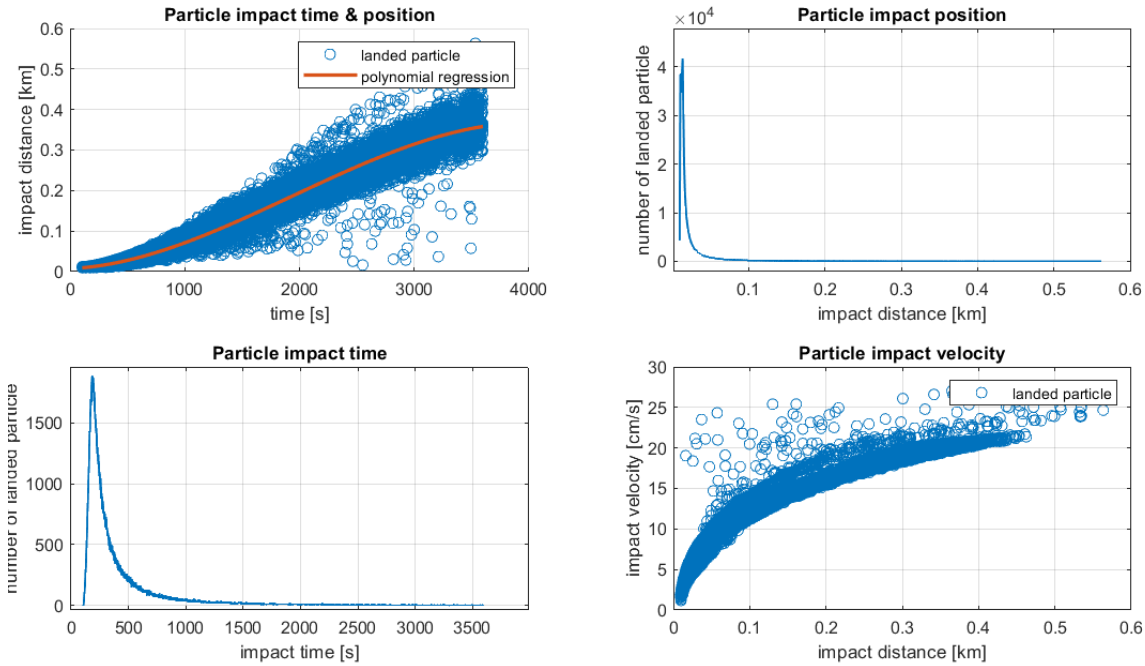

Figure 6.3: Ejecta particles landed compared to impact distance, time and velocity.

With a simulation of 350,000 dust particles with dimensions ranging linearly from 0.1 mm to 10 mm, the number of particles that landed on the ground was calculated as a

function of the distance from the point of impact and time, as shown in Figure 6.3. The model results show that 75 % of the particles fall back after about 9 minutes, and 90 % travel less than 100 meters away from the impact. Both percentages are calculated with the total number of particles landed and still in orbit. In the graphs in which the individual samples of landed particles are visible as a function of time and speed, it is possible to observe some deviations from the average trend. This phenomenon is due to solar radiation pressure which pushes the finest particles more effectively in the x-positive direction (synodic reference frame). Once the optimal distance has been selected, from Figure 6.3 it is possible to estimate the time intervals in which the dust accumulation on the lander is possible. Due to the uncertainty of the impact location, the impactor-lander distance can vary between 182 meters and 382 meters. From these data, it appears that the lander may be hit by dust about 1400 seconds after impact. To avoid complications during the mission, the solar panels should be closed before impact, while the waiting time before reopening the panels depends on the degree of precaution and the duration of the battery, since the dust can fall even after many hours. A simulation over a longer time interval shows that 95% of the particles are on the ground 30 minutes after the impact. 97.5% after one hour, 98.5% after five hours.

Finally, the position of the landers is chosen 20 crater radii from the uncertainty zone. As evaluated in Figure 6.3, the images will be obtained for a maximum time of 45 minutes after the impact, to avoid damages due to the ejecta dust. If the impact does not occur at the designated point, a reduction of the image acquisition time may be necessary

6.2.1. Nanolader camera pointing

To properly evaluate the optimal view from the surface, it is important to consider other factors such as the orientation of the lander's camera relative to the impact location and the position of the Sun. With a hypothetical impact location at 45 degrees latitude and 180 degrees longitude (on the mean meridian), in Figure 6.4a, a possible observation location is shown, where the camera is pointed towards the impact location. However, the impact remains obscured by the horizon, assuming it occurs exactly at the selected point. Additionally, the camera looks towards the negative x-axis of the synodic reference frame, which also includes the Sun in the FoV. To simplify the lander's design or due to space and cost limitations, it may have been equipped with a camera that only points towards the zenith. However, this kind of pointing may not be useful for observing the impact's ejecta cone axis, as shown in Figure 6.4b. Even with a wide-angle camera, the initial dust could remain hidden. A panoramic camera or one that can rotate 360 degrees could be an ideal solution, but it may exceed the structural constraints of a nanolander.

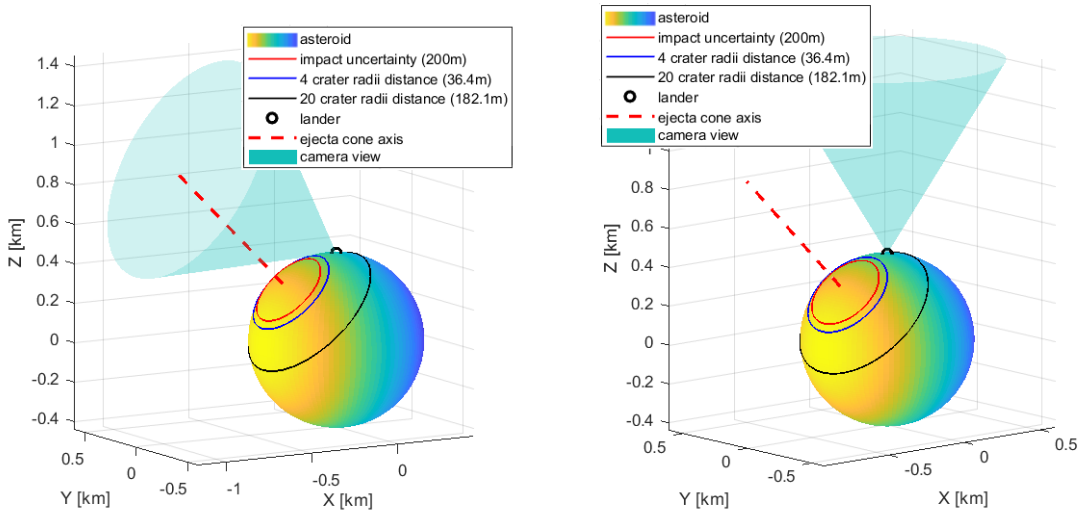

(a) Lander camera pointing towards the impact location at nord pole.

(b) Lander camera pointing towards zenit at nord pole.

Figure 6.4: Evaluation of lander location and pointing.

Therefore, the best location for an impact-observing lander is either east or west of the impact zone. If the impact occurred on the sunrise or sunset line, a location north or south of the impact would be more appropriate to avoid direct sunlight. For instance, if the lander is located 20 crater radii from the impact zone (in red in Figure 6.2), it could be placed on the opposite side of the impact's actual location from the impact zone viewpoint. Having multiple landers on the asteroid's surface at the same time would allow for a complete reconstruction of the dust cone from various angles, even if the impact occurred at the edge of the uncertainty zone. Figure 6.5 displays the placement of two nanolanders, positioned respectively 20 crater radii east and west of the impact location zone.

Figure 6.2 shows the actual surface of the asteroid, which allows the lander to be positioned far from the impact point and still have visibility, particularly if the impact occurs on one of the asteroid's flat surfaces. Consequently, the lander can be placed at a greater distance, enhancing its safety. However, in the image acquisition model, the asteroid's shape is spherical for computational simplicity. Therefore, the selection of the lander's position was also based on the observability of the ejecta dust with the implemented model.

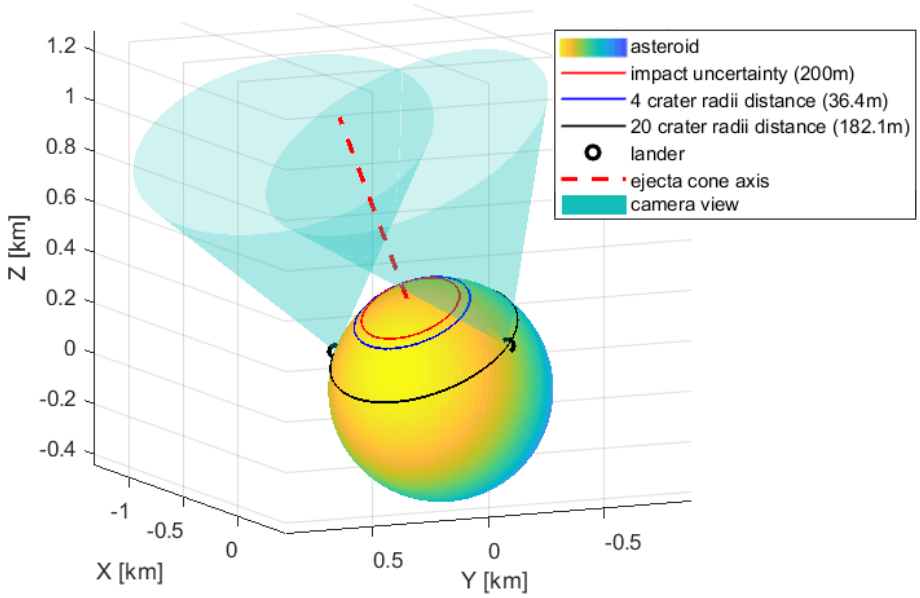

Figure 6.5: Double lander on asteroid surface and theirs views.

Furthermore. for the simulation of the images, the camera pointing will always be directed towards the impact zone, with an inclination such as to maintain the asteroid surface exactly below the FoV.

6.2.2. Nanolader camera selection

MASCAM was the on-board MASCOT camera, for on-site surface observation. Indeed, once the lander was correctly oriented, the camera pointed downwards, having the surface in most of its FoV. But from the images obtained during the descent on the surface, as seen in [6], it can be observed that the wide-ranging images are clear and well-defined. For this reason, the camera selected for the lander is the same one used on MASCOT. This preliminary choice avoids complications regarding the requirements and constraints to be considered for a new camera, since the newly chosen one has already been successfully tested in space mission on the asteroid Ryugu. The MASCAM parameters are shown in the Table 6.2.

MASCAM camera	
Detector type	CMOS
Number of pixels	1024 x 1024
Pixel size d_{px}	15 µm x 15 µm
ADC bits	14 bits
Significant ADC bits	10 bits
FOV θ_{FOV}	36.25 deg
Focal length f	14.8 mm
Pixel scale	150 micron/px at 150 mm

Table 6.2: MASCAM camera parameters [14].

As mentioned earlier, the implementation of a wide-angle camera can be useful for observing a surface impact. Consequently, the use of a camera with the same parameters as MASCAM but with a field of view of 60 degrees is studied, to assess the possible contribution of such payload in characterizing the ejecta plume.

For the diffraction inside the lander camera, the same Gaussian model used for the spacecraft camera has been implemented, but with a standard deviation index σ equal to 0.3, since MASCAM has a diffraction value $<$ 30 µm [14].

7 | Imaging and post-processing results

The simulated images presented and studied in this chapter are used to develop a model for asteroid impact observability, attempting to understand the effects of reflected sunlight and the properties of detectable dust. With a spacecraft in orbit around the asteroid and a lander on its surface, a small impact produced by a projectile fired by the spacecraft itself will undoubtedly be discussed, since it is dangerous to plan a large impact with nearby probes, as seen in Section 4.1.1. At a velocity of 2 kilometers per second, the object is capable of ejecting enough material from the surface to make the impact visible from a probe located several kilometers or hundreds of meters away.

Figure 7.1 shows the appearance of the simulated images that the model creates. In this case, the impact is at 45 degrees latitude on the illuminated side of the asteroid, 25 minutes after impact. The asteroid has the shape of a sphere that evenly reflects sunlight from the entire illuminated surface, as described in Section 5.1.2, while the particles reflect part of the solar radiation, using the third model described in Section 5.1.1, which corresponds to the Hergenrother model as long as the phase angle value is between 70 and 120 degrees. For the other phase angle values, the Lambert sphere model is used, as shown in Figure 4.6. The particle size varies between 0.1 mm and 10 mm according to the slope function presented in section 5.6, and depending on the $\bar{\alpha}$ parameter chosen, the function strongly favors the smallest particles.

These images are generated by the choice of the impact zone, subsequently by the dynamic propagation of the particles, as described in Chapter 3, whose initial conditions are given by the Housen & Holsapple model (Chapter 4). After that, the image acquisition model is used, through rotation matrices, calculation of the visibility, and calculation of the pixel hit, then applying the diffraction effect (Chapter 5).

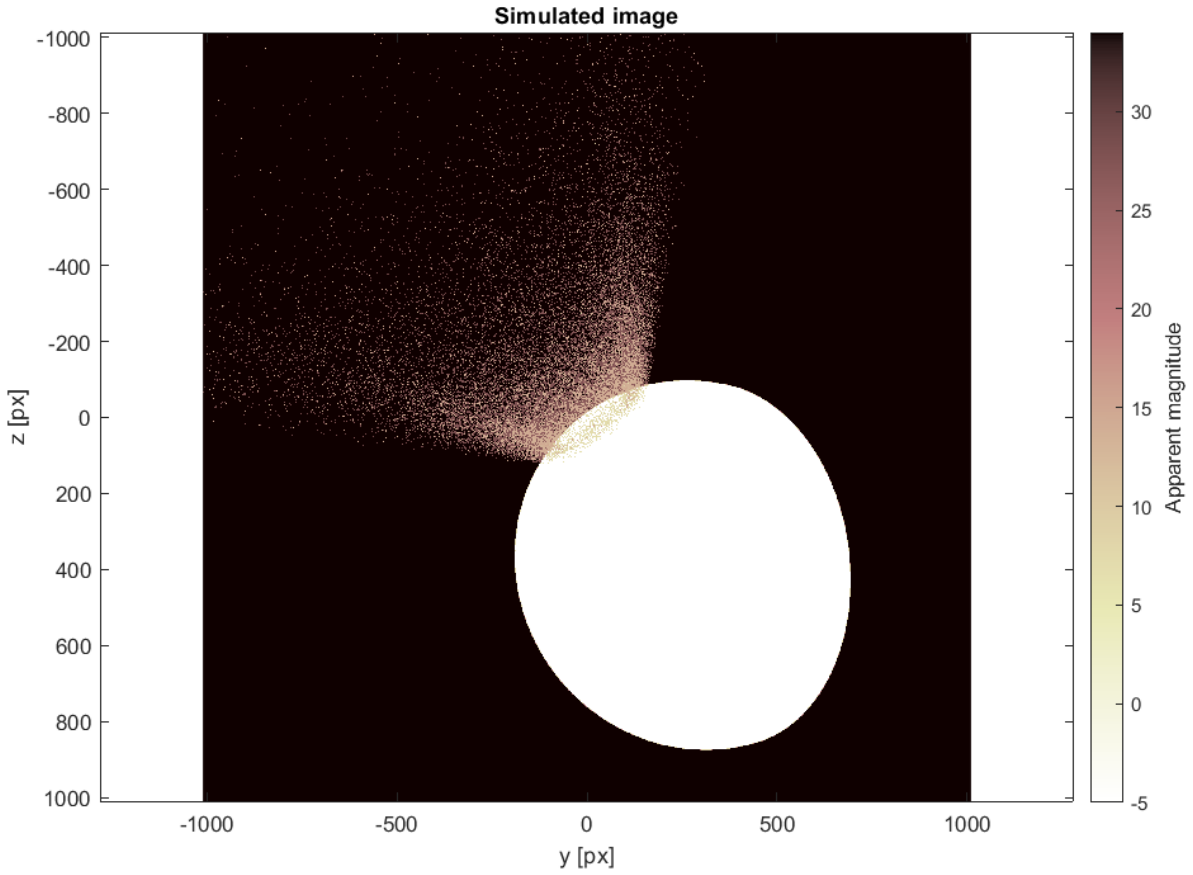

Figure 7.1: Image simulation of 1 million dust particles 25 minutes after the impact. Spacecraft position at [-1,-1,0]km. Impact location at 45° latitude, 180° longitude.

As seen in Section 6.2, most of the dust falls within the first few minutes after impact. In particular, for the impact shown in Figure 7.1, 75% of the dust is landed after only 9 minutes, 95% after 30 minutes. This is due to the low velocity of the ejecta particles launched from final stages of crater formation. Only 7.1% of the particles are displayed in the figure, and only the sunlit particles, in the FoV of the camera and not eclipsed behind the asteroid are shown. All that greatly lightens the computational load, especially for images simulated long after the impact.

Figure 7.2 shows the same impact at the same instant but from a different observer location, particularly behind the asteroid with respect to the Sun (not in eclipse). The position still guarantees the visualization of the ejecta cone, even if the point of impact and the first part of the ejecta cone are not visible. The magnitude of individual particles increases as the phase angle increases, making them dimmer, but still visible, as will be shown in later sections.

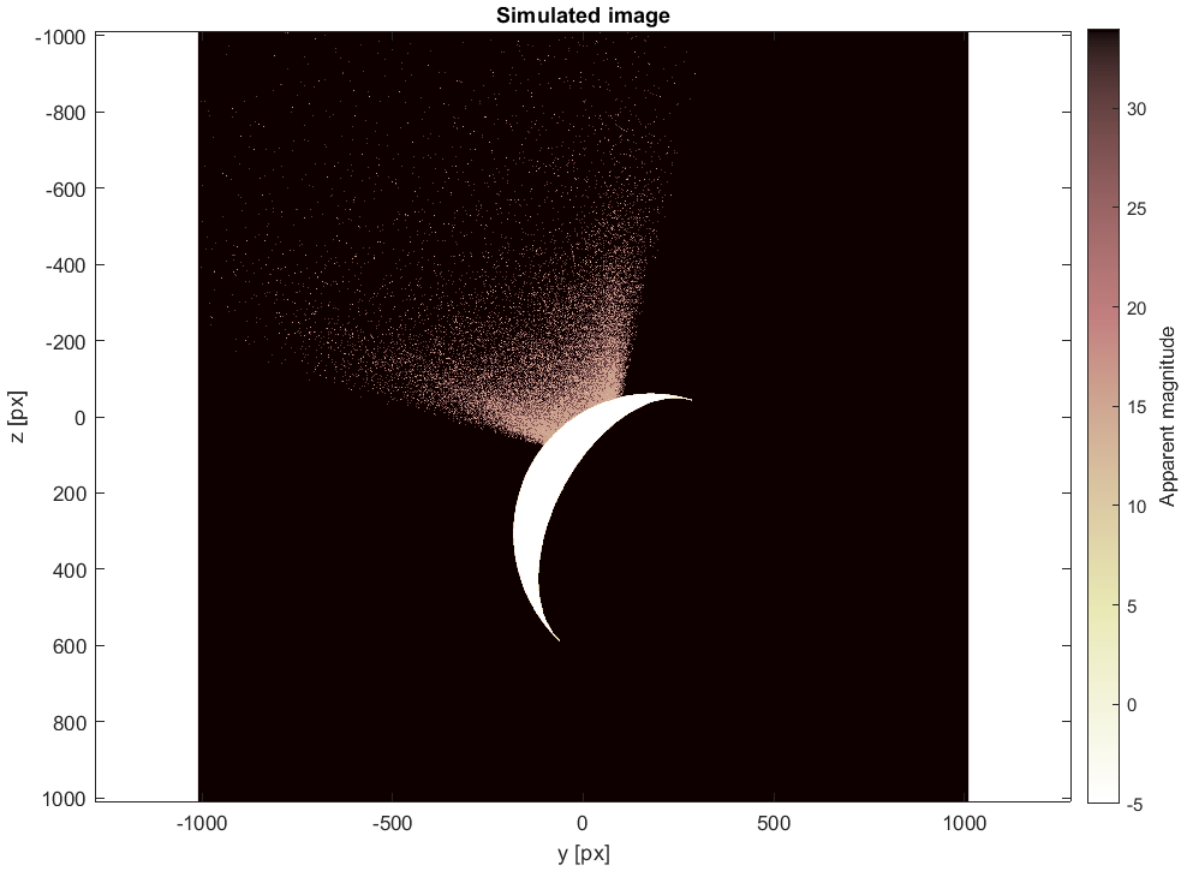

Figure 7.2: Image simulation of 1 million dust particles 25 minutes after the impact. Spacecraft position at [1,-1,1]km. Impact location at 45° latitude, 180° longitude.

All results were obtained using MATLAB software [12]. In particular, the integration is performed using the build-in MATLAB function ode113, while the images are a matrix representation of the magnitude for each detector pixel.

7.1. Comparison with real images for model verification

First of all, the comparison between the simulated images and the real images from the DCAM3 camera during the Hayabusa2 mission is performed. From Figure 7.3 to Figure 7.6 the comparisons between images in the instants of time 100, 192, 396, and 498 seconds after the impact are shown in sequence. The simulated images are obtained from the observer in position [-0.5 -0.5 0,3] km (synodic reference system centered on the asteroid), and a scale bar is inserted, as in the real images, to get an idea of the size of the ejecta cone. The scale bar is representative of the impact point, obtained by measuring the

resolution per pixel as in Eq. 5.13. The real pictures are taken from Arakawa et al. [1].

First of all, the sphericity of the asteroid is evident in the simulated images, due to the model developed in Section 5.1.2, while it is possible to notice how in the real image the asteroid has an irregular shape, almost flat in the impact zone, as already noted in Section 6.2. From the first image, 100 seconds after the impact, denser dust branches are visible, due to the presence of boulders on the surface that break the symmetry of the ejecta dust, as already observed in Section 2.3.1. As far as the dimensions of the cone are concerned, the images are superimposable in all time instants studied, even if the tips of the dust branches reach greater distances than those of the simulations, probably having a higher speed than the maximum speed used in the model, as seen in Section 4.2.

Another aspect is the brightness of the cone relative to the surface. As already mentioned, the model implements the same surface albedo for ejecta dust. Through the digital conversion of the signal, the minimum readable irradiance on a single pixel is set for a magnitude value equal to 34 that correspond at the first ADC digital number, while the last one is set for the highest brightness value directly registered from the image. This setting makes the display of the simulated minimum recorded magnitudes different from the real images, but does not compromise the data.

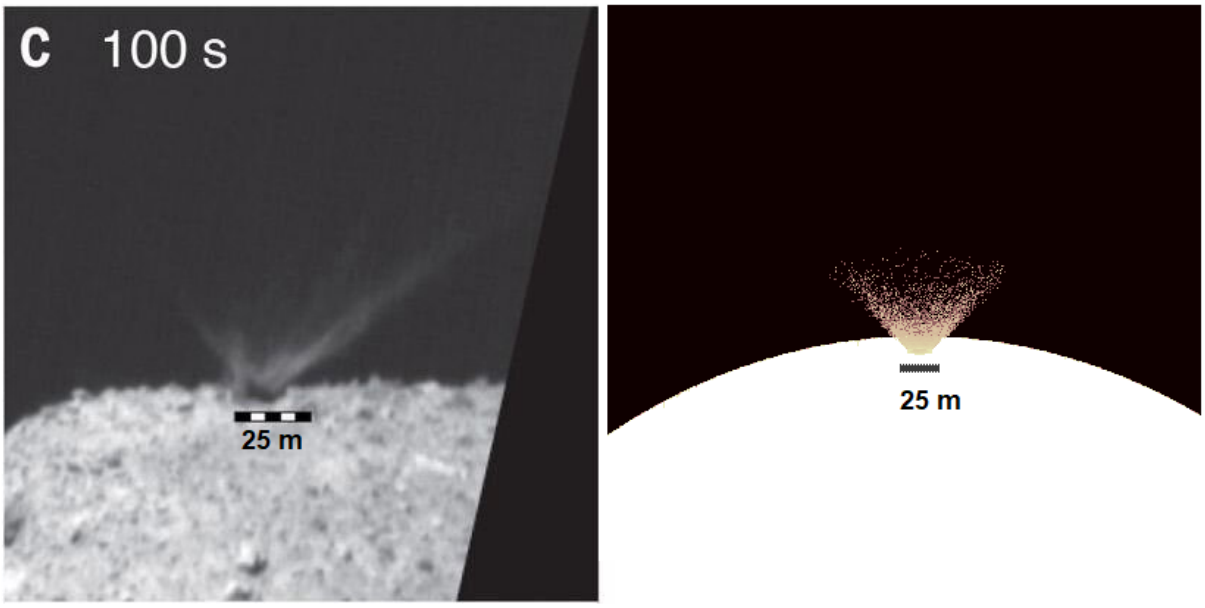

Figure 7.3: Simulated image (right figure) - real image (left figure) comparison at 100 seconds after impact. For both images, the same impact location and the same camera parameters are selected.

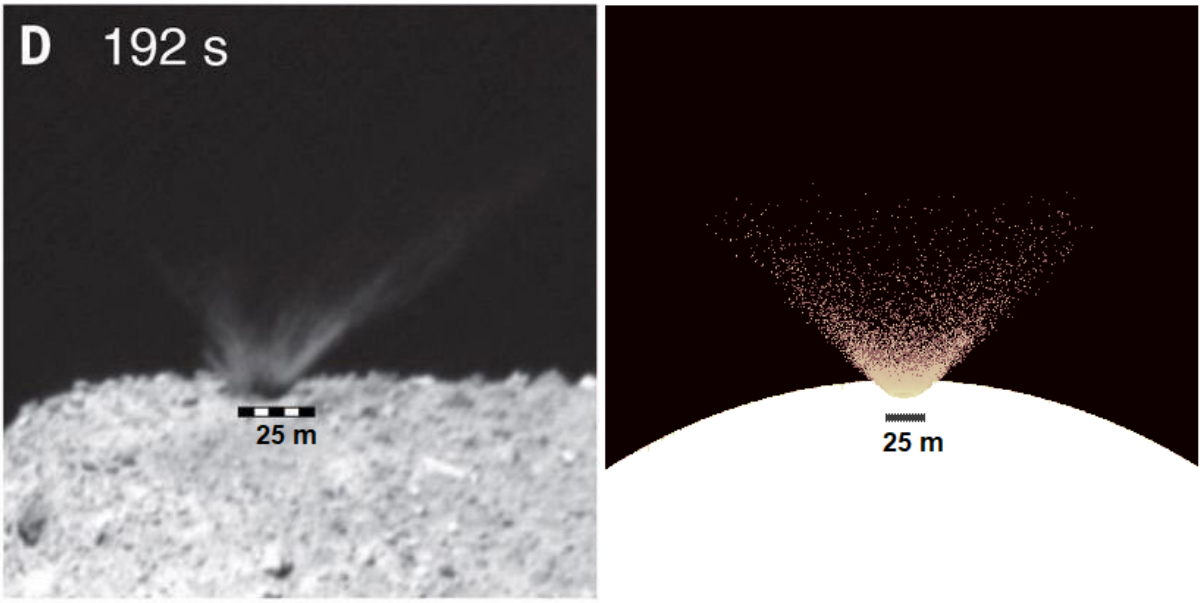

Figure 7.4: Simulated image (right figure) - real image (left figure) comparison at 192 seconds after impact. For both images, the same impact location and the same camera parameters are selected.

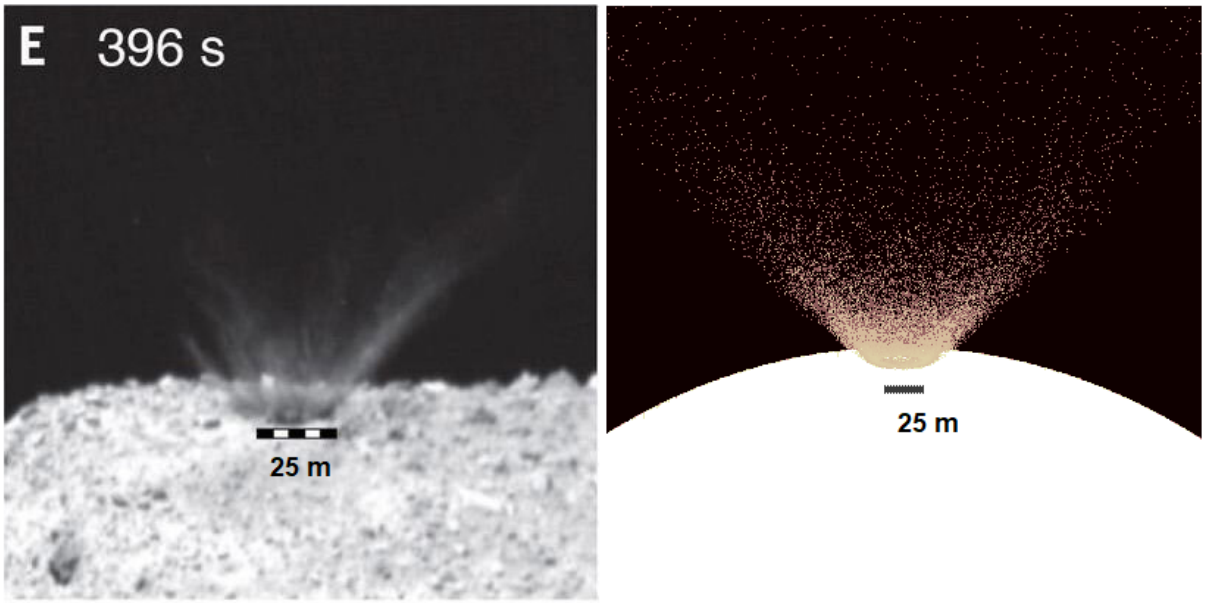

Figure 7.5: Simulated image (right figure) - real image (left figure) comparison at 396 seconds after impact. For both images, the same impact location and the same camera parameters are selected.

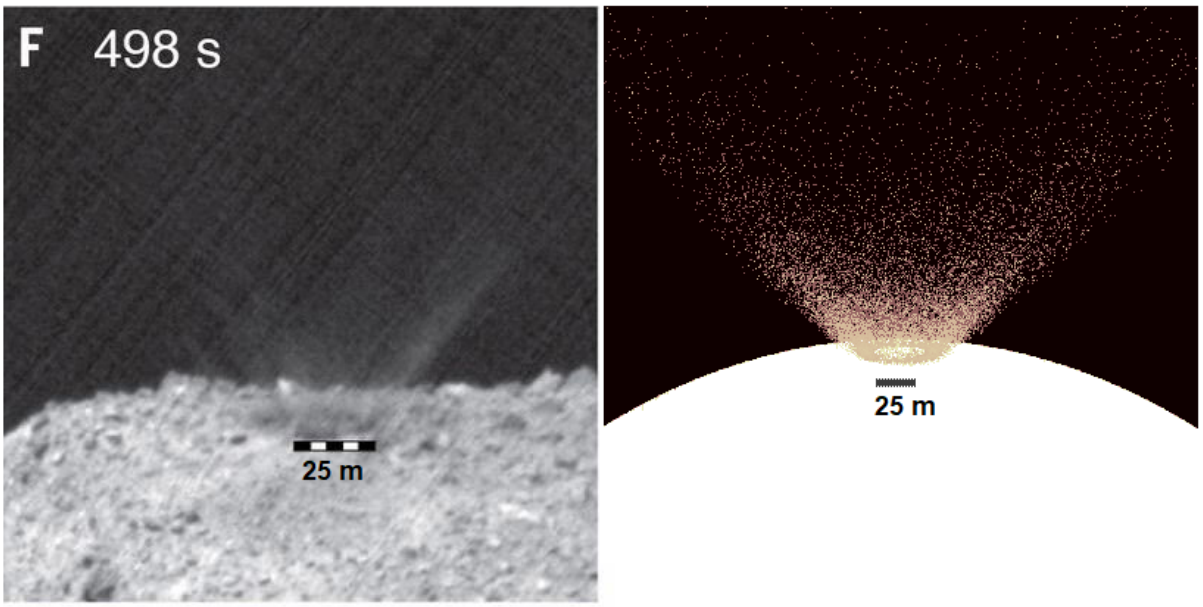

Figure 7.6: Simulated image (right figure) - real image (left figure) comparison at 498 seconds after impact. For both images, the same impact location and the same camera parameters are selected.

7.2. Ejecta cone shape with different particle sizes

The visualization of the ejecta cone shape and deformation by an observer orbiting the asteroid is studied in this section. As seen in Chapter 3, the finer particles are more subject to the solar radiation pressure, which changes their trajectory. Particles in the order of µm are swept away in an anti-solar direction up to within a few hours.

In the images from Figure 7.7 to Figure 7.9, two identical impacts with different particle sizes are simulated, on the three instants of time 10, 15, and 30 minutes after the impact, simulated from the observer location [0,-2,0] km in asteroid centered synodic reference frame. In the images on the right, particles of 0.1 mm size, in those on the left, particles of 1 mm size. The first difference between the two cases is the magnitude detected by the observer (for this type of image, the third model for radiation flux detection was used, section 5.1.1): the larger particles have a lower magnitude value detected.

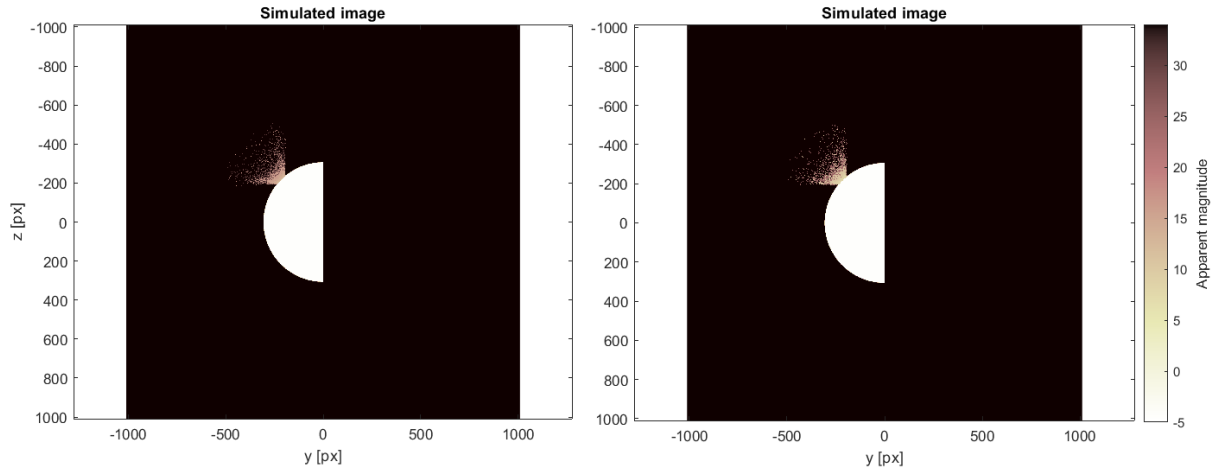

Figure 7.7: 45° latitude - 180° longitude impact, 10 minutes after the impact. [0,-2,0] km observer location. Left figure: particle size of 0.1 mm. Right figure: particle size of 1 mm.

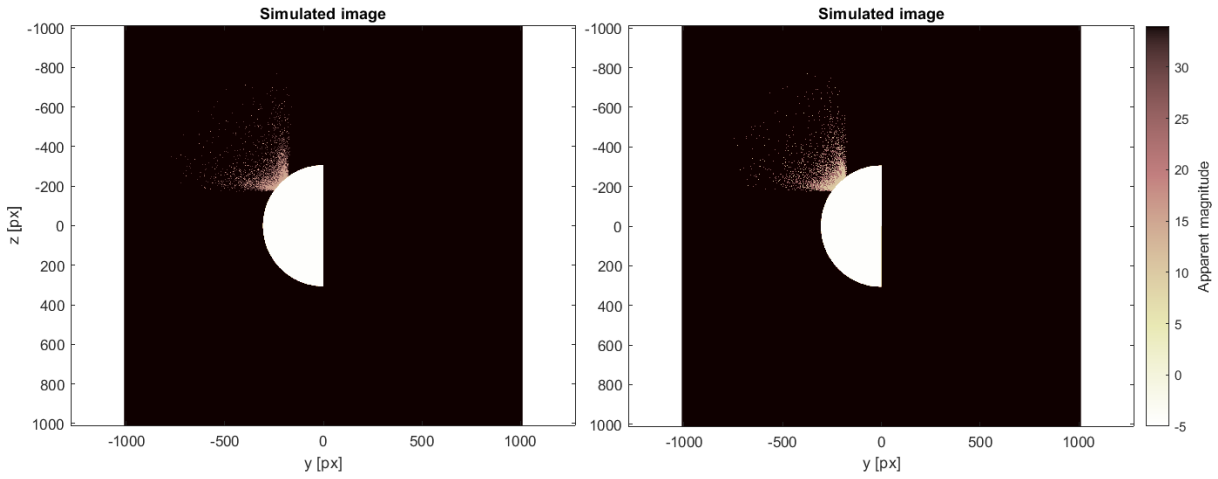

Figure 7.8: 45° latitude - 180° longitude impact, 15 minutes after the impact. [0,-2,0] km observer location. Left figure: particle size of 0.1 mm. Right figure: particle size of 1 mm.

The cone shape difference increases with time, since solar radiation has time to change the trajectory of finest particles. As can be observed in Figure 7.9, the right edge of the cone of the 0.1 mm particle size is much more displaced in the anti-solar direction than the particles of 1 mm size. The ability to discriminate the dimensions of the finest particles derives from the cone deformation observation, as well as from the calculation of the magnitude, which however can be compromised by the quantity of dust recorded in a single pixel. In Figure 7.10 there are some support lines that represent the edges of the ejecta cone.

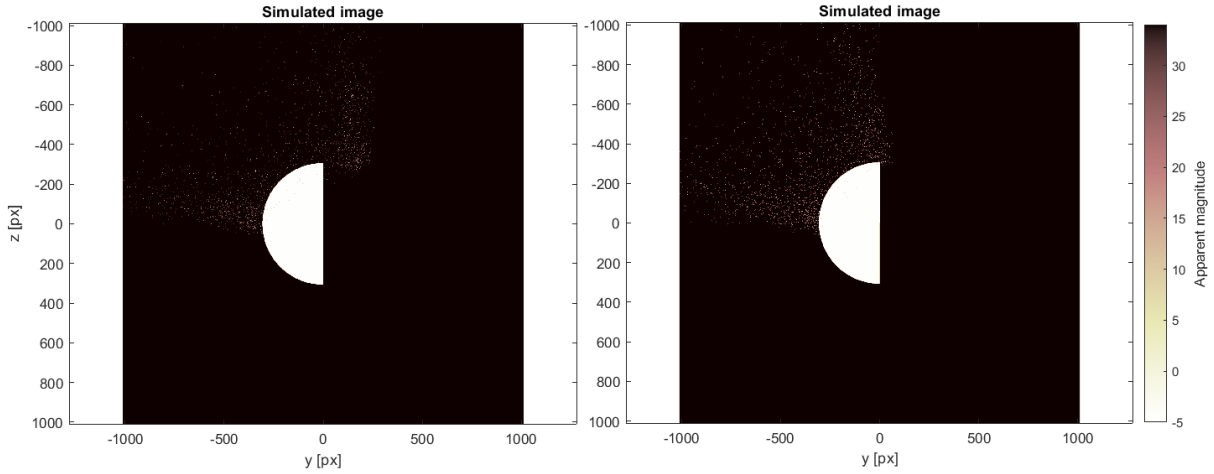

Figure 7.9: 45° latitude - 180° longitude impact, 30 minutes after the impact. [0,-2,0] km observer location. Left figure: particle size of 0.1 mm. Right figure: particle size of 1 mm.

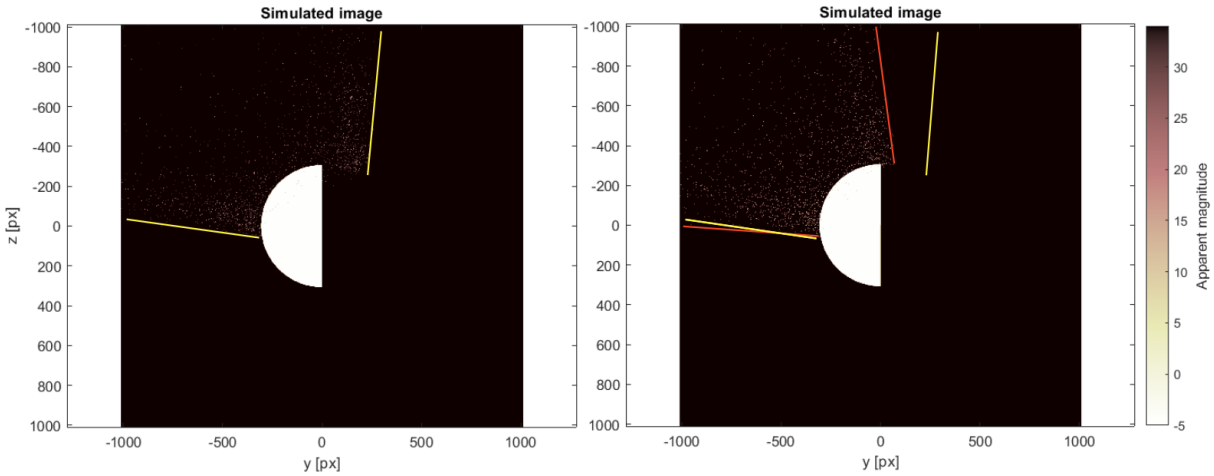

Figure 7.10: 45° latitude - 180° longitude impact, 30 minutes after the impact. [0,-2,0] km observer location. Left figure: particle size of 0.1 mm with cone edge line. Right figure: particle size of 1 mm with cone edge line of 0.1 mm and 1 mm size cone.

In the left figure, the 2 edges of the 0.1 mm particle size ejecta cone are marked in yellow. The deformation of the cone does not actually keep the edges flat, since at different heights from the surface there are particles with higher ejecta velocity but with same SRP effect. In the right image the same support lines (in red), are applied to the 1 mm particle size ejecta cone, with those of the left image for a more effective comparison. It is evident how the two structures at the same instant of time are different.

Calculating the cone deformation from the simulated images is complicated given the proximity to the event. The perspective can hide the edge of the cone taken in reference

and distort the data. As shown in Figure 7.11, the red dotted line corresponds to the visual line of the edge of the cone by the observer, which is visible in the first two instants, not in the last one, due to the cone expansion.

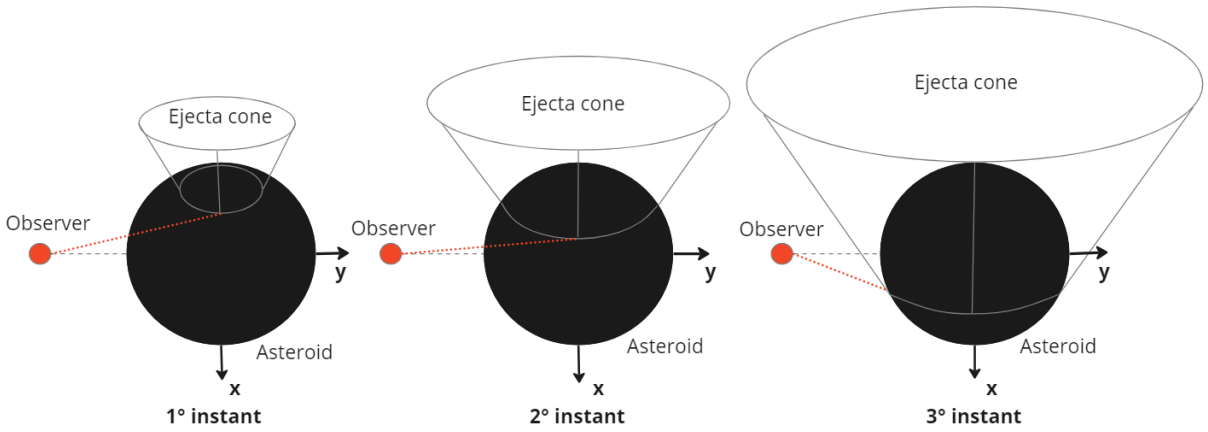

Figure 7.11: Prospective effect on ejecta cone observation. The black dashed line is the camera pointing direction, the red dashed line is the conjunction observer-ejecta cone edge at x equal to 0 (in the last the ejecta cone edge is not visible from observer).

In the case study hypothesized up to now, with the impact occurring at 45° latitude and 180° longitude, it is possible to observe the 0.1 mm dust size furthest from the axis of the cone 200 pixels away in the y-direction (reference system of the detector, Figure 5.2b), more distant than 1 mm particle size. The same observations were carried out for 5 and 10 mm particle sizes, which do not present particular divergences, demonstrating the fact that larger particles are not affected too much by solar radiation pressure.

It is useful to try to calculate the distance traveled by the two types of ejecta particles in x-direction from the image itself as an image post-process. By calculating the resolution in Eq (5.13), it is possible to estimate the deformation of the cone, which is affected by the perspective error: with the observer location equal to [0,-2,0] km, with the camera pointing towards the asteroid, in reference to the xz plane of synodic reference frame, the resolution per pixel is equal to 1.3 meters. Consequently, the difference in distance between 0.1 and 1 mm particle sizes can reach over 260 meters after 30 minutes in the antisolar direction. In Figure 7.12 the different particle sizes with respect the number of pixels in the y-direction of the detector axis are shown. The vertical right axis represents the estimated distance traveled in the x-direction (synodic reference frame).

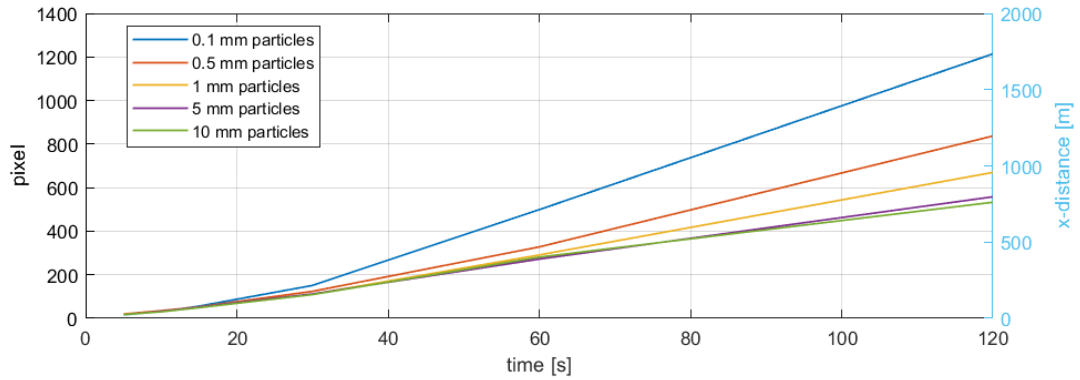

Figure 7.12: Distance in the x-direction (synodic reference frame) of different particles at different time instants after impact.

These data can be obtained for each impact location, always remembering that the perspective error alters the data with close observation images. With a real impact observation, it is possible to compare the real images with the simulated ones and modify the parameters seen in Chapter 4 to set the initial conditions and create an ejecta plume as close as possible to the real one (as done in Richardoson et al. [25] for the impact of the Deep Impact mission). In this way, the characterization of the asteroid takes place by modifying the parameters of the asteroid until the simulated image of the dust equal to the real one is obtained.

7.3. Variation of Magnitude at different phase angle

The spacecraft location changes the amount of light reflected by the dust that the onboard camera detects in relation to the phase angle: the higher the phase angle, the higher the average magnitude of the simulated image. Four types of impacts were evaluated, at different latitudes and longitudes, to compute the apparent magnitude of the dust. However, it must be remembered that the data obtained must be discarded if the Sun is in the FoV of the camera.

The post-processing technique used for this study is hiding the light coming from the asteroid to focus only on the particle reflected irradiation, as shown in Figure 7.13. Obviously, the particle data superimposed on the surface is lost, but without compromising the general result. Then the average magnitude is calculated over all pixels, which will be close to a value of 34 (which corresponds to the first digital number of pixels) because most of them are not illuminated. An average over only illuminated pixels is not possible, because the smallest particle leads to a lower diffraction, due to the lower luminosity, and

therefore to a smaller number of pixels illuminated.

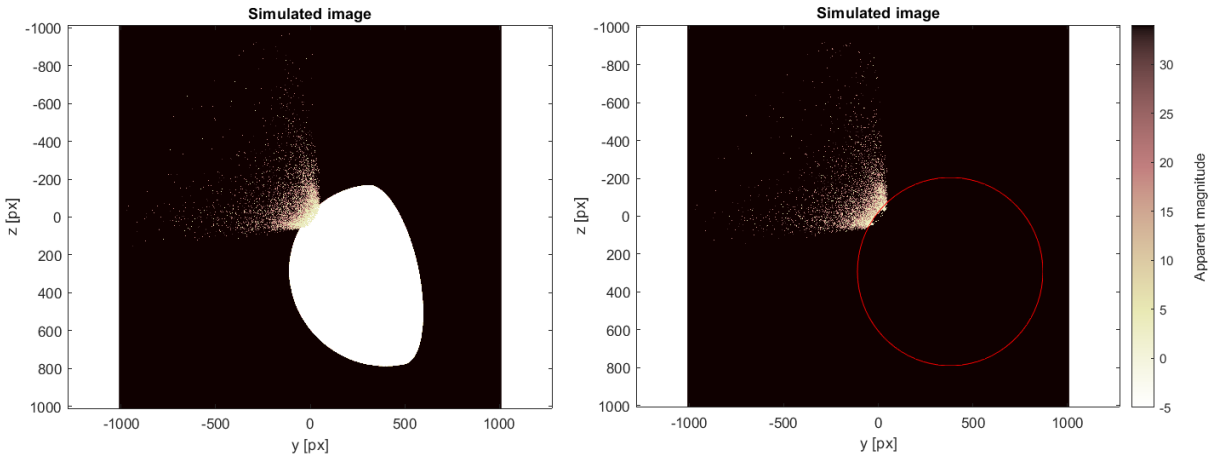

Figure 7.13: Asteroid obscuration image post-processing.

To obtain the images, the observer is positioned in 24 equally spaced positions in the circumference around the dust cone. The use of a support angle that characterizes the position of the observer with respect to the axis of the dust cone is necessary to have the same reference system for each impact. The strategy adopted is to set the angle ϕ_s equal to zero in the south position with respect to the axis of the cone, and proceed counterclockwise around the cone axis until it reaches the north position with the angle ϕ_s equal to 180°.

The four impacts studied are all in the illuminated part of the asteroid, two of them are at 45 degrees latitude, one occurs on the north pole of the asteroid and the last occurs at the equator with the axis of the dust cone parallel to Sun - asteroid direction.

From Figure 7.14 to Figure 7.17, the positions of the observer and the relative calculated average magnitude are graphically reported. Both models of radiated light reflection are applied to study their differences as well. As could be expected, the magnitude is greater for the Lambertian-sphere model, which is valid for all phase angle values, while for the Hergenrother model, the validity is limited to the 70° - 120° phase angle range. However, it is interesting to see the trend for all the phase angle values

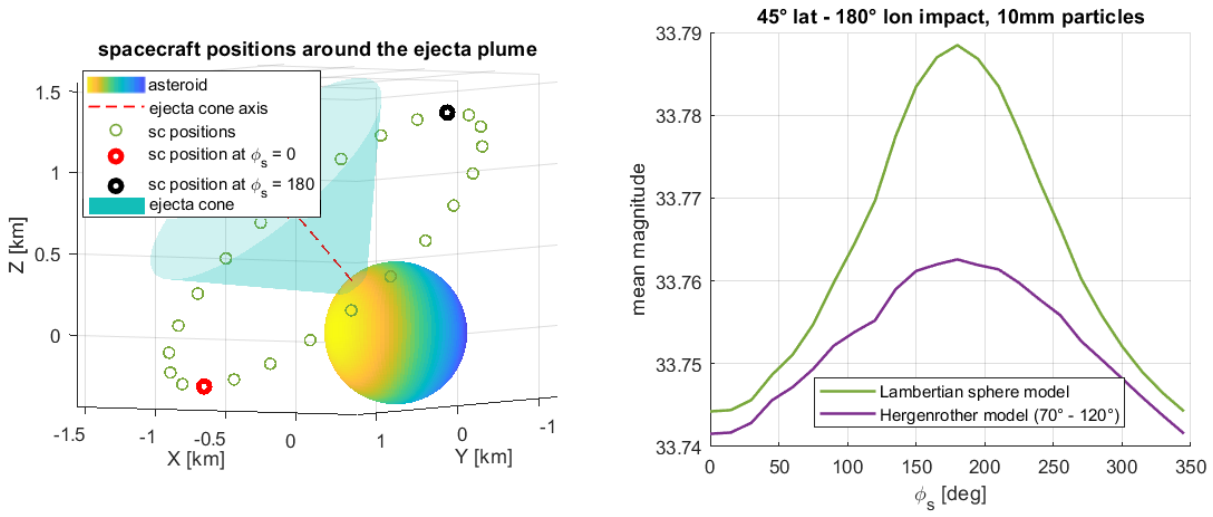

Figure 7.14: Mean magnitude computation, 45° latitude - 180° longitude impact.

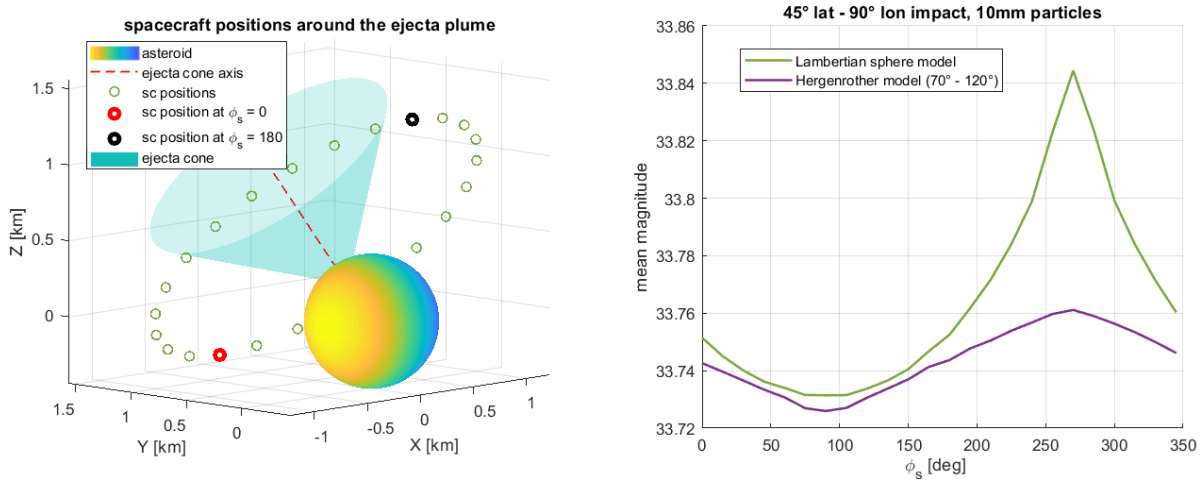

Figure 7.15: Mean magnitude computation, 45° latitude - 90° longitude impact.

All images were simulated with the camera pointing toward the impact location, 15 minutes after the impact. The average values of the detected magnitude are higher when the observer is positioned behind the cone with respect to the Sun, but it must be remembered that the images with the Sun itself in the field of view are not valid in this computation.

As it is possible to see in Figure 7.17, only in the case of the ejecta cone axis parallel to the Sun - asteroid direction, the average magnitude detected does not vary (or varies slightly due to the randomization of the departure of the particles) depending of the position around the axis.

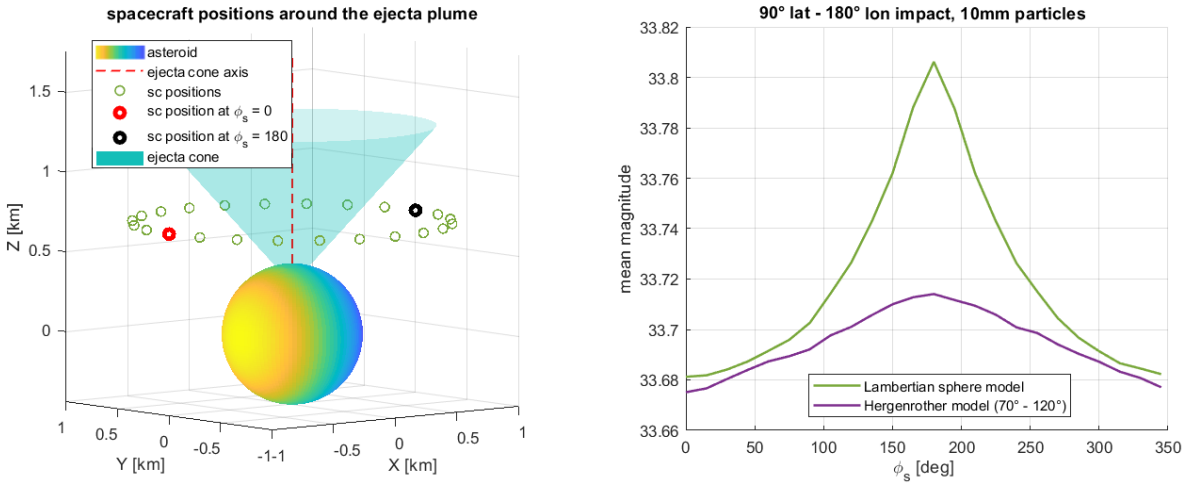

Figure 7.16: Mean magnitude computation, 90° latitude - 180° longitude impact.

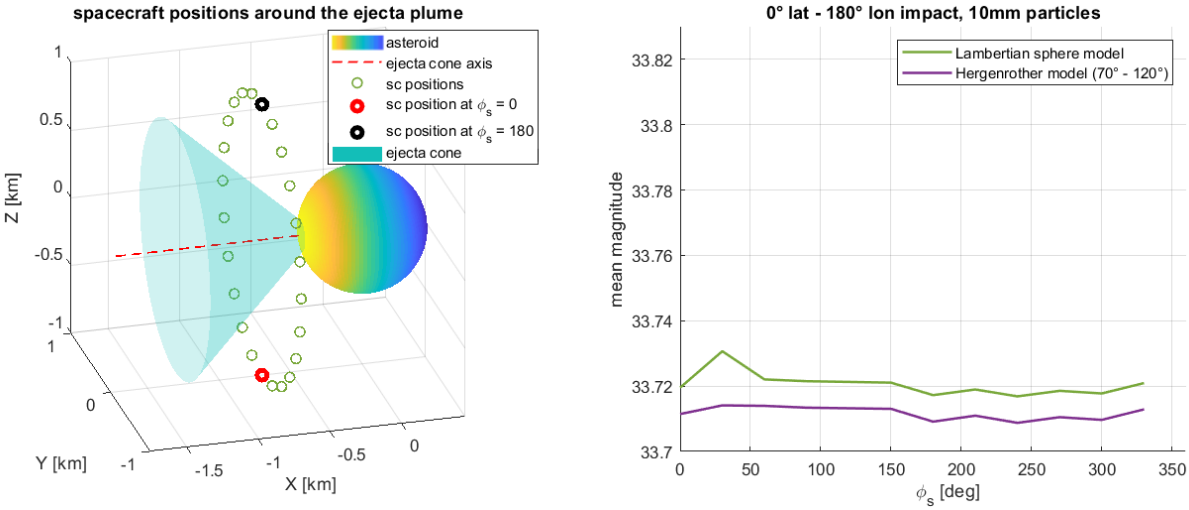

Figure 7.17: Mean magnitude computation, 0° latitude - 180° longitude impact.

A complementary study to the one just performed is to observe how the magnitude changes over time with the observer at a constant position. Figure 7.18 shows the trends of the average magnitude calculated on the images at 5, 10, 15, 20, 25, 30, 35, 40, 45, 60 and 80 minutes after the impact for three different observer locations. In the first ejecta cone growth phase, the magnitude decreases, although dust dispersion increases the magnitude per pixel. This first trend is valid for every studied observer position, but the closer the observer is to the event, the sooner the maximum perceived brightness is reached. Particularly from 1.41 kilometers away from the center of the asteroid, the minimum average magnitude is reached after 25 minutes from the impact, 30 minutes from 2 kilometers, and 45 minutes from 4 kilometers. Furthermore, it is possible to observe

how the brightness peak is higher at greater distances.

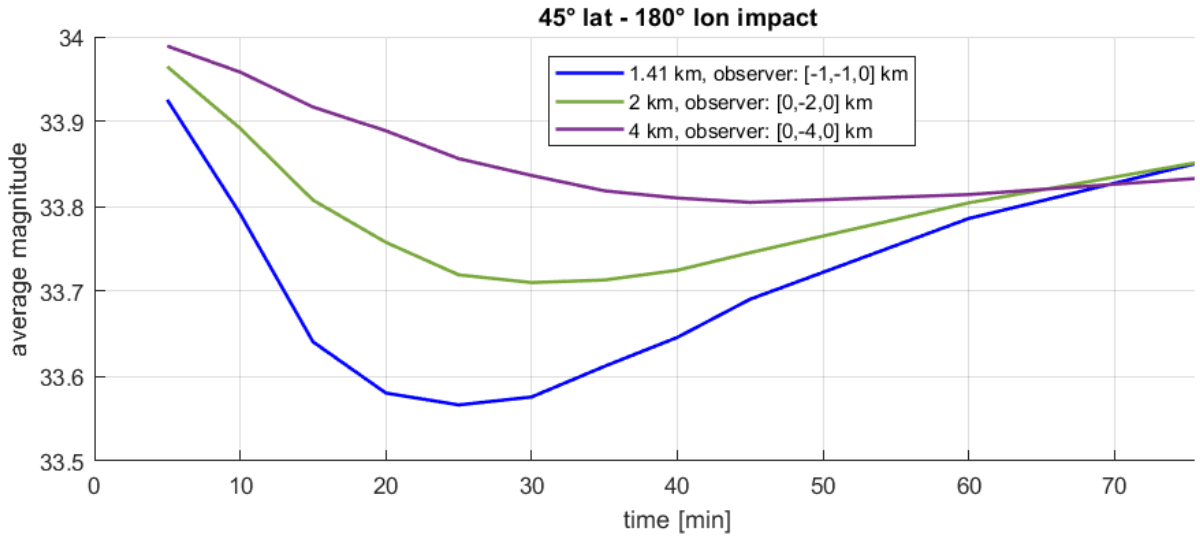

Figure 7.18: Average magnitude over time of the same impact from three different observer location: [-1,-1,0] km in blue, [0,-2,0] km in green, [0,-4,0] km in violet.

It is important to remember that the value of the average magnitude is calculated by obscuring the asteroid, and calculating the same pixels at the minimum recorded value. Consequently, the reported value is indicative only for the comparison between the cases, and not as a reference value of brightness acquired from the image.

7.4. Simulated images from a lander on surface

Subsequent images are obtained with the same imaging model but directly from the asteroid, without considering the surface in the field of view of the camera. Lander placement is discussed in Chapter 6, where both visibility and safety are covered. The images obtained are believed to be helpful in understanding the impact and, more generally, in understanding the physical characteristics of asteroid itself.

As seen in Chapter 6,it was necessary to increase the lander distance due to the uncertainty about the impact location. Indeed, the impact can occur at the established point (Figure 7.19a), but also, in the worst case, on the edge of the area of uncertainty (Figure 7.19b). As explained in Section 6.2, a possible solution to the problem is the use of several landers, located on the 2 opposite sides of the established point of impact. To quickly indicate the landers, west of the impact there is lander A, east the lander B.

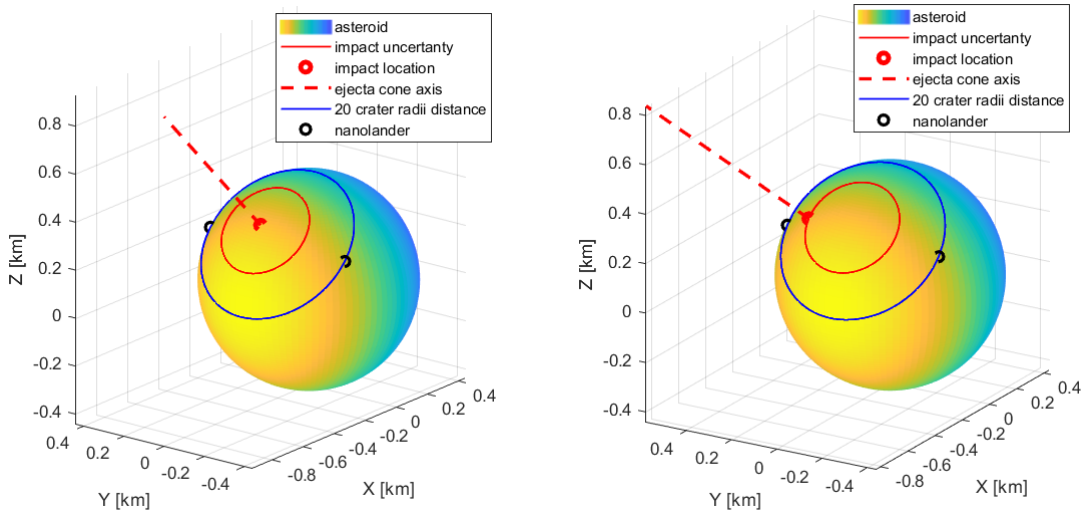

(a) Nanolader locations with impact at established point: 45° latitude - 180° longitude.

(b) Nanolader locations with uncertainty area edge impact.

Figure 7.19: Nanolander location and impact location. The lander A is west of the impact (on the left in the figure); The lander B is east of the impact (on the right in the figure)

As explained in Chapter 6, the camera is pointed towards the impact at the established location, with an inclination such that the surface is just below the FoV. Figure 7.20 shows the simulated images 5 and 10 minutes after the impact that occurred at the established location for lander A, while Figure 7.21a and Figure 7.21b shows images of lander A and B respectively for an impact occurred on the edge in the uncertainty zone (as shown in Figure 7.19b).

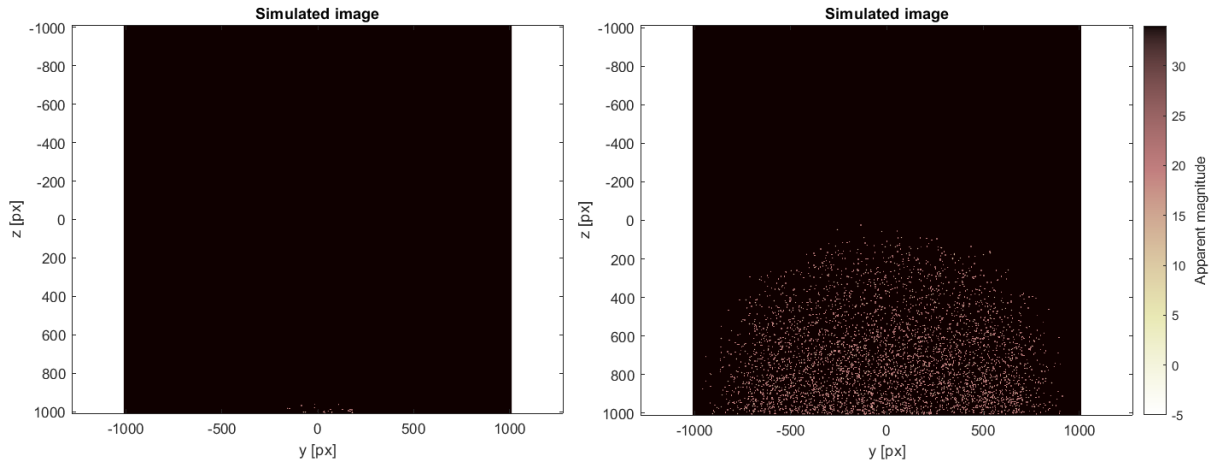

Figure 7.20: Lander A simulated images at 5 minutes (left image) and 10 minutes (right image) of impact at the established point.

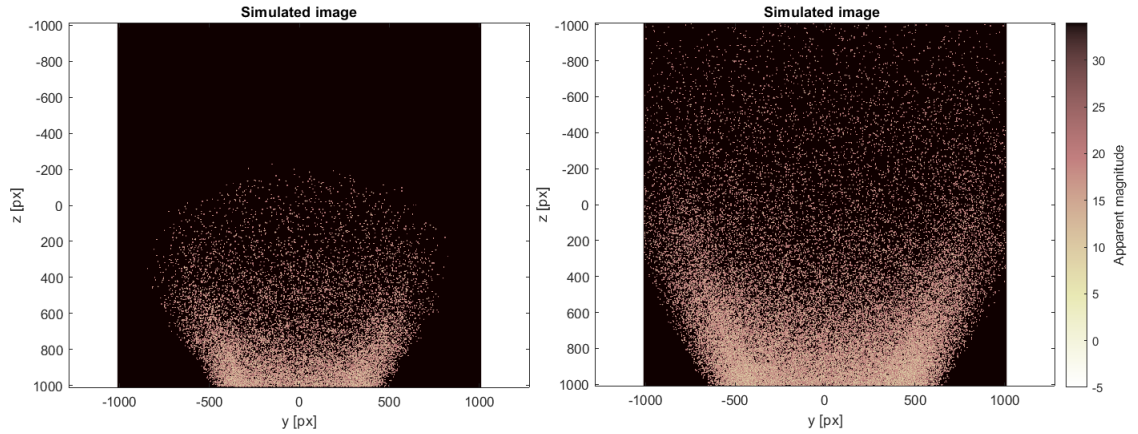

(a) Lander A simulated images at 5 minutes (left image) and 10 minutes (right image) of impact at edge of uncertainty area as in Figure 7.19b.

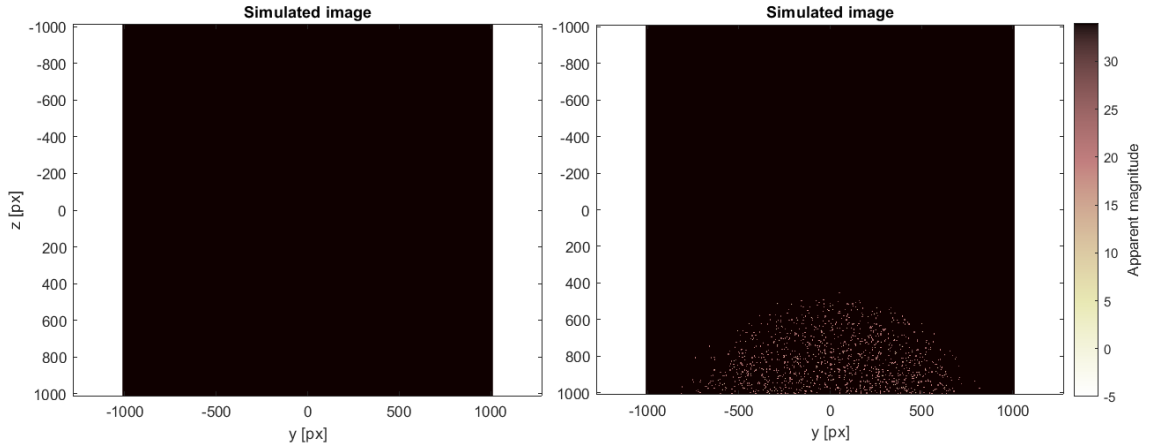

(b) Lander B simulated images at 5 minutes (left image) and 10 minutes (right image) of impact at edge of uncertainty area as in Figure 7.19b.

Figure 7.21: Edge of uncertainty area impact view form Landers at 5 and 10 minute after the event.

For the impact that took place in the established point, the ejecta cone is visible only 5 minutes after the impact, as can be seen in Figure 7.20, while if the impact is closest to lander A, as can be seen in Figure 7.21a, the ejecta cone is visible from the first minutes, while lander B does not see the cone even 5 minutes after the impact, as it is possible to observe in Figure 7.21b.

The average magnitude computation of the image obtained by the lander on the surface is calculated in the same way as it is done for the images simulated by the spacecraft. The results, visible in Figure 7.22, are obtained for both impact cases just studied.

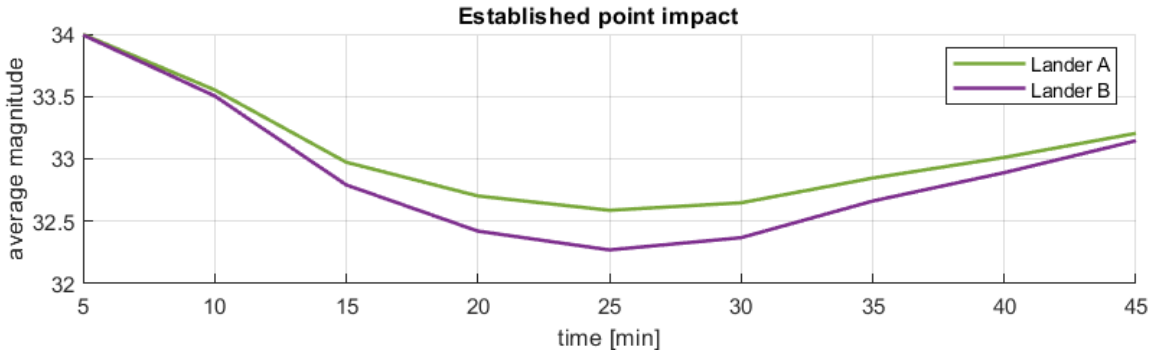

(a) Average magnitude at each instant time of established impact point.

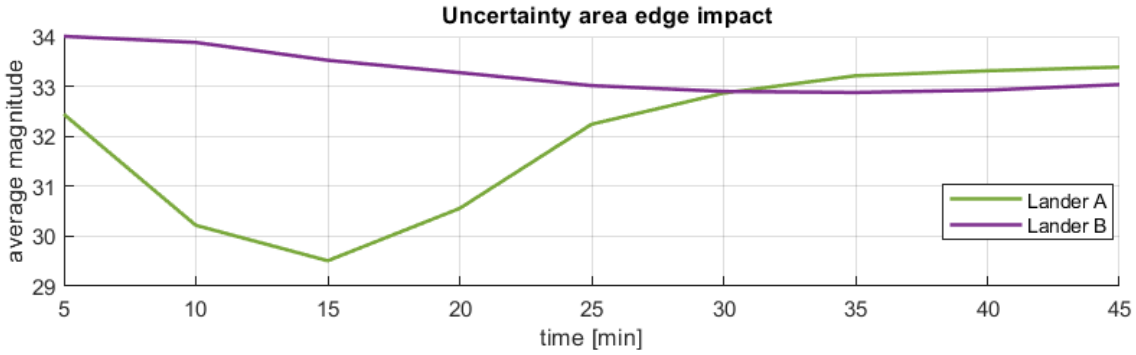

(b) Average magnitude at each instant time of impact at the edge of uncertainty area.

Figure 7.22: .The average magnitude from both landers at [5, 10, 15, 20, 25, 30, 35, 40, 45] minutes instants time.

in Figure 7.22a, it can be seen that the recorded brightness is higher for lander A, which is closest to the impact. Also, the maximum brightness is measured 15 minutes after impact, while for Lander B is about 35 minutes after impact. These results are consistent with those obtained for spacecraft images. For the impact in the established impact point, however, no perfect magnitude symmetry can be seen from the results in Figure 7.22b. This effect is due to the rotational velocity of the asteroid, which gives the dust a velocity contribution in eastward direction with respect to the impact. However, the model does not implement the rotation of the asteroid minutes after the impact, which should lead to compensation or even obtain the opposite effect. In both cases, the greatest brightness is measured about 25 minutes after impact.

With the implementation of a wide-angle camera, the edges of the ejecta cone are visible for more time, even if the perspective distortion is greater. As seen in Figure 7.23, with a 60° FoV camera, 45 minutes after impact, the time limit established for observation for lander safety, the sides of the cone are clearly visible.

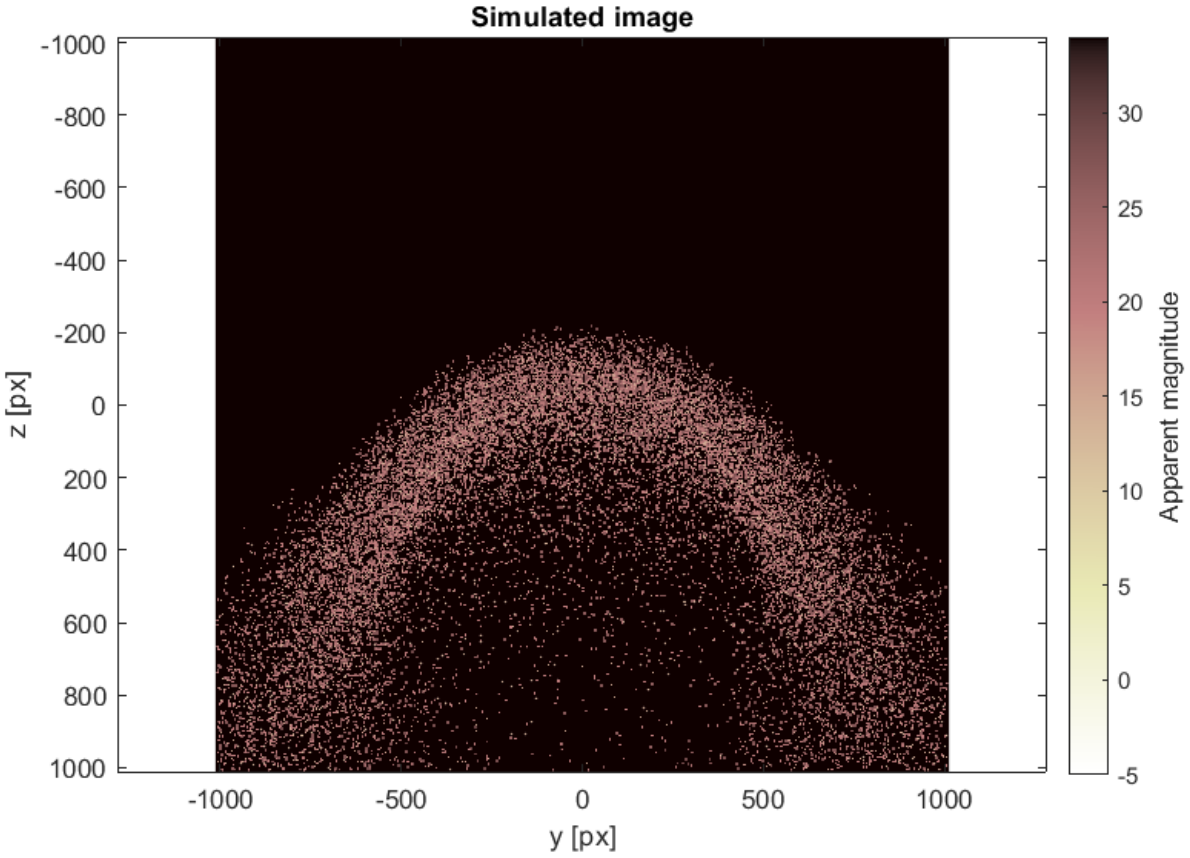

Figure 7.23: Lander A simulated image at 45 minutes of impact at the established point. 60° FoV camera.

In the end, a comparison between the lander and spacecraft images at the same instant time is shown in Figure 7.24. As it is possible to observe, and as already mentioned, in this model, the lander is unable to observe the point of impact. Indeed, the magnitude detected at the cone base by the spacecraft, despite being at a greater distance, is smaller than the first portion of the cone visible from the lander, due to the denser concentration of particles. From the images, it can be deduced that the lander can be a useful close observer for the purpose. Implementing a seismograph and other instruments necessary for a complete study of the impact event, a nanolander has the potential to be a good choice in order to obtain the information necessary for the purpose of the mission, without exaggerated development costs, given the evidence of use in the Hayabusa2 mission.

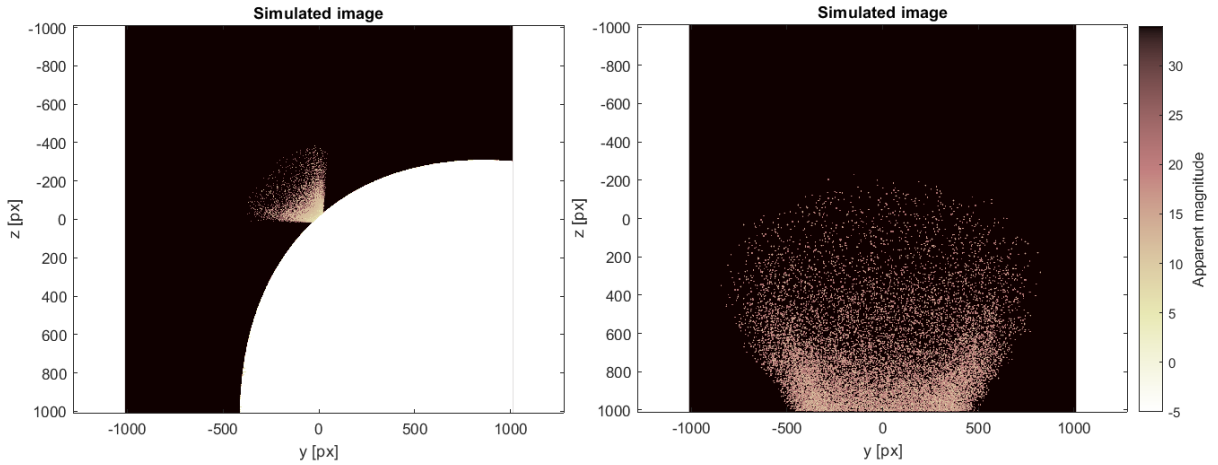

Figure 7.24: Comparison between spacecraft impact simulated image at camera position [-0.5, -0.5, 0] km (at left), and lander impact simulated image (lander A at 20 crater radii distance from impact). Impact at 45° latitude and 180° longitude, 5 minutes after impact.

8 | Conclusions and future developments

The aim of this thesis is the model development for small impact visualization on an asteroid, observed from a camera close to the asteroid itself. The study of the image obtained is also preliminary carried forward, especially as regards the total brightness of the image with respect to the position of the observer. Furthermore, the images obtained from a lander positioned close to the impact try to demonstrate their utility for the study of the event, as well as for the study of the internal structure of the asteroid.

To obtain the images, the following steps were performed: development of the dynamic model using the equations of motion of perturbed photo-gravitational Circular Restricted Three-Body Problem and setting of the initial conditions using crater formation proven models; development of the optical and image acquisition model with the camera parameters selected from instruments already tested in space and with a field of view suitable for observing the phenomenon; study of a lander use on the surface during the impact; image viewing and image processing to obtain useful data.

The use of the gravitational field coefficient J_4 in the motion equations is certainly of great importance, as explained in Kikuchi et al. [16], with respect to the development of a more realistic model. Furthermore, the image acquisition model proved to be computationally well constructed and effective in target observation. The studies on the images themselves, even if preliminary, give an idea of the phenomenon observability, also as regards the use of one or more landers, which, as seen in the images in Section 7.4, can obtain more detailed images of the ejecta cone.

Moreover, a photometry model has been specifically developed for this thesis, which consists of 2 models already widely used, using the first (developed especially for the observation of impact dust) in its range of validity, while the more simplified one for the remainder of the phase angle values.

8.1. Limitations and future work

The use and improvement of this image simulator can help to study activated asteroids, for understanding the physical characteristics. The dynamic model used in this thesis is certainly simplified, using only the zonal coefficients J_2 and J_4, without using other tesselar and sectorial coefficients. The choice is both dictated by the relevance of the coefficients used, and because the model does not require levels of complexity higher than those implemented, considering that the first instants after the impact are little influenced by the very low gravitational field of the asteroid. A more accurate model could give further realism, also as regards the visualization of the asteroid, which in this research is approximated to a sphere for computational reasons. The image acquisition model is based on the Pinhole model, an approximation of the optical system derived from the success of the cameras selected in the space environment. A more complete model should include background and system noises, which have been deliberately neglected due to their low relevance in the selected instruments, and a real optical system for modeling aberrations and diffraction.

Acknowledgements

I would like to acknowledge and thanks my thesis supervisor, Dr. Camilla Colombo, of the Aerospace Science and Technology Department at Politecnico di Milano. I would like also to thank Dr. Mirko Trisolini for their patient support and help during all the thesis. I would like to thank you for the opportunity to participate in the CRADLE project, which has received funding from the European Union's Horizon 2020 research and innovation programme under the Marie Sklodowska-Curie grant agreement No 896404 - CRADLE, and the COMPASS project, which has received funding from the European Research Council (ERC) under the European Union's Horizon 2020 research and innovation programme (grant agreement No 679086 - COMPASS).

Bibliography

[1] M. Arakawa, T. Saiki, K. Wada, K. Ogawa, T. Kadono, K. Shirai, H. Sawada, K. Ishibashi, R. Honda, N. Sakatani, et al. An artificial impact on the asteroid (162173) ryugu formed a crater in the gravity-dominated regime. *Science*, 368(6486): 67–71, 2020. doi: 10.1126/science.aaz1701.

[2] A. F. Cheng, S. Raducan, E. G. Fahnestock, E. Dotto, V. Della Corte, and A. M. Stickle. Model of double asteroid redirection test impact ejecta plume observations. *The Planetary Science Journal*, 3(6):131, 2022. doi: 10.3847/PSJ/ac66e9.

[3] M. J. Cintala, L. Berthoud, and F. Hörz. Ejection-velocity distributions from impacts into coarse-grained sand. *Meteoritics & Planetary Science*, 34(4):605–623, 1999. doi: https://doi.org/10.1111/j.1945-5100.1999.tb01367.x.

[4] E. Dotto, V. Della Corte, M. Amoroso, I. Bertini, J. Brucato, A. Capannolo, B. Cotugno, G. Cremonese, V. Di Tana, I. Gai, et al. Liciacube-the light italian cubesat for imaging of asteroids in support of the nasa dart mission towards asteroid (65803) didymos. *Planetary and Space Science*, 199:105185, 2021. doi: https://doi.org/10.1016/j.pss.2021.105185.

[5] E. G. Fahnestock, A. F. Cheng, S. Ivanovski, P. Michel, S. D. Raducan, A. Rossi, P. A. Abell, S. Chesley, E. Dotto, F. Ferrari, et al. Pre-encounter predictions of dart impact ejecta behavior and observability. *The Planetary Science Journal*, 3(9):206, 2022. doi: 10.3847/PSJ/ac7fa1.

[6] R. Garmier, A. Torres, T. Martin, L. Lorda, E. Canalias, A. Moussi, J. Biele, F. Scholten, R. Jaumann, T.-M. Ho, et al. Attitude reconstruction of mascot lander during its descent and stay on asteroid (162173) ryugu. *Planetary and Space Science*, 195:105150, 2021. doi: https://doi.org/10.1016/j.pss.2020.105150.

[7] C. Hergenrother, C. Maleszewski, J.-Y. Li, M. Pajola, S. Chesley, A. French, A. Davis, J. Pelgrift, J. Leonard, F. Shelly, et al. Photometry of particles ejected from active asteroid (101955) bennu. *Journal of Geophysical Research: Planets*, 125(9): e2020JE006381, 2020. doi: https://doi.org/10.1029/2019JE006363.

[8] K. A. Holsapple and K. R. Housen. Momentum transfer in asteroid impacts. i. theory and scaling. *Icarus*, 221(2):875–887, 2012. doi: https://doi.org/10.1016/j.icarus.2012.09.022.

[9] K. Housen, R. Schmidt, and K. Holsapple. Crater ejecta scaling laws: Fundamental forms based on dimensional analysis. *Journal of Geophysical Research: Solid Earth*, 88(B3):2485–2499, 1983. doi: https://doi.org/10.1029/JB088iB03p02485.

[10] K. R. Housen and K. A. Holsapple. Ejecta from impact craters. *Icarus*, 211(1):856–875, 2011. doi: https://doi.org/10.1016/j.icarus.2010.09.017.

[11] HubbleSite. Webb, hubble capture detailed views of dart impact, 2022 (Last retrieved 08/03/2023). URL `https://hubblesite.org/contents/news-releases/2022/news-2022-047`.

[12] T. M. Inc. Mathworks, 2022 (Last retrieved 09/04/2023). URL `https://it.mathworks.com/?s_tid=gn_logo`.

[13] K. Ishibashi, K. Shirai, K. Ogawa, K. Wada, R. Honda, M. Arakawa, N. Sakatani, and Y. Ikeda. Performance of hayabusa2 dcam3-d camera for short-range imaging of sci and ejecta curtain generated from the artificial impact crater formed on asteroid 162137 ryugu (1999 ju 3 ju_3). *Space Science Reviews*, 208:213–238, 2017. doi: https://doi.org/10.1007/s11214-016-0298-4.

[14] R. Jaumann, N. Schmitz, A. Koncz, H. Michaelis, S. Schroeder, S. Mottola, F. Trauthan, H. Hoffmann, T. Roatsch, D. Jobs, et al. The camera of the mascot asteroid lander on board hayabusa 2. *Space Science Reviews*, 208:375–400, 2017. doi: https://doi.org/10.1007/s11214-016-0263-2.

[15] S. Kameda, H. Suzuki, T. Takamatsu, Y. Cho, T. Yasuda, M. Yamada, H. Sawada, R. Honda, T. Morota, C. Honda, et al. Preflight calibration test results for optical navigation camera telescope (onc-t) onboard the hayabusa2 spacecraft. *Space Science Reviews*, 208:17–31, 2017. doi: https://doi.org/10.1007/s11214-015-0227-y.

[16] S. Kikuchi, Y. Oki, and Y. Tsuda. Frozen orbits under radiation pressure and zonal gravity perturbations. *Journal of Guidance, Control, and Dynamics*, 44(11):1924–1946, 2021. doi: https://doi.org/10.2514/1.G005564.

[17] A. V. Krivov, M. Sremčević, F. Spahn, V. V. Dikarev, and K. V. Kholshevnikov. Impact-generated dust clouds around planetary satellites: spherically symmetric case. *Planetary and Space Science*, 51(3):251–269, 2003. doi: https://doi.org/10.1016/S0032-0633(02)00147-2.

[18] J. P. Laboratory. Jpl small-body database browser: 162173 ryugu (1999 ju3), 2018 (Last retrieved 28/01/2023). URL `https://ssd.jpl.nasa.gov/tools/sbdb_lookup.html#/?sstr=Ryugu`.

[19] C. Lange, J. Biele, S. Ulamec, C. Krause, B. Cozzoni, O. Küchemann, S. Tardivel, T.-M. Ho, C. Grimm, J. T. Grundmann, et al. Mascot2–a small body lander to investigate the interior of 65803 didymos moon in the frame of the aida/aim mission. *Acta Astronautica*, 149:25–34, 2018. doi: https://doi.org/10.1016/j.actaastro.2018.05.013.

[20] C. Lange, T.-M. Ho, C. D. Grimm, J. T. Grundmann, C. Ziach, and R. Lichtenheldt. Exploring small bodies: Nano-and microlander options derived from the mobile asteroid surface scout. *Advances in Space Research*, 62(8):2055–2083, 2018. doi: https://doi.org/10.1016/j.asr.2018.05.013.

[21] A. Latino. Ejecta orbital and bouncing dynamics around asteroid ryugu. *master thesis in Space Engineering at Politecnico di Milano, Supervisor: Camilla Colombo, Co-Supervisors: Dr. Stefania Soldini, Prof. Yuichi Tsuda*, 2019.

[22] J.-Y. Li, M. Hirabayashi, T. L. Farnham, J. M. Sunshine, M. M. Knight, G. Tancredi, F. Moreno, B. Murphy, C. Opitom, S. Chesley, et al. Ejecta from the dart-produced active asteroid dimorphos. *Nature*, pages 1–3, 2023. doi: https://doi.org/10.1038/s41586-023-05811-4.

[23] D. E. Maxwell. Simple z model for cratering, ejection, and the overturned flap. In *Impact and explosion cratering: Planetary and terrestrial implications*, pages 1003–1008, 1977.

[24] NASA. Deep impact (epoxi), 2021 (Last retrieved 30/03/2023). URL `https://solarsystem.nasa.gov/missions/deep-impact-epoxi/in-depth/`.

[25] J. E. Richardson, H. J. Melosh, C. M. Lisse, and B. Carcich. A ballistics analysis of the deep impact ejecta plume: Determining comet tempel 1's gravity, mass, and density. *Icarus*, 191(2):176–209, 2007. doi: https://doi.org/10.1016/j.icarus.2007.08.033.

[26] J. E. Richardson Jr, H. J. Melosh, R. J. Greenberg, and D. P. O'Brien. The global effects of impact-induced seismic activity on fractured asteroid surface morphology. *Icarus*, 179(2):325–349, 2005. doi: https://doi.org/10.1016/j.icarus.2005.07.005.

[27] K. Richter and H. Keller. On the stability of dust particle orbits around cometary nuclei. *Icarus*, 114(2):355–371, 1995. doi: https://doi.org/10.1006/icar.1995.1068.

[28] A. S. Rivkin and A. F. Cheng. Planetary defense with the double asteroid redirection test (dart) mission and prospects. *nature communications*, 14(1):1003, 2023. doi: https://doi.org/10.1038/s41467-022-35561-2.

[29] T. Saiki, H. Imamura, M. Arakawa, K. Wada, Y. Takagi, M. Hayakawa, K. Shirai, H. Yano, and C. Okamoto. The small carry-on impactor (sci) and the hayabusa2 impact experiment. *Space Science Reviews*, 208:165–186, 2017. doi: https://doi.org/10.1007/s11214-016-0297-5.

[30] D. Scheeres and F. Marzari. Temporary orbital capture of ejecta from comets and asteroids: Application to the deep impact experiment. *Astronomy and Astrophysics*, 356:747–756, 2000.

[31] D. Scheeres, D. Durda, and P. Geissler. The fate of asteroid ejecta. *Asteroids III*, 1: 527–544, 2002.

[32] S. Soldini. *Design and control of solar radiation pressure assisted missions in the sun-earth restricted three-body problem.* PhD thesis, University of Southampton, 2016.

[33] S. Sugita, R. Honda, T. Morota, S. Kameda, H. Sawada, E. Tatsumi, M. Yamada, C. Honda, Y. Yokota, T. Kouyama, et al. The geomorphology, color, and thermal properties of ryugu: Implications for parent-body processes. *Science*, 364(6437): eaaw0422, 2019. doi: 10.1126/science.aaw0422.

[34] V. Szebehely. *Theory of Orbits, The Restricted Problem of Three Bodies, Acad.* 1967.

[35] M. Trisolini, C. Colombo, Y. Tsuda, et al. Ejecta dynamics around asteroids in view of in-orbit particle collection missions. In *INTERNATIONAL ASTRONAUTICAL CONGRESS: IAC PROCEEDINGS*, pages 1–10, 2021.

[36] M. Trisolini, C. Colombo, and Y. Tsuda. Ejecta models for particles generated by small kinetic impactors onto asteroid surfaces. In *AIAA Scitech 2022 Forum*, page 2383, 2022. doi: https://doi.org/10.2514/6.2022-2383.

[37] M. Trisolini, C. Colombo, Y. Tsuda, et al. Sensitivity analysis of asteroid ejecta models for future in-orbit sample collection mission. In *INTERNATIONAL ASTRONAUTICAL CONGRESS: IAC PROCEEDINGS*, pages 1–13, 2022.

[38] M. Trisolini, C. Colombo, and Y. Tsuda. Ejecta cloud distributions for the statistical analysis of impact cratering events onto asteroids' surfaces: A sensitivity analysis. *Icarus*, page 115432, 2023. doi: https://doi.org/10.1016/j.icarus.2023.115432.

[39] E. M. Vallerie. Investigation of photometric data received from an artificial earth

satellite. Technical report, AIR FORCE INST OF TECH WRIGHT-PATTERSON AFB OH, 1963.

[40] D. Villegas-Pinto, S. Soldini, Y. Tsuda, and J. Heiligers. Temporary capture of asteroid ejecta into periodic orbits: Application to jaxa's hayabusa2 impact event. In *AIAA Scitech 2020 Forum*, page 0221, 2020. doi: https://doi.org/10.2514/6.2020-0221.

[41] S. Watanabe, M. Hirabayashi, N. Hirata, N. Hirata, R. Noguchi, Y. Shimaki, H. Ikeda, E. Tatsumi, M. Yoshikawa, S. Kikuchi, et al. Hayabusa2 arrives at the carbonaceous asteroid 162173 ryugu—a spinning top–shaped rubble pile. *Science*, 364(6437):268–272, 2019. doi: 10.1126/science.aav8032.

[42] S.-i. Watanabe, Y. Tsuda, M. Yoshikawa, S. Tanaka, T. Saiki, and S. Nakazawa. Hayabusa2 mission overview. *Space Science Reviews*, 208:3–16, 2017. doi: https://doi.org/10.1007/s11214-017-0377-1.

[43] Y. Yu, P. Michel, S. Schwartz, S. Naidu, and L. Benner. Ejecta cloud from a kinetic impact on the secondary of a binary asteroid: I. *Mechanical Environment and Dynamic Model.*, 2016. doi: https://doi.org/10.1016/j.icarus.2016.09.008.